NOVEL METHODS FOR SOURCE LOCALIZATION AND MATERIAL IDENTIFICATION

A Dissertation

Presented to the Faculty of the Graduate School

of Cornell University

in Partial Fulfillment of the Requirements for the Degree of

Doctor of Philosophy

by

Anthony Joseph Sabelli

January 2013

NOVEL METHODS FOR SOURCE LOCALIZATION AND MATERIAL IDENTIFICATION

Anthony Joseph Sabelli

Cornell University 2013

In this work we present two independent inverse problem methods. In the first chapter we address the problem of source localization. Localizing sources in physical systems represents a class of inverse problems with broad scientific and engineering applications. This chapter is concerned with the development of a non-iterative source sensitivity approach for the localization of sources in linear systems under steady-state. We show that our proposed approach can be applied to a broad class of physical problems, ranging from source localization in elastodynamics and acoustics to source detection in heat/mass transport problems. The source sensitivity field introduced in this work represents the change of a cost functional caused by the appearance of an infinitesimal source is a given domain (or its boundary). In order to extract macroscopic inferences, we apply a threshold to the source sensitivity field in a way that parallels the application of the topological derivative concept in shape identification. We establish precise formulas for the source sensitivity field using a direct approach and a Lagrangian formulation. We show that computing the source sensitivity field entails just obtaining the solution of a single adjoint problem. Hence, the computational expense of obtaining the source sensitivity is of the same order as that of solving one forward problem. We illustrate the performance of the method through numerical examples drawn from the areas of elastodynamics, acoustics, and heat and mass transport. Our results show that our proposed approach could be used on its own as a source detection tool or to

obtain initial guesses for more quantitative iterative gradient-based minimization strategies.

In the second chapter we focus on material characterization. Material identification is integral to medical imaging, finite element calibration, non destructive testing, and other engineering applications. We propose an iterative computational framework for nonlinear material identification with transient data. Our method centers on the weak enforcement of the internal force computation, through which we derive a modified internal force equation. We subsequently enforce potentially sparse measurements in a least squares penalty term. The modified internal force equation results in a fully space-time coupled forward and adjoint problem. We consider two steps at each iteration. First the solution to the coupled problem, and second the material parameter update. Our approach generalizes the technique used for linear elastic materials. For our numerical examples, we focus on the Iwan constitutive model, commonly used to model frictional interactions in mechanical joints. We show several numerical examples exploring the accuracy of the coupled problem solution as well as the material reconstruction. We conclude with larger examples requiring distributed computation in order to demonstrate not only the algorithmic properties, but the computational scalability.

BIOGRAPHICAL SKETCH

Anthony Sabelli grew up in Swampscott, Massachusetts, and in 2004 graduated from St. Johns Preparatory School in Danvers, Massachusetts. Anthony concentrated in Applied Mathematics at Brown University. He graduated with honors in Applied Mathematics, earning the Rhon Truell Premium Prize in 2008. After receiving his masters degree from Cornell in 2011, Anthony moved to Durham, North Carolina to complete his degree while at Duke University. Upon graduation, Anthony intends to move to Minnesota having accepted a position with 3M.

For my parents.

ACKNOWLEDGEMENTS

I would like to thank the many people who have not only made this work possible, but who have also enriched my time as a graduate student. My advisor, Prof. Wilkins Aquino, has been instrumental in my success. His patience, insight, and support have been invaluable, and have helped me grow not only as a researcher, but as an individual. I would also like to thank my committee members, Prof. David Bindel, and Prof. Alex Vladimirsky for their valuable guidance throughout my time at Cornell. I am thankful for the many enlightening conversations with our research group members: Miguel Aguilo, Gabrial de Frias, Manuel Diaz, Swarnavo Sarkar, and Jim Warner. I would also like to thank the students of CAM, who have exposed me to topics and ideas I never otherwise would have known. This work would not have been possible without the support of Sandia National Laboratories. I would like to thank all of the 1542 organization, and especially Garth Reese and Tim Walsh for their vast technical knowledge and friendly support.

TABLE OF CONTENTS

LIST OF TABLES

LIST OF FIGURES

CHAPTER 1

INTRODUCTION

Classification of a problem as an "inverse problem" reflects a viewpoint by which we have incomplete or partial observations of an analogous "forward problem". Given this parity, designation of either inverse or forward hinges on an individual's viewpoint, but conventionally the problem denoted the forward problem is either better understood, or studied chronologically earlier, or perhaps mathematically better conditioned, or more consistent with physical observation. Conversely, the inverse problem sometimes features incomplete information or may require solving an ill posed mathematical problem. Solving inverse problems is fundamental to a multitude of technical fields. The heart of most medical imaging tasks can be viewed as an inverse problem [5] [7] [78] [66] [89]. Many geological inquiries, such as seismic imaging and reservoir estimation, have motivated inverse problem research [73] [76] [79]. Inverse problems in computational engineering, such as inverse heat conduction and material identification, are motivated by control problems and nondestructive testing [90] [88] [32] [6]. Given the breadth of application, significant theoretical research has been devoted to inverse problems, addressing existence, uniqueness, stability and computational considerations [47] [23].

Various computational techniques are used to solve inverse problems. Statistical inference methods have been applied with great success [52] [53] [67]. When possible, algebraic techniques are typically efficient, giving them practical advantages [51] [46]. A common and robust technique is to use numerical optimization theory [70] [25]. This is particularly useful when the forward problem is well modeled by a partial differential equation (PDE). Coupling these ideas gives rise to PDE constrained optimization [14].

Many physical problems of engineering interest can be modeled through PDEs.

After abstracting a physical process to a PDE, one typically needs to solve for the quantity of interest given some external stimulus. For example, one might solve for acoustic pressure using the Helmholtz equation given a known external acoustic source. Given this mathematical formalism of this type of forward problem, most inverse problems are posed where we have some knowledge of the former quantity of interest (acoustic pressure for the Helmholtz example), and need to infer something about the governing PDE. We may not know the geometric domain, as is the case in inverse scattering, and need to infer a shape. We may not know the external stimulus, and need to infer its location or intensity or functional form. We may not know the parameters of the PDE, which corresponds to inferring the ambient material in the Helmholtz example.

Two of the aforementioned classes of inverse problems will be addressed in this thesis. In Chapter 2, we will address source or force localization in physical contexts governed by steady state linear PDE's, given sparse measurement data. In Chapter 3, we will address material identification, *i.e.* identifying material parameters given displacement data for large structural models. We assume the reader is familiar with finite elements and computational mechanics. While we will strive to outline a complete formulation and thorough algorithm derivation, some details are omitted for the sake of clarity.

CHAPTER 2

A SUPPORT SENSITIVITY APPROACH FOR FAST SOURCE LOCALIZATION IN STEADY STATE LINEAR SYSTEMS

Methods for source localization are of high relevance in a variety of engineering and scientific applications. The source localization challenge is often cast within the mathematical framework of an inverse problem in which we are tasked with identifying a hidden driving force given the measured response of a system. Important examples of this class of problems include earthquake source localization [61, 54], damage or defect identification from acoustic emission [87, 27, 2], odor or contaminant localization [1, 41, 28, 44], and source identification in electromagnetics [12], among others. In spite of the different physics involved in the latter examples, their mathematical structures share many common features, allowing us to develop methods that are applicable to a wide range of problems.

Most popular approaches used for source localization in wave propagation problems (mechanical and electromagnetic) are centered around the concept of Time Reversal (TR) [38, 12, 17]. In TR methods, by reversing time, the measured signal is back propagated through the system and energy is focused on the region where sources are located, causing their illumination. To be applicable, the TR concept requires linearity and non-lossy or slightly lossy media. Since, the present work considers only frequency-domain dynamics and steady-state transport, it is imperative to mention that the TR concept has a frequency domain analog called the Phase Conjugation Mirror (PCM) [48]. The TR/PCM concepts have been extended to enhance robustness via the MUSIC (MUltiple SIgnal Classification) method [31]. The MUSIC method considers the response received at each of the measurement points in series, ultimately forming a response matrix for the entire

measurement array. Once the response matrix is formed, one can use a variety of robust techniques from linear algebra (*e.g.* singular value decomposition) to infer measurement locations. Holography is another technique that rests upon the same theoretical basis as TR/PCM, but makes additional assumptions about the frequency spread and/or the length scale at which measurements are made [93]. Recently, a general Bayesian framework was proposed for obtaining an optimal basis that minimize the reconstruction error in acoustic source identification problems [3]. The latter work demonstrated that this framework can be used with classical acoustic source reconstruction methods. Interestingly, the authors found that iterative optimization algorithms have not been widely used for source localization in acoustics and elastic wave propagation. This finding contrasts with the widespread use of large scale optimization theory and algorithms in other inverse problems, including source identification in contaminant transport as discussed next.

Iterative optimization methods have been widely used for source localization problems in mass/heat transport problems. It is important to recognize that the TR/PCM concepts do not apply to these problems due to their mathematical structure. Source identification in mass/heat transport problems are oftentimes solved with general methods for Partial Differential Equation (PDE) constrained optimization [1]. Gradient-based PDE-constrained optimization methods are very general and robust and can efficiently handle problems with a large number of unknowns. Biologically inspired algorithms, such as the Particle Swarm Method [43, 49], have also been successfully used for source localization in mass transport problems. These algorithms are very simple to implement, are nonintrusive to existing codes, and can find global minima. However, their main drawback is the large computational cost when the objective function is expensive to evaluate

and also they suffer from the curse of dimensionality. An interesting intuitive approach that uses qualitative reasoning and search rules to seek odor locations was presented in [58]. Bayesian methods have also been used for source localization and quantification of uncertainty [74]. All optimization-based methods are iterative in nature and, hence, call for the solution of complex and often expensive simulations multiple times.

In this work, we propose a non-iterative technique for fast source localization. Our aim is to develop a general, easy-to-implement, simple, and robust approach that can be used in a wide variety of physical problems. While the proposed method can be used on its own, it could also be used to seed a more conventional iterative method. Our proposed method is based on the notion of the existence of a Source Sensitivity (SS) or Source Derivative (SD) field that represents perturbations to a cost functional caused by the appearance of hypothetical infinitesimal sources. We show in this work how to compute such a field, and that it can be used in source localization problems. Once equipped with a source sensitivity field, we scrutinize regions where this sensitivity field attains extrema, as these are taken as indicators of the "true" locations of sources. Furthermore, we develop a general mathematical formulation that can be applied to any linear system, irrespective of the physics involved. However, for the sake of simplicity and clarity, we will limit the scope of our work to steady-state conditions, but extensions of our proposed approach to the time domain are possible. We would like to emphasize that our main goal is to find the location of sources without much regard for their intensity. Mathematically, the inverse problem at hand can be thought of as one in which the support of a function is the main unknown. Hence, we will focus on problems in which sources are indeed localized (*i.e.* the support is significantly smaller than the domain size).

It is important to highlight that the terminology "Source Sensitivity" (SS) should not be confused with the conventional directional derivatives that appear in PDE-constrained optimization formulations. Although we will show that the SS can be derived from concepts found in PDE-constrained optimization, our intention is to associate this terminology with perturbations of the cost functional to the appearance of infinitesimal sources. Therefore, the reader, from here on, should interpret "Source Sensitivity" (SS) as such.

The rest of the paper is organized in the following way. The general mathematical formulation of the forward problem is given in Section 2.1.1. In the latter section, we present a general abstract form of the forward problem, and also show particular examples in the form of elastodynamics and mass/heat transport problems. We describe the corresponding inverse problem in Section 2.2.1. The source sensitivity idea is presented in Section 2.2.1, including two different approaches for deriving the SS field: a direct and a Lagrangian approach. Finally, we show numerical examples that demonstrate the feasibility of the method in Section 2.3. Specifically, we consider acoustic waves, elastic waves, and advection-diffusion problems. We will show how our method fares given sparse and/or noisy measurements. We also discuss how the selection of measurement points affects the solution, and how sensitivity can be influenced by the physics governing the forward problem. Concluding remarks are given in Section 2.4.

2.1 Background

2.1.1 The Forward Problem

We consider arbitrary sesquilinear operators $A(\cdot,\cdot)$, which act on weakly differentiable functions over $\Omega \subset \mathbb{R}^n$. We allow mixed boundary conditions and assume the Neumann/Dirichlet/Robin portions of the boundary are known. Without loss of generality, we assume that the Dirichlet conditions are homogeneous. We will work with general variational problems of the form, find $\boldsymbol{u} \in \mathcal{V}$, such that

$$A(\boldsymbol{u},\boldsymbol{v}) = \langle \boldsymbol{f},\boldsymbol{v}\rangle + \langle \boldsymbol{h},\boldsymbol{v}\rangle_{\partial\Omega^N},\ \forall \boldsymbol{v} \in \mathcal{V} \tag{2.1}$$

where

$$\mathcal{V} = \left\{\boldsymbol{v} : \boldsymbol{v} \in H^1(\Omega),\ \boldsymbol{v} = \boldsymbol{0} \text{ on } \partial\Omega^D\right\}. \tag{2.2}$$

We also require the forcing functions to be square integrable. Specifically,

$$\boldsymbol{f} \in \mathcal{F} = \left\{\boldsymbol{f} : \boldsymbol{f} \in L^2(\Omega)\right\}, \tag{2.3}$$

$$\boldsymbol{h} \in \mathcal{H} = \left\{\boldsymbol{h} : \boldsymbol{h} \in L^2\left(\partial\Omega^N\right)\right\}. \tag{2.4}$$

The right hand side of (2.1) is defined in terms of the standard inner products over the interior of the domain and the Neumann boundary of the domain, respectively, as

$$\langle \boldsymbol{f},\boldsymbol{v}\rangle = \int_\Omega \boldsymbol{f}\cdot\overline{\boldsymbol{v}}\ d\Omega \tag{2.5}$$

$$\langle \boldsymbol{h},\boldsymbol{v}\rangle_{\partial\Omega^N} = \int_{\partial\Omega^N} \boldsymbol{h}\cdot\overline{\boldsymbol{v}}\ d(\partial\Omega^N) \tag{2.6}$$

Note that $\overline{\boldsymbol{v}}$ denotes that complex conjugate of $\boldsymbol{v}$. The $\boldsymbol{h}$ that appears on the right hand side of (2.1) is a Neumann condition acting on the Neumann portion of the boundary $\partial\Omega^N$. We also denote the adjoint of $A(\cdot,\cdot)$ by $A^*(\cdot,\cdot)$, which is defined

as,

$$A^*(\boldsymbol{u}, \boldsymbol{v}) = A(\boldsymbol{v}, \boldsymbol{u}),\ \forall \boldsymbol{u}, \boldsymbol{v}. \tag{2.7}$$

We assume that $A(\cdot, \cdot)$ satisfies the Babuska-Brezzi (BB) conditions [72]. Therefore, the solution $\boldsymbol{u}$ is bounded and unique. We make the further assumption that the adjoint operator $A^*(\cdot, \cdot)$ also satisfies the BB conditions.

In this work, we consider two specific forward problems: steady-state elastodynamics and steady-state advection-diffusion. These two model problems will allow us to demonstrate the broad applicability of the proposed method. In this section, we show details of their formulations, which will be later used in the numerical section of this work.

Frequency Domain Elastodynamics

The steady-state harmonic response of a forced linear elastic body is described by

$$\nabla \cdot (\boldsymbol{\mathcal{C}} : \nabla \boldsymbol{u}) + \rho \omega^2 \boldsymbol{u} = \boldsymbol{f},\ \boldsymbol{x} \in \Omega \tag{2.8}$$

$$\boldsymbol{\mathcal{C}} : \nabla \boldsymbol{u} \cdot \boldsymbol{n} = \boldsymbol{h},\ \boldsymbol{x} \in \partial\Omega^N \tag{2.9}$$

$$\boldsymbol{u} = \boldsymbol{0},\ \boldsymbol{x} \in \partial\Omega^D \tag{2.10}$$

$$\boldsymbol{B}^R \boldsymbol{u} = \boldsymbol{0},\ \boldsymbol{x} \in \partial\Omega^R \tag{2.11}$$

where $\boldsymbol{n}$ is the normal direction on $\partial\Omega$; $\partial\Omega^N$ represents the Neumann portion of the boundary; the function $\boldsymbol{h}$ represents surface forces; $\partial\Omega^D$ is the Dirichlet portion of the boundary where $\boldsymbol{u}$ is specified to be equal to $\boldsymbol{0}$; and $\boldsymbol{B}^R$ is a linear operator defined on $\partial\Omega^R$, representing an absorbing condition. We can split the operator $\boldsymbol{B}^R$ into a differential portion, $\boldsymbol{B'}$, and an algebraic portion, $\boldsymbol{B}^u$. In order for this problem to be well defined, $\partial\Omega^N$, $\partial\Omega^D$, and $\partial\Omega^R$ are non-overlapping and their union is all of $\partial\Omega$. $\boldsymbol{\mathcal{C}}$ is the (fourth order) elasticity tensor describing the

underlying material. The corresponding weak formulation is to find $\boldsymbol{u} \in \mathcal{V}$ such that

$$A(\boldsymbol{u}, \boldsymbol{v}) = \langle l, \boldsymbol{v} \rangle, \ \forall \boldsymbol{v} \in \mathcal{V} \tag{2.12}$$

where

$$A(\boldsymbol{u}, \boldsymbol{v}) = \int_\Omega \nabla \boldsymbol{u} : \boldsymbol{\mathcal{C}} : \nabla \overline{\boldsymbol{v}} - \rho\omega^2 \boldsymbol{u} \cdot \overline{\boldsymbol{v}} \ d\Omega + \int_{\partial\Omega^R} \boldsymbol{B}^u \boldsymbol{u} \cdot \overline{\boldsymbol{v}} \ d(\partial\Omega) \tag{2.13}$$

$$\langle l, \boldsymbol{v} \rangle = \int_\Omega \boldsymbol{f} \cdot \overline{\boldsymbol{v}} \ d\Omega + \int_{\partial\Omega^N} \boldsymbol{h} \cdot \overline{\boldsymbol{v}} \ d(\partial\Omega). \tag{2.14}$$

The analogous weak formulation for acoustics problems can be found in [36] and is not shown here for the sake of brevity. The presence of an absorbing boundary condition will render this operator not self adjoint.

Mass/Heat Transport (Advection-Diffusion).

The boundary value problem for advection-diffusion is given as

$$D\Delta u - \boldsymbol{a} \cdot \nabla u + f = 0, \ \boldsymbol{x} \in \Omega \tag{2.15}$$

$$u = 0, \ \boldsymbol{x} \in \partial\Omega \tag{2.16}$$

where D is the diffusivity of the media and $\boldsymbol{a}$ is the velocity field. The corresponding weak formulation is to find $u \in \mathcal{V}$ such that

$$A(u, v) = \langle f, v \rangle, \ \forall v \in \mathcal{V}, \tag{2.17}$$

where

$$A(u, v) = \int_\Omega D(\nabla u \cdot \nabla v) + v(\boldsymbol{a} \cdot \nabla u) \ d\Omega \tag{2.18}$$

$$\langle f, v \rangle = \int_\Omega f v \ d\Omega. \tag{2.19}$$

Observe that the bilinear form is not self adjoint in this case. The adjoint bilinear form is given as

$$A^*(u,v) = \int_\Omega D\nabla u \cdot \nabla v - u(\boldsymbol{a} \cdot \nabla v)\ d\Omega \tag{2.20}$$

Notice that, without loss of generality, we will consider only interior sources (*i.e.* only prescribed Dirichlet boundary conditions) in advection-diffusion problems.

2.2 Formulation of the Source Sensitivity Approach

2.2.1 Inverse Problem Statement

The inverse problem contrasts with the forward problem in that we have information about the solution $\boldsymbol{u}$ over some part of the domain, and need to identify the support of some unknown sources. We assume knowledge of a measured field $\boldsymbol{u}^{\mathrm{M}}$ on some subset of the domain, which is denoted as Ω^{M}. We further assume that $\boldsymbol{u}^{\mathrm{M}}$ is a measurement of $\boldsymbol{u}^{\mathrm{True}}$, where $\boldsymbol{u}^{\mathrm{True}}$ satisfies the forward problem exactly for some $\boldsymbol{f}^{\mathrm{True}}$ and $\boldsymbol{h}^{\mathrm{True}}$. Our goal is to determine the support of $\boldsymbol{f}^{\mathrm{True}}$ and $\boldsymbol{h}^{\mathrm{True}}$, denoted $\mathrm{supp}(\boldsymbol{f}^{\mathrm{True}})$ and $\mathrm{supp}(\boldsymbol{h}^{\mathrm{True}})$ respectively, based on our measurements. In order to determine $\mathrm{supp}(\boldsymbol{f}^{\mathrm{True}})$ and $\mathrm{supp}(\boldsymbol{h}^{\mathrm{True}})$, we define a functional

$$J(\boldsymbol{f},\boldsymbol{h}) = \frac{1}{2}\int_{\Omega^M} \left|\boldsymbol{u}(\boldsymbol{f},\boldsymbol{h}) - \boldsymbol{u}^{\mathrm{M}}\right|^2\ d\Omega, \tag{2.21}$$

where $\boldsymbol{u}(\boldsymbol{f},\boldsymbol{h})$ satisfies (2.1) for some postulated $\boldsymbol{f}$ and $\boldsymbol{h}$. The first step in our proposed approach will be to characterize the perturbation of the cost functional in (2.21) when a hypothetical infinitesimal source is introduced. The next section describes the source sensitivity field and approaches to compute it. It is important to keep in mind that we will take all sources to be square-integrable functions (*e.g.* $\boldsymbol{f} \in L^2(\Omega)$, $\boldsymbol{h} \in L^2(\partial\Omega^N)$).

The Source Sensitivity Field.

In this section, we introduce the source sensitivity field. The source sensitivity field denoted as D_T quantifies how the cost functional J changes when we introduce infinitesimal sources. For the sake of clarity and simplicity, we will consider perturbations in body sources only, as surface sources can be treated in a similar way. Next, we will consider two approaches to determine an expression for the source sensitivity D_T: a direct approach and a Lagrangian approach.

The direct approach. To derive an expression for the source sensitivity $D_T(\boldsymbol{x}, \boldsymbol{K})$, consider a localized source $\boldsymbol{\delta f}$ defined as

$$\boldsymbol{\delta f} = \boldsymbol{K}\chi_{\mathcal{B}(\boldsymbol{x},\varepsilon)}, \tag{2.22}$$

where $\boldsymbol{K}$ is a vector that defines a direction, χ_A is an indicator function of the set $\mathcal{A} \subset \Omega$, and $\mathcal{B}(\boldsymbol{x}, \varepsilon)$ denotes a ball centered at $\boldsymbol{x}$ with radius ε.

Given the form of the source perturbation, (2.22), we seek a source sensitivity field, $D_T(\boldsymbol{x}, \boldsymbol{K})$, such that

$$J(\boldsymbol{f} + \boldsymbol{\delta f}) = J(\boldsymbol{f}) + \mu(\varepsilon)D_T(\boldsymbol{x}, \boldsymbol{K}) + o(\mu(\varepsilon)), \tag{2.23}$$

where $\boldsymbol{x}$ is the center of the support of $\boldsymbol{\delta f}$, ε is the characteristic length of the support of $\boldsymbol{\delta f}$, and $\mu(\varepsilon)$ is a given positive function such that

$$\lim_{\epsilon \to 0} \mu(\varepsilon) \to 0. \tag{2.24}$$

By definition $o(\mu(\varepsilon))$ means

$$\lim_{\epsilon \to 0} \frac{o(\mu(\varepsilon))}{\mu(\varepsilon)} \to 0. \tag{2.25}$$

We begin by computing the Gâteaux derivative of the cost functional J in the direction of an arbitrary localized body source $\boldsymbol{\delta f}$ as

$$\begin{aligned} DJ \cdot \boldsymbol{\delta f} &= \frac{1}{2}\frac{d}{d\eta}\left[\int_{\Omega^M} \left|\boldsymbol{u}(\boldsymbol{f}+\eta\boldsymbol{\delta f}) - \boldsymbol{u}^{\mathrm{M}}\right|^2 \, d\Omega\right]_{\eta=0} \\ &= \frac{1}{2}\frac{d}{d\eta}\left[\int_{\Omega^M} \left|\boldsymbol{u}(\boldsymbol{f}) + \eta\boldsymbol{u}(\boldsymbol{\delta f}) - \boldsymbol{u}^{\mathrm{M}}\right|^2 \, d\Omega\right]_{\eta=0} \end{aligned} \tag{2.26}$$

where we have invoked linearity of $\boldsymbol{u}$ in its first argument in expanding $\boldsymbol{u}(\boldsymbol{f}+\boldsymbol{\delta f})$. Note that $\eta \in \mathbb{R}$. Expanding the modulus in the above integral, we get

$$DJ \cdot \boldsymbol{\delta f} = \frac{d}{d\eta}\left[J(\boldsymbol{f}) + \Re\left[\int_{\Omega^M} \eta\, \boldsymbol{u}(\boldsymbol{\delta f}) \cdot \overline{(\boldsymbol{u}(\boldsymbol{f}) - \boldsymbol{u}^{\mathrm{M}})}\, d\Omega\right] + \frac{\eta^2}{2}\,||\boldsymbol{u}(\boldsymbol{\delta f})||^2_{L^2}\right]_{\eta=0}, \tag{2.27}$$

where $\Re[g]$ denotes the real part of g. Carrying out the derivative and substituting $\eta = 0$, we get

$$DJ \cdot \boldsymbol{\delta f} = \Re\left[\int_{\Omega^M} \boldsymbol{u}(\boldsymbol{\delta f}) \cdot \overline{(\boldsymbol{u}(\boldsymbol{f}) - \boldsymbol{u}^{\mathrm{M}})}\, d\Omega\right]. \tag{2.28}$$

We now introduce the Green's tensor $\boldsymbol{G}(\boldsymbol{x},\boldsymbol{y})$, corresponding to the operator $A(\cdot,\cdot)$ in (2.1), which allows us to express

$$\boldsymbol{u}(\boldsymbol{\delta f}) = \int_{\Omega} \boldsymbol{G}(\boldsymbol{x},\boldsymbol{y})\boldsymbol{\delta f}(\boldsymbol{y})\, d\Omega(\boldsymbol{y}). \tag{2.29}$$

Substituting (2.29) into (2.28), yields

$$\begin{aligned} DJ \cdot \boldsymbol{\delta f} &= \Re\left[\int_{\Omega^M}\left[\int_{\Omega} \boldsymbol{G}(\boldsymbol{x},\boldsymbol{y})\boldsymbol{\delta f}(\boldsymbol{y})\, d\Omega(\boldsymbol{y})\right] \cdot \overline{(\boldsymbol{u}(\boldsymbol{f}) - \boldsymbol{u}^{\mathrm{M}})}\, d\Omega(\boldsymbol{x})\right] \\ &= \Re\left[\int_{\Omega}\left[\int_{\Omega^M} \boldsymbol{G}^{*}(\boldsymbol{x},\boldsymbol{y})\left(\boldsymbol{u}(\boldsymbol{f}) - \boldsymbol{u}^{\mathrm{M}}\right)\, d\Omega(\boldsymbol{x})\right] \cdot \overline{\boldsymbol{\delta f}}(\boldsymbol{y})\, d\Omega(\boldsymbol{y})\right]. \end{aligned} \tag{2.30}$$

In the last equation, we have switched the order of integration and used the identity $\Re[\overline{\boldsymbol{a}} \cdot \boldsymbol{P}\boldsymbol{b}] = \Re[\overline{\boldsymbol{b}} \cdot \boldsymbol{P}^{*}\boldsymbol{a}]$. Where $\boldsymbol{a}$ and $\boldsymbol{b}$ are complex vectors, $\boldsymbol{P}$ is a linear operator and $\boldsymbol{P}^{*}$ is the adjoint of $\boldsymbol{P}$. Also, notice that we have introduced the adjoint of the Green's tensor, $\boldsymbol{G}^{*}(\boldsymbol{x},\boldsymbol{y})$, which allows us to represent the solution to the adjoint variational problem: find $\boldsymbol{T} \in \mathcal{V}$ such that

$$A^{*}(\boldsymbol{T},\boldsymbol{w}) = \int_{\Omega^M} \left(\boldsymbol{u}(\boldsymbol{f}) - \boldsymbol{u}^{\mathrm{M}}\right) \cdot \overline{\boldsymbol{w}}\, d\Omega,\ \forall \boldsymbol{w} \in \mathcal{U} \tag{2.31}$$

as the integral

$$\boldsymbol{T}(\boldsymbol{y}) = \int_{\Omega^{\mathrm{M}}} \boldsymbol{G}^{*}(\boldsymbol{x},\boldsymbol{y}) \left(\boldsymbol{u}(\boldsymbol{f}) - \boldsymbol{u}^{\mathrm{M}}\right)\ d\Omega(\boldsymbol{x}). \tag{2.32}$$

Notice that the test functions for the forward problem, and therefore $\boldsymbol{T}$, are constrained to be zero on the Dirichlet boundary. It is also interesting to observe that (2.31) is the same as the adjoint problem that arises in gradient-based PDE-constrained optimization formulations [16].

Substituting $\boldsymbol{\delta f}$ given in (2.22) into (2.30), and using (2.32), yields

$$\begin{aligned} DJ \cdot \delta\boldsymbol{f} &= \Re\left[\int_{\Omega} \overline{\boldsymbol{K}}\chi_{\mathcal{B}(\boldsymbol{x},\varepsilon)} \cdot \boldsymbol{T}(\boldsymbol{y})\ d\Omega(\boldsymbol{y})\right] \\ &= \Re\left[\int_{\mathcal{B}(\boldsymbol{x},\varepsilon)} \overline{\boldsymbol{K}} \cdot \boldsymbol{T}(\boldsymbol{y})\ d\Omega(\boldsymbol{y})\right]. \end{aligned} \tag{2.33}$$

Since $\boldsymbol{T}$ is in $\mathcal{V}$, and hence locally integrable, we can use the Lebesgue differentiation theorem (see Appendix E , Theorem 6 in Reference [35]) to express the integral in (2.33) (for small ε) as

$$DJ \cdot \delta\boldsymbol{f} = \Re\left[\overline{\boldsymbol{K}} \cdot \boldsymbol{T}(\boldsymbol{x})\right] |\mathcal{B}(\boldsymbol{x},\varepsilon)| + o(|\mathcal{B}(\boldsymbol{x},\varepsilon)|) \tag{2.34}$$

where $|\mathcal{B}(\boldsymbol{x},\varepsilon)|$ denotes the measure of the ball. Expanding $J(\boldsymbol{f}+\delta\boldsymbol{f})$ about $J(\boldsymbol{f})$, considering a small ε, and using (2.34), yields

$$\begin{aligned} J(\boldsymbol{f}+\boldsymbol{\delta f}) &= J(\boldsymbol{f}) + DJ \cdot \delta\boldsymbol{f} + o(\|\boldsymbol{\delta} f\|) \\ &= J(\boldsymbol{f}) + \Re\left[\overline{\boldsymbol{K}} \cdot \boldsymbol{T}(\boldsymbol{x})\right] |\mathcal{B}(\boldsymbol{x},\varepsilon)| + o(|\mathcal{B}(\boldsymbol{x},\varepsilon)|) \end{aligned} \tag{2.35}$$

Comparing equations (2.35) and (2.23), we can identify the expression for the source sensitivity field as

$$D_T(\boldsymbol{x},\boldsymbol{K}) = \Re\left[\overline{\boldsymbol{K}} \cdot \boldsymbol{T}(\boldsymbol{x})\right], \tag{2.36}$$

while $\mu(\varepsilon) = |\mathcal{B}(\boldsymbol{x},\varepsilon)|$.

Remark 1 *The derivation of the source sensitivity due to surface sources follows closely the developments shown in this section. The only difference in the final result would be that* $\mathcal{B}(\boldsymbol{x}, \varepsilon) \subset \partial\Omega^N$*, and* $\boldsymbol{T}(\boldsymbol{x})$ *takes values over* $\partial\Omega^N$*. Since* $\boldsymbol{T}(\boldsymbol{x})$ *is computed the same way for both surface and body sources, we can compute the source sensitivity field* $D_T(\boldsymbol{x}, \boldsymbol{K})$ *for both cases simultaneously and consider its values over* $\Omega \cup \partial\Omega^N$*.*

Remark 2 *It is important to bear in mind that our asymptotic expansion of the cost functional* J *assumes that a source has vanishing support. Therefore, we expect that our reconstruction method can be used only in cases in which true sources are localized.*

The Lagrangian viewpoint. In this section, we present an alternate derivation of the source sensitivity $D_T(\boldsymbol{x}, \boldsymbol{K})$ by means of a Lagrangian. Our approach is to use a Lagrangian to derive $DJ \cdot \delta\boldsymbol{f}$, which, as in the previous section, allows us to arrive an expression for $D_T(\boldsymbol{x}, \boldsymbol{K})$ by using asymptotic arguments. Consider the Lagrangian functional

$$\mathcal{L}(\boldsymbol{u}, \boldsymbol{\lambda}, \boldsymbol{f}) = \frac{1}{2} \int_{\Omega^M} \left| \boldsymbol{u} - \boldsymbol{u}^{\mathrm{M}} \right|^2 \, d\Omega^M + \Re \left[A(\boldsymbol{u}, \boldsymbol{\lambda}) - \langle \boldsymbol{f}, \boldsymbol{\lambda} \rangle \right]. \tag{2.37}$$

As before, $\boldsymbol{u} \in \mathcal{V}$ and $\boldsymbol{f} \in \mathcal{F}$. We can interpret the function $\boldsymbol{\lambda} \in \mathcal{V}$ as a Lagrange multiplier used to enforce the forward variational problem. Formally, $\mathcal{L} : \mathcal{V} \times \mathcal{V} \times \mathcal{F} \to \mathbb{R}$. We proceed by taking variations of $\mathcal{L}$ with respect to $\boldsymbol{u}$ and $\boldsymbol{\lambda}$, subsequently setting them equal to zero for all directions $\boldsymbol{\delta u} \in \mathcal{V}$ and $\boldsymbol{\delta\lambda} \in \mathcal{V}$, and finally obtaining an expression for $DJ \cdot \boldsymbol{f}$. First, taking the variation of $\mathcal{L}$ with respect to $\boldsymbol{\lambda}$, we get

$$D\mathcal{L} \cdot \boldsymbol{\delta\lambda} = \Re \left[A(\boldsymbol{u}, \boldsymbol{\delta\lambda}) - \langle \boldsymbol{f}, \boldsymbol{\delta\lambda} \rangle \right] \tag{2.38}$$

Setting (2.38) equal to zero for all $\boldsymbol{\delta\lambda}$, we recover the forward variational problem in (2.1). That is, find $\boldsymbol{u} \in \mathcal{V}$ such that

$$A(\boldsymbol{u}, \boldsymbol{\delta\lambda}) = \langle \boldsymbol{f}, \boldsymbol{\delta\lambda} \rangle, \ \forall \boldsymbol{\delta\lambda} \in \mathcal{V} \tag{2.39}$$

Next, we take the variation of $\mathcal{L}$ with respect to $\boldsymbol{u}$ as

$$D\mathcal{L} \cdot \boldsymbol{\delta u} = \Re \left[A(\boldsymbol{\delta u}, \boldsymbol{\lambda}) - \int_{\Omega^M} \boldsymbol{\delta u} \cdot \overline{(\boldsymbol{u} - \boldsymbol{u}^{\mathrm{M}})} \, d\Omega \right] \tag{2.40}$$

$$= \Re \left[A^*(\boldsymbol{\lambda}, \boldsymbol{\delta u}) - \int_{\Omega^M} (\boldsymbol{u} - \boldsymbol{u}^{\mathrm{M}}) \cdot \overline{\boldsymbol{\delta u}} \, d\Omega \right]. \tag{2.41}$$

Setting (2.41) equal to zero for all $\delta\boldsymbol{u} \in \mathcal{V}$, results in the variational problem: find $\boldsymbol{\lambda} \in \mathcal{V}$ such that

$$A^*(\boldsymbol{\lambda}, \boldsymbol{\delta u}) = \int_{\Omega^M} (\boldsymbol{u} - \boldsymbol{u}^{\mathrm{M}}) \cdot \overline{\boldsymbol{\delta u}} \, d\Omega, \ \forall \boldsymbol{\delta u} \in \mathcal{V}. \tag{2.42}$$

The problem in (2.42) is the same as the adjoint variational problem that we encountered in (2.31). Taking $\boldsymbol{u}$ and $\boldsymbol{\lambda}$ such that they satisfy the forward and adjoint problems in Eqs. (2.39) and (2.42), respectively, we can conclude that (for these $\boldsymbol{u}$ and $\boldsymbol{\lambda}$)

$$D\mathcal{L} \cdot \boldsymbol{\delta f} = DJ \cdot \boldsymbol{\delta f}. \tag{2.43}$$

Now, taking the variation of $\mathcal{L}$ with respect to $\boldsymbol{f}$, we arrive at

$$DJ \cdot \boldsymbol{\delta f} = D\mathcal{L} \cdot \boldsymbol{\delta f} = \Re\langle \boldsymbol{\delta f}, \boldsymbol{\lambda} \rangle \tag{2.44}$$

Notice that from (2.31) and (2.42), we can infer that $\boldsymbol{\lambda} \equiv \boldsymbol{T}$. Substituting $\boldsymbol{T}$ and (2.22) into Eq. (2.44), we arrive again at (2.33). Then, we can proceed as in the previous section. That is, we use the approximation in (2.34) with (2.33) to arrive at the expression for $D_T(\boldsymbol{x}, \boldsymbol{K})$ given in (2.36).

Source localization strategy based on the source sensitivity.

Up to this point, we have derived an expression for the source sensitivity field, $D_T(\boldsymbol{x}, \boldsymbol{K})$. In this section, we describe a procedure for estimating the location of sources by means of this source sensitivity. This approach is influenced by the Topological Derivative concept used in inverse scattering problems [21, 36, 10], materials/defect identification problems [22, 19], and topology optimization [85]. While the source sensitivity approach is theoretically independent from the topological derivative, we consider the same thresholding heuristic, as both techniques seek to infer macroscopic change from infinitesimal perturbations. That is, we postulate that since large negative values of the source sensitivity field cause commensurate reductions of the cost functional J in (2.23), the source sensitivity field will attain large negative values where "true" sources are located. Guided by this insight, we will look for regions in $\Omega \cup \partial\Omega$ where $D_T(\boldsymbol{x}, \boldsymbol{K})$ is most negative. Furthermore, recalling that $D_T(\boldsymbol{x}, \boldsymbol{K}) = \Re\left[\overline{\boldsymbol{K}} \cdot \boldsymbol{T}(\boldsymbol{x})\right]$, we will show that we can estimate, not only the location of a source, but also its direction (*i.e.* $\boldsymbol{K}$). Next, we describe the two main components of our source localization approach: 1) the computation of the source sensitivity $D_T(\boldsymbol{x}, \boldsymbol{K})$, and 2) the post-processing of this field to estimate the location and the direction of sources.

We have shown that the computation of the source sensitivity field, $D_T(\boldsymbol{x}, \boldsymbol{K})$, requires knowledge only of the adjoint field $\boldsymbol{T}$ or $\boldsymbol{\lambda}$. In general, obtaining the adjoint field requires the solution of two variational problems. Specifically, we need to first compute the state field $\boldsymbol{u}$ by solving the forward problem in (2.39), and then, knowing $\boldsymbol{u}$, we need to obtain the adjoint field $\boldsymbol{T}$ by solving the adjoint problem in (2.42). However, using the linearity of the problem, we can effectively eliminate the need for solving the forward problem by considering a source-free domain as

our base state. That is, our base state will be described by $\boldsymbol{f} = \boldsymbol{h} = \boldsymbol{0}$, implying $\boldsymbol{u} = \boldsymbol{0}$. Hence, the computation of the source sensitivity field, $D_T(\boldsymbol{x}, \boldsymbol{K})$, reduces to the solution of the adjoint problem (2.42) (with $\boldsymbol{u} = \boldsymbol{0}$) and the evaluation of (2.36).

Having obtained the adjoint field T, we can compute the source sensitivity as $D_T(\boldsymbol{x}, \boldsymbol{K}) = \Re\left[\overline{\boldsymbol{K}} \cdot \boldsymbol{T}(\boldsymbol{x})\right]$. Since $\boldsymbol{K}$ is simply the direction of the source, we can take it to be a unit vector. That is, $\boldsymbol{K} \in \{\boldsymbol{z} \in \mathbb{C}^d : |\boldsymbol{z}| = 1\}$, where d describes the dimension of the field. Intuitively, the vector $\boldsymbol{K}$ that minimizes $\Re\left[\overline{\boldsymbol{K}} \cdot \boldsymbol{T}(\boldsymbol{x})\right]$ at a point $\boldsymbol{x}$ aligns with $-\boldsymbol{T}$. Hence, we define the direction for which the source sensitivity will be minimal at a given point as

$$\boldsymbol{K}(\boldsymbol{x}) = \frac{-\boldsymbol{T}(\boldsymbol{x})}{|\boldsymbol{T}(\boldsymbol{x})|}. \tag{2.45}$$

Using (2.45) in the definition of the source sensitivity, (2.36), yields

$$\begin{aligned}
\hat{D}_T(\boldsymbol{x}) &= \min_{\boldsymbol{K}} D_T(\boldsymbol{x}, \boldsymbol{K}) \\
&= \min_{\boldsymbol{K}} \Re\left[\overline{\boldsymbol{K}}\ \boldsymbol{T}(\boldsymbol{x})\right] \\
&= \frac{-\overline{\boldsymbol{T}(\boldsymbol{x})}\boldsymbol{T}(\boldsymbol{x})}{|\boldsymbol{T}(\boldsymbol{x})|} \\
&= -|\boldsymbol{T}(\boldsymbol{x})|.
\end{aligned} \tag{2.46}$$

The above expression indicates that true sources will likely be found in regions where $|\boldsymbol{T}(\boldsymbol{x})|$ is large. Based on the approach presented in [10], we define an indicator function $D_{T\alpha}(\boldsymbol{x})$ that will allow us to identify/isolate the location of the true sources. This indicator function is defined as

$$D_{T\alpha}(\boldsymbol{x}) = \begin{cases} \hat{D}_T(\boldsymbol{x}) & \text{if } \hat{D}_T(\boldsymbol{x}) \leq \alpha \hat{D}_T^{\min}(\boldsymbol{x}) \\ 0 & \text{if } \hat{D}_T(\boldsymbol{x}) > \alpha \hat{D}_T^{\min} \end{cases} \tag{2.47}$$

where $\hat{D}_T^{\min}(\boldsymbol{x}) = \min_{\boldsymbol{x}} \hat{D}_T(\boldsymbol{x})$ and $\alpha \in (0, 1)$ is a threshold value.

Assume that, using the indicator function defined above, we have identified n regions Ω_i, $i = 1, ..., n$, that contain sources. Furthermore, assume that only one source is present in each region. Then, using Eq. (2.45), we can define an average, constant direction, $\hat{\boldsymbol{K}}_i$, for a source over region Ω_i as

$$\hat{\boldsymbol{K}}_i = -\frac{\int_{\Omega_i^\alpha} \boldsymbol{T}(\boldsymbol{x})\ d\Omega}{\left|\int_{\Omega_i^\alpha} \boldsymbol{T}(\boldsymbol{x})\ d\Omega\right|} \tag{2.48}$$

If there are multiple smaller sources in Ω_i, we will seek to reconstruct a single direction that amalgamates the contributions from the individual sources. As we will see later in Section (2.3), we may use different values of α for identifying the different regions Ω_i.

Remark 3 *In steady-state elastodynamics and acoustics, we might have information over multiple frequencies $\omega_i, i = 1, ..., m$. In this case, it is straightforward to show that we can simply add the contributions over multiple frequencies. That is, for each ω we determine $\boldsymbol{T}(\boldsymbol{x}, \omega)$ and then compute the quantities defined in* (2.46)-(2.48) *from the sum*

$$\tilde{\boldsymbol{T}}(\boldsymbol{x}) = \sum_{\omega} \boldsymbol{T}(\boldsymbol{x}, \omega). \tag{2.49}$$

We found that this approach is very effective in practice, and this is how we will use information across multiple frequencies in the numerical examples section

2.3 Numerical examples

In this section, we present numerical examples that demonstrate the salient features of the proposed source sensitivity method. To demonstrate the generality of our approach, we selected example problems from the areas of elastodynamics, acoustics, and mass transport. Furthermore, we study the performance of the

method in the face of noise, sparse information, and multiple sources, among other challenges.

In some of the examples, we added noise to the simulated data as

$$\tilde{u}_i^{\mathrm{M}} = u_i^{\mathrm{M}}(1 + \eta_i \beta) \tag{2.50}$$

where η_i are independent identically distributed standard normal random variables and β is the noise level.

2.3.1 Acoustics and elastodynamics examples

In this set of examples, we consider steady-state acoustics and elastodynamics problems. We use the same domain for all the examples in this section. Specifically, the domain for these examples is composed of a hemisphere of radius 1, symmetric about the Y axis, and extending along the negative Y axis. A radiation condition is specified on the spherical portion of the boundary to simulate a semi-infinite medium. In the subsequent examples, we considered two sets of measurement points: Set A, consisting of points arranged in 7 concentric circles on the flat portion of the boundary, and Set B, consisting points arranged in only three concentric circles. The arrangement of measurement points can be seen in Figures (2.1(a)) and (2.1(b)), respectively. The domain was finely meshed with 162,931 linear tetrahedral finite elements, and the simulated data was generated with this mesh. We then interpolated the simulated data onto a coarser mesh consisting of 53,718 linear tetrahedral elements with no *a priori* information of the true source locations. In the acoustics examples, we used a medium with unit wave speed, while in the elasticity problems we used a unit Young's modulus and a Poisson's ratio of 0.2. In all examples, we used frequencies, $\omega_i, i = 1, .., 5$, in the rage from 1

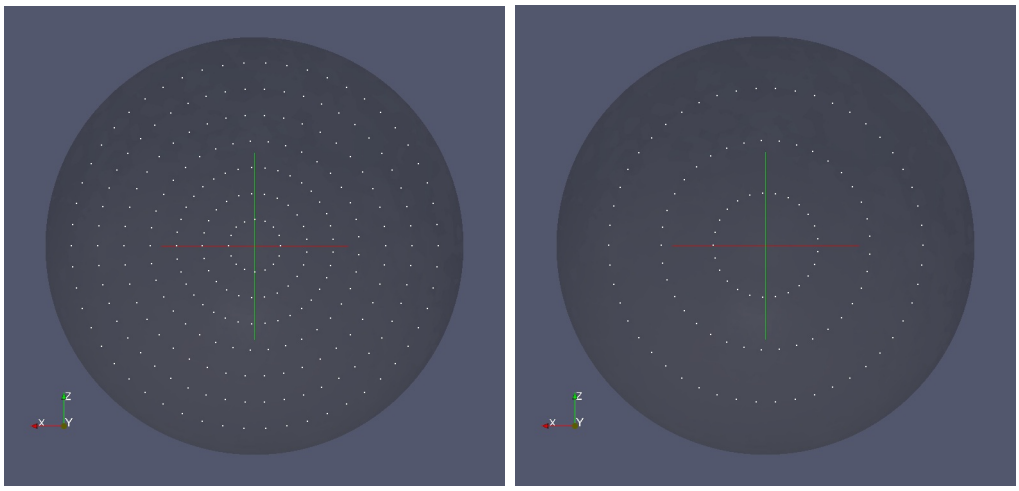

(a) Sensor Set A (b) Sensor Set B

Figure 2.1: Top view of the domain displaying the sensors locations. a) Set A: seven concentric rings of points, b) Set B: three concentric ring of points.

Experiment	α	Estimated Direction(s)	True Direction(s)
Acoustic Monopole (Dense Meas.)	0.85	$0.87 + 0.49i$	1
Acoustic Monopole (Sparse Meas.)	0.85	$0.88 + 0.47i$	1
Acoustic Monopole (Sparse Noisy Meas.)	0.85	$0.88 + 0.47i$	1
Acoustic Dipole (Sparse Noisy Meas.)	0.85	$0.86 + 0.50i$, -0.88- $0.47i$	1, -1
Elastic Dipole (Sparse Noisy Meas.)	0.85	$\begin{bmatrix} -0.02 + 0.01i \\ -0.59 + 0.17i \\ -0.74 + 0.27i \end{bmatrix}, \begin{bmatrix} 0.65 - 0.11i \\ 0.05 + 0.02i \\ 0.75 - 0.08i \end{bmatrix}$	$\begin{bmatrix} 0 \\ -0.71 \\ -0.71 \end{bmatrix}, \begin{bmatrix} 0.71 \\ 0 \\ 0.71 \end{bmatrix}$

Table 2.1: We see the list of steady state acoustic and elastic wave experiments along with reconstruction threshold α.

to 3 in intervals of 0.5.

First, we studied the reconstruction of a single volumetric source (*i.e.* monopole) in an acoustic medium using the larger measurement set (Set A), and with no noise added to the simulated data. The true source was taken as a pos-

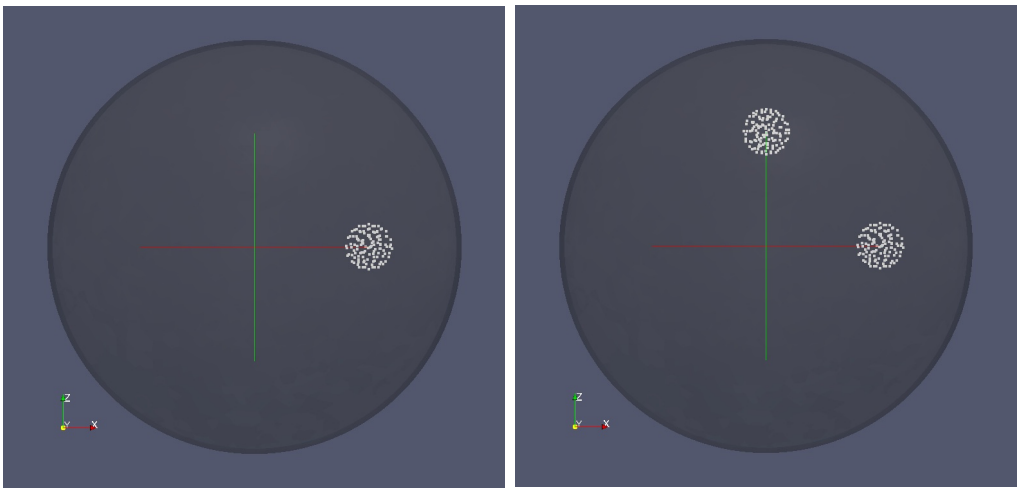

(a) Monopole Location (b) Dipole Locations

Figure 2.2: Top view of domain with monopole and dipole locations for acoustic and elasticity examples

itive, real, spherical monopole with magnitude of 10, centered at $(0.5, -0.5, 0)$, and radius of 0.1, as shown in Fig. (2.2(a)). The results of this and subsequent examples are summarized in Table 2.1. For each example, we show the threshold constant, α, the true source direction, and the estimated source direction. Figure (2.3(a)) shows a plot of the thresholded source sensitivity field (see Eq. (2.47)) overlaid on top of the true source location. We can see from the this Figure that the location of the monopole was accurately identified as the thresholded source sensitivity field coincides with the location of the true source. The latter result corresponds to a threshold constant $\alpha = 0.85$. During the course of this investigation, we studied the sensitivity of the reconstruction to different values of α and found that the identified location did not change significantly for a wide range of values of α, confirming the robustness of the method. We do not show these results herein for the sake of brevity.

We also studied the effect of reducing the number of sensor locations on the performance of the proposed algorithm. To this end, we used the sensors in Set

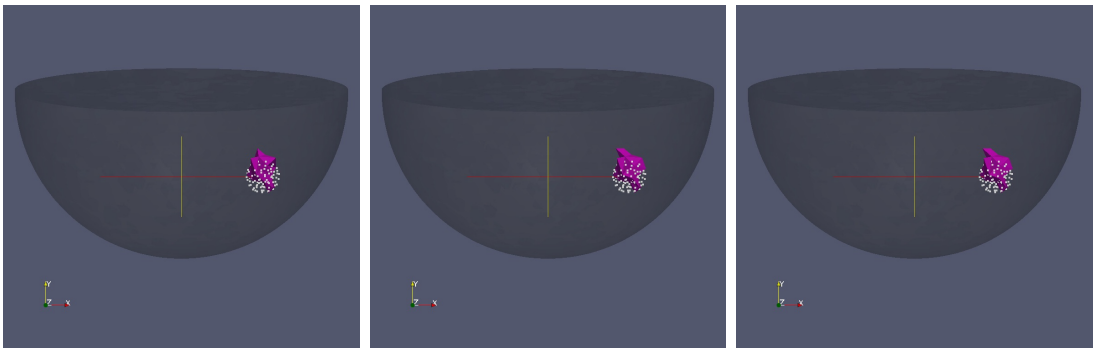

(a) Sensor Set A, no noise (b) Sensor Set B, no noise (c) Sensor Set B, 10% noise

Figure 2.3: Plot of the thresholded source sensitivity for a monopole in an acoustic medium using different combinations of sensor locations and noise levels.

B, which consisted of three concentrical rings of points on the top of the domain, and the case of a single monopole in an acoustic medium. Figure 2.3(b) shows the thresholded source sensitivity for the current case, using a value of $\alpha = 0.85$. As seen from this Figure, the algorithm was able to locate the source accurately even in this case where fewer sensors were used.

We also explored the effect of noise on the proposed algorithm. For this, we added noise to the simulated data using $\beta = 0.1$ in Eq. (2.50). For this case, we again used the single monopole from the previous cases, the sensor locations in Set B, and $\alpha = 0.85$. Figure 2.3(c) shows the thresholded field corresponding to this case (noise + sensors in Set B). We can see that, again, the source location was correctly identified, confirming the robustness of the proposed algorithm in the face of sparse sensor information and noise. We can see in Figure 2.3(c) that the source was localized with similar accuracy as for the noiseless cases. This outcome was expected as the adjoint field $\boldsymbol{T}$ is a linear function of the measurements, and Gaussian noise will not affect its expected value. Moreover, it is not difficult to show that the effect of Gaussian noise in the covariance of $\boldsymbol{T}$ is proportional to the square of the noise level (*i.e.* β^2).

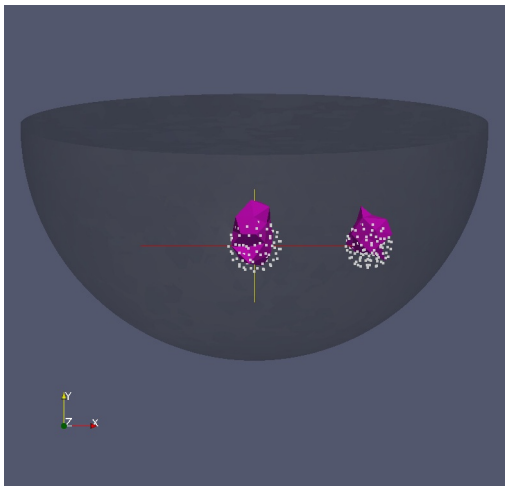

Figure 2.4: In this image we see the reconstructed location of the two acoustic monopoles from sparse, noisy measurements.

In our next acoustics example, we added a second spherical monopole centered at $(0, -0.5, 0.5)$ with a radius of 0.1. The magnitude of this second monopole was chosen to be the same as the first one (*i.e. 10*), but its direction was opposite to the first one. Figure 2.2(b) shows the position of the two monopoles considered in this example. For this example, we used the sparser set of measurements (Set B), $\alpha = 0.85$, and added noise using $\beta = 0.1$. Figure 2.4 shows the thresholded source sensitivity for the dipole reconstruction case. We observe from this Figure that the locations of the two sources were accurately reconstructed. Moreover, the directionality of the sources was also accurately estimated as seen in Table 2.1. We would like to mention that a negative sign in the context of acoustics signifies a sink, which rarely appears in practical problems. Nonetheless, we wanted to illustrate the generality of the proposed approach in identifying multiple sources and of different nature.

The next example considers the problem of source identification in an elastic medium. These problems are somewhat more complex than the acoustics ones as sources are vector-valued. For the elastic wave propagation example, we consid-

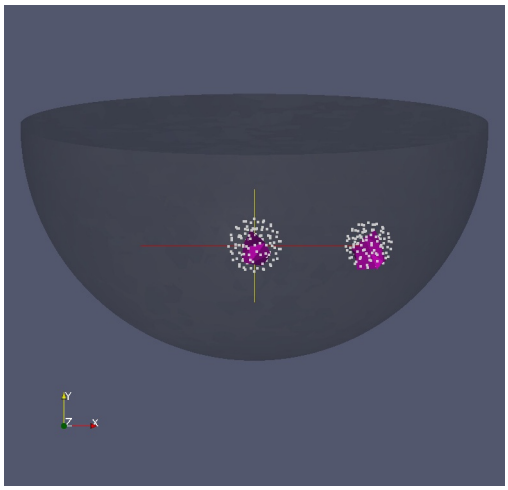

Figure 2.5: In this image we see the reconstructed location of the two elastic monopoles given sparse noisy measurements.

ered two spherical sources in the same semi-infinite domain that was used in the acoustics examples. These sources were located in the same positions as those in the last acoustics example. We took both sources as real-valued with unit magnitude. The true direction of the source located along the X axis was $(0, -1, -1)$, while the direction of the one located along the Y axis was $(1, 0, 1)$ (See Figure 2.2). We used for this case the sensor locations in Set B (three concentric circles), and assumed that displacements were measured in all three degrees of freedom at each of the sensor locations. Furthermore, we added noise to the simulated data using $\beta = 0.1$. The threshold plot for the computed source sensitivity for this case is shown in Figure 2.5. As in the previous examples, we can see from this plot that the two sources were correctly located. Moreover, we can observe in Table 2.1 that the directions of the sources were identified with reasonable accuracy. Notice that in general we take the direction $\boldsymbol{K}$ to be complex-valued, and, as expected, the imaginary component for the direction of the source in the present example is significantly smaller than the real part.

Remark 4 *We would like to point out that the concept of the Phase Conjugation Mirror (PCM) used in steady-state acoustics problems, which is analogous to Time Reversal (TR) for transient problems, has been successfully used for source reconstruction. The PCM is well established from both the theoretical and experimental points of view [38], [65], [48], [93], [31]. However, one restricting assumption required by the PCM/TR theory is that of an ergodic cavity. For instance, problems involving strongly dissipative media violate this assumption and PCM/TR methods would not perform well in this case. In contrast, our proposed approach is derived from a more general perspective and, hence, is applicable to problems where PCM/TR approaches breakdown.*

2.3.2 Advection-Diffusion

We now turn to examples drawn from the area of mass or energy transport under steady-state conditions. Specifically, we consider advection-diffusion boundary-value problems. The strong form of the forward problem was defined in (2.15)-(2.16), while the corresponding variational formulation was given in (2.17). The purpose of the examples presented in this section is to show how our proposed approach applies seamlessly to problems stemming from significantly different physical principles (*e.g.* wave propagation and mass transport). Notice that in our inverse problem formulation we assumed linearity and well-posedness of the forward variational problem in a general, abstract sense. The fundamental mathematical difference between advection-diffusion and wave propagation formulations is the presence of odd-order derivatives in advection-diffusion.

For the advection-diffusion examples, we considered a square, two-dimensional domain with dimensions 1×1. We enforced a homogeneous Dirichlet condition

over the entire boundary, and used a constant unit diffusivity. For generating the simulated data, we discretized the domain using a 200 by 200 grid of bilinear finite elements. The data was then interpolated onto a coarser 100 by 100 grid (also of bilinear elements) for solving the source localization problem. We would like to point out that this interpolation to a coarser grid represents our way of corrupting the simulated data in the advection-diffusion examples. Measurement points were taken to be in a 9 by 9 grid of points uniformly distributed over the domain. Specifically, measurement points were taken at multiples of 0.1 units in each spacial dimension.

We studied the performance of the method for various conditions, including multiple sources/sinks, different flow directions, and different Péclet numbers. We used the following definition for the Péclet number, P_e.

$$P_e = \frac{L \times \max_i |\boldsymbol{a}_i|}{D}, \tag{2.51}$$

where L is a characteristic length of the domain. In the examples presented herein, we take $L = 1$ and $D = 1$. A large Péclet number characterizes advection-dominated flows, while a low one is related to diffusion-dominated transport. In the following examples, we consider the influence of the Péclet number on the identifiability of the source location and the role of the sensor locations. A summary of the results presented in this section is given in Table 2.2.

Advection-diffusion problem with single source First, we considered a circular source located at the bottom left corner of the domain as shown in Fig. 2.6(a). The source had a radius of 0.1 and was centered at the location $(0.2, 0.2)$. The intensity of the source was taken as 10 units. The velocity field was taken as constant throughout the domain with components (1, 1), *i.e.* the flow occurred

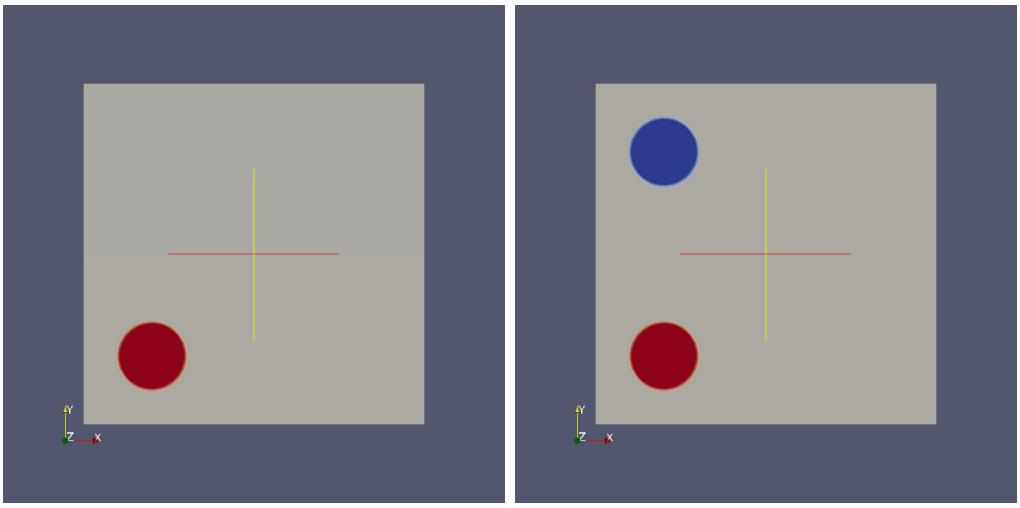

(a) Source Location (b) Source and Sink Locations

Figure 2.6: True sources used in the advection-diffusion (*transport*) examples.

Experiment	α	Estimated Direction(s)	True Direction(s)
Source, $\boldsymbol{a} = (1, 1)$	0.8	1	1
Source, $\boldsymbol{a} = (10, 10)$	0.8	1	1
Source/Sink, $\boldsymbol{a} = (1, 1)$	0.65, 0.55	1,-1	1,-1
Source/Sink, $\boldsymbol{a} = (10, 10)$	0.75, 0.2	1,-1	1,-1
Source/Sink, $\boldsymbol{a} = (10, 0)$	0.65	1,-1	1,-1

Table 2.2: We see the list of advection-diffusion experiments along with velocity $\boldsymbol{a}$ and reconstruction threshold α.

from the bottom left corner to the top right. We first consider $P_e = 1$, which we took as our lower Péclet number case.

A threshold plot of the source sensitivity field obtained for the present case and using $\alpha = 0.80$, is shown in Fig. 2.7(a). We observe that the reconstructed source location is close to the true location, but there is just a small overlap of the two regions (*i.e* true and reconstructed locations). We can conclude that for this case the source sensitivity field does not locate the true source with high accuracy. This result may be explained by the sparsity of the sensors and the diffusion-dominated

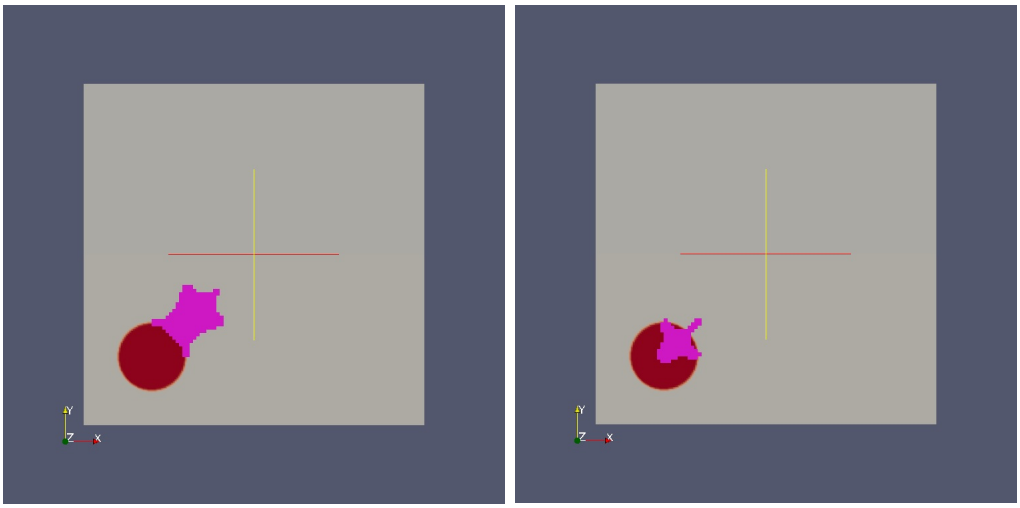

(a) $\boldsymbol{a} = (1, 1)$ (b) $\boldsymbol{a} = (10, 10)$

Figure 2.7: Threshold plots of the source sensitivity field for the advection-diffusion problem with a single source.

(*i.e.* low P_e) nature of the forward and adjoint solutions. That is, the source may be felt only by sensors in its vicinity, or in other words, the sensitivity of sensors away from the source to changes in the state variable is small. Hence, given the ill-posedness of the problem, the sensed information seem to be inadequate for an accurate reconstruction. If the later arguments are valid, we would expect that a more accurate reconstruction can be obtained either by increasing the number of sensors around the source or by increasing the Péclet number. As we will see in the next example, this is indeed the case.

We would like to point out that resolving the direction of the source (*i.e.* distinguishing between a source and a sink) is simpler in the case of advection-diffusion problems as it amounts to determining the sign of the adjoint field $\boldsymbol{T}$ in a given region. Notice that for the current example we do indeed conclude that there is a source in the bottom left corner of the domain (See Table 2.2).

We studied the case in which the flow becomes advection-dominated by in-

creasing the Péclet number by a factor of 10. Specifically, we used a velocity vector with components $(10, 10)$. As per our previous example, we expect that, in an advection-dominated flow, information can travel farther away from the source location than in a diffusion-dominated case. That is, for the the same threshold parameter and sensor placement as the diffusion-dominated case, we expect that the reconstruction accuracy in an advection-dominated flow should increase as more sensors would perceive the presence of the source. We can see from Fig. 2.7(b) that this is indeed the case. That is, the reconstructed location now intersects the support of the true source. Also, the direction of the source is correctly identified as can be seen in Table 2.2. It is important to keep in mind that the sparsity of the sensors still plays a significant role in the accuracy, which may be a reason for the small size of the reconstructed location as compared to the true source. It is expected that increasing the number of sensors would have a further positive effect on the accuracy of the solution.

Advection-diffusion problem with source and sink We now consider a problem with a source and a sink in the domain used in the previous example. The sink was modeled as a circle with radius of 0.1 units, constant intensity (-10 units), and centered at $(0.2, 0.8)$. The configuration studied in the present example can be seen in Fig. 2.6(b). First, we considered the case in which the velocity components were $(1, 1)$. Notice that locating sources and sinks using the proposed approach can be carried out in separate steps as sources are expected to be located in regions where the adjoint field, $\boldsymbol{T}$, is positive, while sinks are expected to be located in regions where this field is negative. Also, by considering positive and negative regions separately, we can use different values of the threshold parameter for each case. For the present case we used $\alpha = 0.65$ for the source and $\alpha = 0.55$

for the sink. We studied many different combinations of these values and selected these for illustration purposes only. Recall that increasing and decreasing alpha just shrinks or broadens, respectively, the support of the source/sink.

The reconstructed locations of the source and sink for the present case are shown in Fig. 2.8(a). Notice that both locations are identified correctly. Furthermore, the signs of the sources/sinks are correctly identified as can be seen in Table 2.2. As in the case of the single source, the locations of the source and sink are shifted with respect to the true ones. This result, again, may be attributed to the sensor locations and the diffusion-dominated flow.

The lower values of the thresholding parameter α used in this case reflect the fact that the contours of the adjoint field had mild slopes in the regions where they attain their extrema. The latter can be interpreted also from the point of view of lack of sensitivity, in general, of the sensed quantity to changes in the source/sink locations, which in turn, may be attributed to the combination of diffusion-dominated flow and sparsity of sensors. During the course of our numerical investigations, we noticed that the magnitudes of gradients of the adjoint field near extrema were correlated with the identifiability of sources/sinks locations. That is, when extrema of the adjoint field occurred in steep-slope regions, sources/sink supports were easily identified, while the opposite was also true. However, some mathematical analysis is needed to determine whether these observations hold in general. In spite of the lack of an analytical justification, intuitively, we can observe that high values of α should be used in regions of the adjoint field that have steep slopes, while low values should be used when gentle slopes occur. Lastly, notice that, based on the foregoing arguments and because of gentler slopes in the sink region, we have used a lower value of α for the sink (located in the top

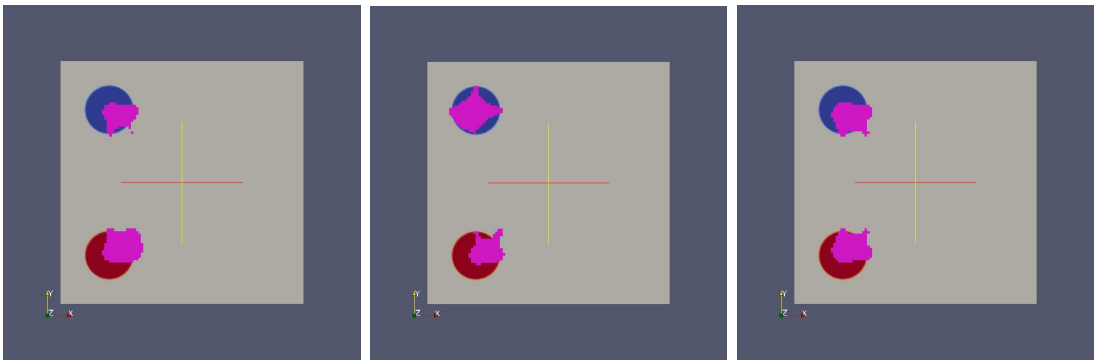

(a) $\boldsymbol{a} = (1, 1)$ (b) $\boldsymbol{a} = (10, 10)$ (c) $\boldsymbol{a} = (10, 0)$

Figure 2.8: Threshold plots of the source sensitivity for the advection-diffusion problem with a source and a sink.

left corner). Since the flow occurs from the bottom left corner to the top right, it is expected that more sensors would be affected by the source than by the sink, which is in agreement with our statements about the connection between measured information and gradients of the adjoint field in the regions where it attains its extrema.

We studied the performance of the algorithm in the face of an advection-dominated flow for the case of source/sink localization. To this end, we used a velocity field with components $(10, 10)$, which corresponds to an increase of ten fold with respect to the diffusion-dominated case used in the previous example. Fig. 2.8(b) shows a threshold plot of the source sensitivity for the present case. In this problem, we used $\alpha = 0.2$ for the negative regions of the adjoint field and $\alpha = 0.75$ for the positive regions. We can see that the locations of the source and sink were correctly identified, and, furthermore, the correct signs were identified as seen in Table 2.2.

In the present case, there was a significant difference in the values of the threshold parameter α used for the source and sink reconstructions. First notice, that

a higher α was used for the source in the present case than the one used for the same source in the diffusion-dominated case. This value of α was chosen due to the occurrence of steeper slopes of the adjoint field over regions where it attained positive values. On the other hand, a much lower value of α had to be used to locate the sink because of much gentler slopes of the adjoint field in the advection-dominated flow case. Again, these results can be explained from the sensitivity of measured quantities to the presence of the source or sink. That is, because of the flow direction (lower left corner to top right corner), the source is expected to influence a larger number of sensors (*i.e.* its information can travel farther). Intuitively, the opposite would be true for the sink since it is located in the top right corner of the domain. To further illustrate the foregoing arguments, Fig. 2.9 shows contours of the adjoint field $\boldsymbol{T}$ obtained using velocity components $(10, 10)$ (*i.e.* advection-dominated). Notice that steep gradients occur in the region of the source (lower left corner), while more gradual slopes can be seen in the area of the sink (top left corner).

As a last example, we studied the reconstruction of a source and a sink, but now considering a horizontal flow. Specifically, we used a velocity field with components $\boldsymbol{a} = (10, 0)$. Because of the symmetry in the locations of the source and sink with respect to the flow direction, we expected to observe equal influence from the source and sink over the sensed points in the domain. Hence, the magnitude of the gradients of the adjoint field in the source and sink regions were expected to be similar, and one value of α could be used for both positive and negative regions. Fig. 2.8(c) shows a threshold plot of the source sensitivity for the horizontal flow case. The reconstruction is shown for $\alpha = 0.65$. As expected, it can be observed from this plot that both locations were correctly identified using only one value of the thresholding coefficient α. Furthermore, Table 2.2 shows that the directions

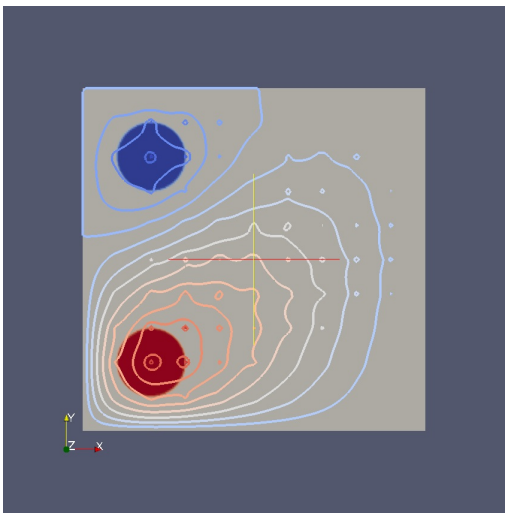

Figure 2.9: Contours of field $\boldsymbol{T}$ for the advection-diffusion example containing a source and sink, using $\boldsymbol{a} = (10, 10)$

of the source and sink were correctly identified as positive and negative signs, respectively.

2.4 Concluding Remarks

We have developed a source sensitivity strategy for the fast localization of sources in linear steady-state problems. We have shown through numerical examples that our proposed approach can be robust, tolerant to noise, and generally applicable across different physics. We demonstrated the breadth of the source sensitivity approach in examples drawn from the areas of wave propagation and advection-diffusion. Our results showed that our proposed approach can be used to identify both the location and direction (or signs in the scalar case) of sources. Moreover, we illustrated that different values of the threshold parameter, α, can be used for different localized sources. Furthermore, the level of the threshold parameter can be based on the magnitude of the gradients near the extrema of the adjoint field

(*i.e.* areas where sources are located). Although qualitative in nature, the proposed methodology can be used on its own to locate potential areas where sources reside or to establish initial guesses for other traditional optimization algorithms. In instances where high accuracy is requires, it its advantageous to use this method to seed a traditional optimization algorithm. While our proposed technique does not provide a measure of the error in the solution, using it to seed a conventional technique, such as gradient based optimization, will likely improve convergence and also provide traditional error metrics.

CHAPTER 3

A MODIFIED ERROR IN CONSTITUTIVE EQUATION APPROACH TO NONLINEAR MATERIAL IDENTIFICATION

3.1 Introduction

Material characterization is an essential component of many scientific and engineering applications. Problems ranging from damage detection, [29], [68], to biomechanical imaging, [89], [34], to finite element and material model calibration, [18], [9], all feature material characterization as a fundamental feature. Within the context of material identification, one can proceed in two distinct ways. One option is to not make any assumptions about the underlying material. Specifically, one does not constrain the connection between stress and strain. In instances where one cannot even postulate a functional form for the constitutive equation, learning techniques are promising. In [84], neural networks were used to infer the constitutive relationship. Alternatively, using a priori or expert knowledge, it is often possible to postulate a functional form for the material constitutive model of interest. Calibrating such a model, and identifying material parameters using experimental or other observations remains a challenging problem.

One can use a variety of techniques to identify material parameters, however some techniques are better suited to specific material models. Much effort has been given to the case of identifying elastic moduli. An overview of some of the available techniques for elastic reconstruction can be found in [20]. However, many phenomena are modeled using more complicated material models, such as hyperelastic, viscoelastic, and viscoplastic material models. All of these models are nonlinear in their stress-strain response. Moreover, viscoelastic and viscoplastic

demonstrate material hysteresis when observing the stress-strain response. The classical approach of postulating the identification problem mathematically as a least squares minimization problem has proven to be a very general technique, applicable for arbitrary constitutive models. Using least squares functionals has proven effective even when characterizing complex viscoplastic material models [64], [63].

For large scale problems, it is often advantageous to impose some regularity on the reconstructed solution. Various techniques exist to achieve this. A regularizer is tuned by a user, and aids a user in addressing issues commonly faced in inverse problems, such as sparse measurements, measurement noise, or solution stability [83]. Tikhonov regularization augments the objective functional with a regularization term [75], [30]. As regularizers often depend on user input, there are methods to tune a regularizer to a specific problem. One popular choice is the L-curve method [55]. Statistical regularization techniques are another robust approach, but might require assumptions about the underlying noise model, [86]. Regardless of the specific method, regularization imposes additional constraints on the inverse problem in order to bring advantageous properties to the reconstruction algorithm.

An emerging technique for both linear and nonlinear material identification is the use functionals based on the Error in Constitutive Equation (ECE). Originally, this technique was developed to quantify error in finite element solutions [60], and then adapted to material Identification, specifically in the time harmonic case [59]. The ECE method centers on weakly enforcing the material constitutive relation. Specifically, one allows errors to persist in how stress and strain are related. Identifying linear materials with static data [39], as well as nonlinear materials with quasi-static data [62] can both be achieved with this method. This class of tech-

niques is robust to noise in both the linear and nonlinear transient case [37], [69]. Analogous methods have been used in other physical and mathematical constructs aside from structural mechanics [57], [56]. The ECE and related objective functionals provide an alternative to classical least squares with several salient features, including a fundamental physical justification and intuition. Energy functionals have also been shown to have advantageous analytical properties [40]. Moreover, in heterogeneous identification problems they have been shown to accurately identify sharp material discontinuities accurately [8].

The computational framework offered by PDE constrained optimization is robust and scalable. The above techniques reformulate the material identification problem as a minimization problem through the construction of a cost functional. Once the cost functional is in hand, one can use a wide array of numerical optimization algorithms from Newton and quasi-Newton to quadratic programming and sequential quadratic programming and others [70]. One can satisfy the optimality conditions using so called full space or all-at-once approaches, [15], [77], yet for time domain problems this class of approaches requires solving coupled space-time, potentially nonlinear, systems of equations. Thus it naturally builds upon space-time finite element forward solvers. Analogously, reduced space, iterative, methods are efficient alternatives [80]. Reduced space iterative approaches can naturally adapt existing finite element modeling codes which use finite elements to discretize space and numerical integrators to march through time. The required gradient of the objective functional can be obtained by solving an adjoint equation [50]. The adjoint equation approach is efficient, scalable, and robust.

While linear material identification problems can be posed in both the frequency domain and the time domain, nonlinear material identification problems are naturally formulated in the time domain. While our formulation considers

general history-dependent nonlinear materials, we highlight the Iwan constitutive model, [82], [4], as an interesting example. Iwan models were conceived to model lap-type joint interactions. That is, they model the interface interaction between abutting three dimensional bodies. Iwan models are often used to quantify dissipative nonlinear interactions within an otherwise linear elastic structure. From a modeling perspective, one attempts to capture much of the nonlinear, complex interactions with Iwan elements, allowing the majority of the structure surrounding the joint to be modeled with simpler material types. Towards the end goal of developing a parallelized computational framework for nonlinear material identification with sparse transient data, we follow the general framework posed postulated for elastic reconstructions using the Modified Error in Constitutive Equation (MECE) technique [8]. In contrast to previous ECE formulations, this work focuses on the discretized model, postulating an analogous error in internal force computation. This approach subsequently allows us to consider arbitrary contributions to the internal force computation, *e.g.* material contributions and lap type joint interface contributions. Moreover, the internal force computation can be nonlinear, and have state dependent variables. One can add a material model to be optimized in this framework in a way that parallels how one adds a new material model in a finite element code. This framework is scalable and parallelized. While ECE techniques have been used for nonlinear material identification with transient data, the author is not aware of such a computational framework that naturally handles arbitrary three dimensional geometries.

The outline for this work will proceed by first defining the forward transient structural dynamics problem. From here we will discuss the inverse problem formulation and the ECE functional. We will discuss several points of the MECE algorithm, including selection of regularizing penalty parameter, the bidirection-

ally coupled forward and adjoint solvers, and implementation details. We will illustrate the features of the algorithm with several numerical examples, beginning with simple single element examples and extending to larger examples requiring parallel computation.

3.2 Background

3.2.1 The Forward Problem

In this section we outline the equations governing the forward evolution of (small displacement) transient structural dynamics problems. For a more complete treatment see [24]. We let Ω be an open, connected, bounded, subset of $\mathbb{R}^3$ denoting the body. We partition the surface of the body into non overlapping regions, $\partial\Omega^D$ and $\partial\Omega^N$, where we prescribe displacements and surface tractions respectively. The deformation of the body in the time interval $[0, T]$ is governed by the balance of linear momentum. We can write this system as

$$\begin{aligned}
\nabla \cdot \boldsymbol{\sigma} + \boldsymbol{b} &= \rho \ddot{\boldsymbol{u}}, \ (\boldsymbol{x}, t) \in \Omega \times (0, T] && (3.1)\\
\boldsymbol{u} &= \mathbf{0}, \ (\boldsymbol{x}, t) \in \Omega \times \{0\} && (3.2)\\
\dot{\boldsymbol{u}} &= \mathbf{0}, \ (\boldsymbol{x}, t) \in \Omega \times \{0\} && (3.3)\\
\boldsymbol{u} &= \mathbf{0}, \ \boldsymbol{x} \in \partial\Omega^D && (3.4)\\
\boldsymbol{\sigma}\boldsymbol{n} &= \boldsymbol{\tau}, \ \boldsymbol{x} \in \partial\Omega^N && (3.5)
\end{aligned}$$

where $\boldsymbol{\sigma}$ is the Cauchy stress tensor, $\boldsymbol{u}$ denotes displacement, $\boldsymbol{\tau}$ denotes surface tractions, and $\ddot{\boldsymbol{u}}$ denotes acceleration. In order to connect displacements and stress, we need a material constitutive model. For the purposes of these derivations, we

will assume the constitutive relation has the following form,

$$\boldsymbol{\sigma} = F(\boldsymbol{u}, \boldsymbol{d}; \boldsymbol{p}) \tag{3.6}$$

where $\boldsymbol{d}$ is an internal state variable and $\boldsymbol{p}$ are material parameters. Note that $\boldsymbol{F}(\cdot, \cdot, \boldsymbol{p})$ can be a first order differential operator. We do not consider case when $\boldsymbol{F}$ requires higher order derivatives of $\boldsymbol{u}$.

While we retain this generality throughout the subsequent derivations, we specifically consider linear elasticity, the generalization of Hooke's law. In this case we define the linearized strain tensor,

$$\boldsymbol{\varepsilon} = \frac{1}{2}\left(\nabla \boldsymbol{u} + \nabla \boldsymbol{u}^T\right). \tag{3.7}$$

Now we can connect the stress to the strain with the fourth order material tensor, $\boldsymbol{\mathcal{C}}$,

$$\boldsymbol{\sigma} = \boldsymbol{\mathcal{C}} : \varepsilon. \tag{3.8}$$

While the most general anisotropic case requires 21 individual material parameters to fully define $\boldsymbol{\mathcal{C}}$, we only need 2 when the material is isotropic. Specifically, when the material is isotropic, we can express stress as,

$$\boldsymbol{\sigma} = \lambda \ \mathrm{Tr}(\boldsymbol{\varepsilon}) + 2\mu\boldsymbol{\varepsilon} \tag{3.9}$$

where λ and μ are Lamé's parameters and $\mathrm{Tr}(\cdot)$ denotes the trace operator.

3.2.2 Lap Type Joint Interactions

When two independent continua or bodies are bound together at an interface, more complicated nonlinear forces can arise as a result. Lap type joints arise when two

materials overlap at an flat interface and are constrained such that components do not separate in the normal direction. Components can, however, slide tangent to the interface or rotate about the axis normal to the interface.

We have visualized an abstraction of a one dimensional lap type joint in Figure 3.1. To model this interaction we consider the Iwan joint model [81]. This model

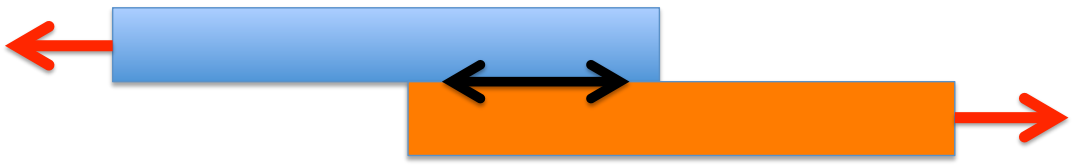

Figure 3.1: Here we see a schematic of a one dimensional lap type joint. The overlapping blue and orange bars represent the components being joined by a lap joint. The black double arrow represents the axis on which the interface interaction occurs. The red arrows represent potential applied forces.

finds applications emulating frictional interactions at structural component interfaces. The Iwan model acts in a single direction, tangent to the interaction surface. We can conceptualize this model as an infinite array of Jenkins (spring/slider) elements, with yield displacement, ϕ, distributed with some density $\psi(\phi)$. Note that the concept of a Jenkins element is distinct from the notion of a finite element. A Jenkins element is a mere abstraction of a spring/slider unit. We have visualized an abstracted Jenkins element in 3.2. Each abstract Jenkins element contains a spring, and a slider plate. We denote the displacement in the Iwan model as u_I, where the subscript I indicates that this displacement corresponds to an Iwan model. We denote the force resulting from said displacement as $f(u_I, d)$. Specifically, $f(u_I, d)$ is a scalar valued function returning force as a function of one dimensional displacement and a state variable, d. In this model $d(\phi)$ represents the slider displacement for the Jenkins elements indexed by ϕ. We can evaluate

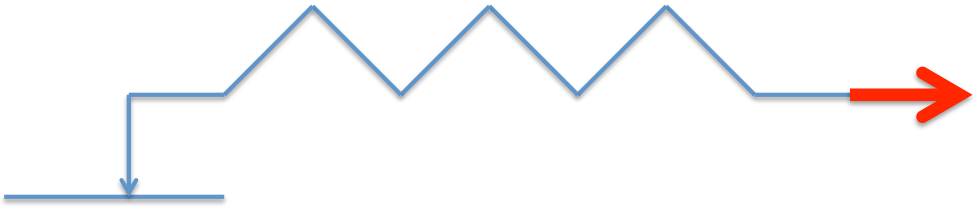

Figure 3.2: An abstract Jenkins element consists of a spring and a slider plate. The red arrow denotes the applied force.

$f(u_I, d)$ as

$$f(u_I, d) = \int_0^\infty \psi(\phi)[u_I - d(\phi)]\, d\phi \tag{3.10}$$

$$\dot{d}(\phi) = \begin{cases} \dot{u_I} & \text{if } |u_I - d(\phi)| = \phi \text{ and } \dot{u}[u_I - d(t,\phi)] > 0 \\ 0 & \text{else} \end{cases} . \tag{3.11}$$

Note that both u_i and d are formally functions of time, and these equations hold for a time slice. Intuitively, the force response of a single spring/slider element is a function of the displacement in only the spring component. It is independent of the displacement in the slider portion of the element. In the integrand of (3.10), we see the quantity $[u_I - d(\phi)]$, which is exactly the spring displacement for the Jenkins element indexed by ϕ. The force response is a sum over the force contribution from the spring component of each Jenkins element. Moreover, we can intuitively understand the evolution law in the following way. If the displacement in the spring is less than ϕ, then the slider has not reached its yield force, and the slider velocity and slider displacement does not change. Correspondingly, if the displacement in the spring is ϕ, then the slider is at the yield force. If the direction of motion is such that the displacement in the spring would increase, then the slider velocity matches the displacement velocity such that the displacement in the spring does not exceed ϕ.

In order to extend this one dimensional model, to lap joints with a two di-

mensional interaction surface, we postulate two independent Iwan models for two orthogonal directions, each tangent to the interaction surface. We assume that the frictional force in one direction is decoupled from the other. We also model the rotation about the vector normal to the interaction surface with a torsion spring.

3.2.3 Discretization

Before we derive the weak form of (3.1)-(3.5), we define the following inner products,

$$(\boldsymbol{a}, \boldsymbol{b})_T = \int_\Omega \boldsymbol{a} : \boldsymbol{b} \; d\Omega \tag{3.12}$$

where $\boldsymbol{a}, \boldsymbol{b}$ are second order tensor fields over Ω. Moreover,

$$(\boldsymbol{c}, \boldsymbol{e}) = \int_\Omega \boldsymbol{c} \cdot \boldsymbol{e} \; d\Omega \tag{3.13}$$

$$(\boldsymbol{c}, \boldsymbol{e})_{\partial\Omega} = \int_{\partial\Omega} \boldsymbol{c} \cdot \boldsymbol{e} \; d\partial\Omega \tag{3.14}$$

where $\boldsymbol{c}, \boldsymbol{e}$ are vectors. In order to derive the weak form of (3.1)-(3.5), we begin by multiplying (3.1) by a weakly differentiable test function, $\boldsymbol{\gamma} : \Omega \to \mathbb{R}^3$, and integrating by parts to obtain,

$$\int_\Omega \rho \ddot{\boldsymbol{u}} \cdot \boldsymbol{\gamma} \; d\Omega + \int_\Omega \boldsymbol{\sigma} : (\nabla \boldsymbol{\gamma}) \; d\Omega = \int_\Omega \boldsymbol{b} \cdot \boldsymbol{\gamma} + \int_{\partial\Omega^N} \boldsymbol{\tau} \cdot \boldsymbol{\gamma} \; d\partial\Omega \tag{3.15}$$

Stated in terms of inner products, we have

$$(\rho \ddot{\boldsymbol{u}}, \gamma) + (\boldsymbol{\sigma}, (\nabla \boldsymbol{\gamma}))_T = (\boldsymbol{b}, \boldsymbol{\gamma}) + (\boldsymbol{\tau}, \boldsymbol{\gamma})_{\partial\Omega} \tag{3.16}$$

We seek a finite element solution of the form

$$\boldsymbol{u}^h(t) = [N]\{u(t)\} \tag{3.17}$$

where $[N]$ denotes the matrix of shape functions and $\{u(t)\}$ denotes the nodal displacements at time t. For a fixed time t_k, we know

$$\boldsymbol{u}^h(t_k),\ \boldsymbol{\gamma} \ \in \ \mathcal{V}^h \subset \mathcal{V} = \{\boldsymbol{f} | \boldsymbol{f} \in H^1(\Omega),\ \text{and}\ \boldsymbol{f} = \boldsymbol{0}, \boldsymbol{x} \in \partial\Omega^D\} \tag{3.18}$$

where $\mathcal{V}^h$ is the finite element approximation subspace. We can denote nodal displacements at time slice t_k as $\{u\}_k = \{u(t_k)\}$. Using finite elements to discretize in space, we arrive at the following equation for every time slice.

$$[M]\{\ddot{u}_k\} + [C]\{\dot{u}_k\} + \{I_k\} = \{F\}_k \tag{3.19}$$

Here, $[M]$ is the mass matrix,

$$[M] = \sum_{\text{Elements}} \int_{\Omega^e} \rho [N^e]^T [N^e]\ d\Omega \tag{3.20}$$

and $[N^e]$ denotes the matrix of finite element shape functions for element e. We use the consistent mass matrix throughout the subsequent implementation. Note that $[C]$ is a damping matrix that arises from some dissipative constitutive models. It is common to use mass or stiffness (or some linear combination) proportional damping in modeling structures. We treat it here for the sake of completeness. Moreover, we note that $[M]$ and $[C]$ are assumed to be symmetric. $\{F\}_k$ denotes the external force vector at time slice t_k, which is determined through the body force $\boldsymbol{b}$ and the surface tractions $\boldsymbol{\tau}$. $\{I\}_k$ denotes the internal force vector at nodal values for time slice t_k. This quantity arises through the material constitutive model and other forces such as interface interactions. We will discuss the evaluation of the internal force vector in Section 3.2.4. We do note here however that $\{I\}_k$ does depend upon displacement and can be thought of as a function of $\{u\}_k$.

We use the Newmark Beta method to integrate displacements in time. Specifically, the Newmark Beta equations relate the displacement, velocity, and acceleration across time steps. We consider time slices t_k in the interval $[0, T]$, and

denote

$$\{\dot{u}\}_k = \{v\}_k \tag{3.21}$$

$$\{\ddot{u}\}_k = \{a\}_k. \tag{3.22}$$

Substituting these definitions into (3.19), we arrive at

$$[M]\{a\}_k + [C]\{v\}_k + \{I\}_k = \{F\}_k \tag{3.23}$$

The Newmark Beta method is a second order time integration method with the following scheme,

$$\{u\}_{k+1} = \{u\}_k + \Delta t\{v\}_k + \frac{\Delta t^2}{2}(1-2\beta)\{a\}_k + \beta\Delta t^2\{a\}_{k+1} \tag{3.24}$$

$$\{v\}_{k+1} = \{v\}_k + (1-\gamma)\Delta t\{a\}_k + \gamma\Delta t\{a\}_{k+1} \tag{3.25}$$

$$\{a\}_{k+1} = \frac{1}{\beta\Delta t^2}\left(\{u\}_{k+1} - \{u\}_k + \Delta t\{v\}_k + \frac{\Delta t^2}{2}(1-2\beta)\{a\}_k\right) \tag{3.26}$$

Coupling the (3.24)-(3.26) with (3.23) yields the forward solver algorithm.

Initial Conditions. We assume zero initial displacement, and velocity. We allow for nonzero initial acceleration. While in practice a nonzero initial acceleration is uncommon, it is allowed by the formulation and thus treated here. Obtaining the initial acceleration requires a linear solve with the mass matrix.

$$\{u\}_0 = \mathbf{0} \tag{3.27}$$

$$\{v\}_0 = \mathbf{0} \tag{3.28}$$

$$[M]\{a\}_0 = \{F\}_0 \tag{3.29}$$

Transition Equations We compute the displacement for the next time step using information from the previous time step. We can compute the quantities $\{\eta\}_k$ and $\{\xi\}_k$ explicitly using only the previous time step. These

quantities are computationally convent and appear on the right hand side of the transition equation for displacement.

$$\begin{aligned}\{\eta_k\} &= \{v\}_k + [\Delta t(1-\gamma)\{a\}_k \\ &\quad -\frac{\gamma}{\beta\Delta t}[\{u\}_k + \Delta t\{v\}_k] - \frac{\gamma\Delta t(1-2\beta)}{2\beta}\{a\}_k\Big] \qquad (3.30)\\ \{\xi\}_k &= \frac{1}{\beta\Delta t^2}[\{u\}_k + \{v\}_k\Delta t] + \frac{1-2\beta}{2\beta}\{a\}_k \qquad (3.31)\end{aligned}$$

From here we need to solve for the displacement at the next time step.

$$\left(\frac{1}{\beta\Delta t^2}[M] + \frac{\gamma}{\beta\Delta t}[C]\right)\boldsymbol{u}_{k+1} + \{I\}_{k+1} = \{F\}_{k+1} - [C]\{\eta\}_k + [M]\{\xi\}_k \qquad (3.32)$$

Using the displacement, we can subsequently obtain the velocity and acceleration for the next time step using the Newmark Beta equations (3.24)-(3.26).

In summary, we begin by establishing $\{u\}_0$, $\{v\}_0$, and $\{a\}_0$ through (3.27)-(3.29). Then for all other time slices, we progress from t_k to t_{k+1} by evaluating (3.30)-(3.31), and subsequently solving (3.32) for $\{u\}_{k+1}$. Note that if $\{I\}_k$ does in fact result from a nonlinear material model, we will need to use Newton or quasi-Newton iterations to solve (3.32). We will discuss further how $\{I\}_k$ is evaluated in the next section. Also, we note that while we do in fact compute velocity and acceleration at intermediate steps, this is merely a computational convenience. The algorithm is displacement driven, and does not require us to explicitly compute velocity and acceleration to transition from one time step to the next. The transition equations can be reformulated to only contain displacement.

For the sake of notational compactness we denote the discretized space-time forward equation as

$$\mathbb{N}_F\{u\} = \mathbb{F}. \qquad (3.33)$$

where $\{u\}$ denotes the space-time nodal displacement vector. In general where curly braces and a subscript denote a nodal quantity at a time slice, quantities in curly brackets without a subscript will denote the space-time nodal quantity vector. Observe that $\mathbb{N}_F$ is a nonlinear operator, and function of material parameters and Iwan parameters, denoted here in a global sense by $\underline{p} \in \mathbb{R}^p$. Also, implicit in this notation is the connection between $\{I\}_k$ and $\{u\}_k$. The right hand side of (3.33), $\mathbb{F}$ denotes the external forces arranged in a space time vector. We will discuss this connection further in the next section. A complete treatment of discretization and the finite element formulation can be found in [11].

3.2.4 The Internal Force Vector

We decompose the internal force vector in the following way,

$$\{I\}_k = \{I_\sigma\}_k + \{I_f\}_k \tag{3.34}$$

where $\{I_\sigma\}_k$ denotes the contribution from the material constitutive model, and $\{I_f\}_k$ denotes the contribution from Iwan interface interactions. Furthermore we can express,

$$\{I_\sigma\}_k = \sum_{\text{Elements}} \int_{\Omega^e} [B^e]^T \boldsymbol{\sigma}_k^e \, d\Omega \tag{3.35}$$

where $[B^e]$ denotes the matrix of derivatives of finite element shape functions for element e, and $\boldsymbol{\sigma}_k^e$ is the stress tensor expressed in Voigt notation for element e at time slice t_k. In the case of linear elasticity, $\{I_\sigma\}_k$ can be evaluated as

$$\{I_\sigma\}_k = [K]\{u\}_k \tag{3.36}$$

where $[K]$ is the stiffness matrix,

$$[K] = \sum_{\text{Elements}} \int_{\Omega^e} [B^e]^T [D^e][B^e] \, d\Omega \tag{3.37}$$

and $[D^e]$ denotes the element level stiffness matrix, derived from the constitutive equation. We assume that $[K]$ is symmetric.

For other contributions, such as Iwan joints, the internal force evaluation can not be expressed so simply. In order to model the lap joint interaction we postulate a multipoint constraint. Specifically we condense the nodes on each face to a single virtual node. We subsequently tie the corresponding degrees of freedom for these virtual nodes together with one-dimensional virtual elements. A two-dimensional interface will be condensed to two nodes, each with two displacement degrees of freedom tangent to the interface and one rotational degree of freedom about the normal direction. The normal displacement will be fixed at zero. The tangential directions are modeled with independent Iwan elements; the rotational degree of freedom is modeled with a torsion spring. The Iwan models postulated above would each apply to a virtual element. If we denote the single-dimensional force at a virtual Iwan element for a given time slice, t_k as $f_{I,k}$, we can assemble the corresponding two-dimensional nodal force vector for each element as $\{f_{I,k}, -f_{I,k}\}^T$. The assembly of these contributions to the global nodal force can be expressed as,

$$\{I_f\}_k = \sum_{\text{Elements}} \left\{ \begin{array}{c} f_{I,k} \\ -f_{I,k} \end{array} \right\}^e \tag{3.38}$$

where the superscript e denotes the element level quantity. We recall here that the Iwan model depended upon a state variable $d(\phi)$. In practice, at each Iwan element we discretize the integral over ϕ, and correspondingly evaluate $d(\phi)$ for discrete values of ϕ. The state variable is history-dependent; we use an explicit time evolution scheme to evaluate it at a given time slice. We will now summarize how to evaluate the Iwan model after discretization.

The continuous Iwan model is given by (3.10)-(3.11). The discrete evaluation is outlined in [81]. It is partly reproduced here. The Iwan model is characterized

by four parameters. We can work in one of two equivalent parameter sets. In the physical parameter set, we have $\{K_T^0, F_s, \chi, \beta_I\}$. In this space, K_T^0 is the initial tangent stiffness, F_s is the force at which all the sliders have yielded, and both χ and β_I affect energy dissipation. The equivalent, mathematically convenient, parameter set is $\{R, S, \chi, \phi^{Max}\}$. While converting to the second parameter set aids the computation, the variables are without physical interpretation. We reproduce the equations to convert parameter sets here.

$$\phi^{\text{Max}} = \frac{F_s(1+\beta_I)}{K_T\left(\beta_I + \frac{\chi+1}{\chi+2}\right)} \tag{3.39}$$

$$R = \frac{F_s(\chi+1)}{(\phi^{\text{Max}})^{\chi+2}\left(\beta_I + \frac{\chi+1}{\chi+2}\right)} \tag{3.40}$$

$$S = \left(\frac{F_s}{\phi^{\text{Max}}}\right)\left(\frac{\beta_I}{\beta_I + \left(\frac{\chi+1}{\chi+2}\right)}\right) \tag{3.41}$$

In equation (3.10), we see that the force results from an integral over the slider density. The integral over ϕ is discretized on the interval $(0, \phi^{Max}]$ in a geometric fashion. That is, interval lengths, $\Delta\phi_i$, grow as

$$\Delta\phi_{i+1} = \alpha\Delta\phi_i \tag{3.42}$$

where $\alpha > 1$. Let $\phi_{l,i}$, ϕ_i, $\phi_{r,i}$ denote the left endpoint, midpoint, and right endpoint of the i^{th} interval, respectively. Conceptually, we can now think of M discrete Jenkins elements, with increasing strengths. Denote the displacement in a given Iwan joint at time slice t_k as $u_{I,k}$. Moreover, the M dimensional state vector at time slice t_k is denoted $\underline{d}_{I,k}$. For the case of the Iwan model, the state variables corresponds to slider displacements in the individual Jenkins elements. Components of $\underline{d}_{I,k}$, or individual slider displacements at time slice t_k, are $\underline{d}_{I,k,j}$. Notice we have adorned these quantities with a subscript I, in order to denote the fact that they are Iwan element level quantities. The element level internal force

is calculated as a sum over contributions from each individual Jenkins element. In the internal Iwan computations, we have suppressed the parameters from the augments of the relevant functions. We compute the Iwan element internal force as the following sum,

$$f_{I,k}(u_{I,k}, \underline{d}_{I,k}) = \sum_{j=1}^{M} g_j(u_{I,k}, \underline{d}_{I,k,j}). \tag{3.43}$$

The contribution for the Jenkins elements indexed by $j = 1 \dots M-1$ can be computed by,

$$g_j(u_{I,k}, \underline{d}_{I,k,j}) = \begin{cases} R\frac{\phi_{r,j}^{2+\chi} - \phi_{l,j}^{2+\chi}}{2+\chi} \text{sgn}[u_{I,k} - \underline{d}_{I,k,j}] & \text{if } ||u_{I,k} - \underline{d}_{I,k,j}|| \geq \phi_j \\ R\frac{\phi_{r,j}^{1+\chi} - \phi_{l,j}^{1+\chi}}{1+\chi}[u_{I,k} - \underline{d}_{I,k,j}] & \text{if } ||u_I, k - \underline{d}_{I,k,j}|| < \phi_j \end{cases} \tag{3.44}$$

and for $j = M$, by

$$g_M(u_{I,k}, \underline{d}_{I,k,M}) = S\phi^{Max}[u_{I,k} - \underline{d}_{I,k,N}]. \tag{3.45}$$

Moreover, the discretized evolution law can be expressed as,

$$\underline{d}_{I,k+1,j} = E_I(u_{I,k+1}, \underline{d}_{I,k,j}, \phi_j) = \begin{cases} u_{I,k+1} - \phi_j & \text{if } (u_{I,k+1} - \underline{d}_{I,k,j}) \geq \phi_j \\ \underline{d}_{I,k,j} & \text{if } |u_{I,k+1} - \underline{d}_{I,k,j}| < \phi_j \\ u_{I,k+1} + \phi_j & \text{if } (u_{I,k+1} - \underline{d}_{I,k,j}) \leq -\phi \end{cases}. \tag{3.46}$$

Consistent with the continuous analogue, this evolution ensures that the displacement in the spring portion of the j^{th} Jenkins element does not exceed ϕ_j. Moreover, we observe that the force contribution from each individual Jenkins element increases linearly with displacement until the spring reaches its critical displacement, at which point there is no additional contribution as the slider portion is slipping.

An important part of the implementation is the computation of the element level tangent stiffness, required for the Newton iterations. Observe that the displacement at an element level is a scalar, and hence the tangent stiffness is also a

scalar. Specifically,

$$\frac{\partial f_{I,k}(u_{I,k}, \underline{d}_{I,k})}{\partial u_{I,k}} = \sum_{j=1}^{M} \frac{\partial g_j(u_{I,k}, \underline{d}_{I,k,j})}{\partial u_{I,k}} \tag{3.47}$$

where for $j = 1 \dots N-1$

$$\frac{\partial g_j(u_{I,k}, \underline{d}_{I,k,j})}{\partial u_{I,k}} = \begin{cases} 0 & \text{if } |u_{I,k} - \underline{d}_{I,k,j}| \geq \phi_j \\ R\frac{\phi_{r,j}^{1+\chi} - \phi_{l,j}^{1+\chi}}{1+\chi} & \text{if } |u_{I,k} - \underline{d}_{I,k,j}| < \phi_j \end{cases} \tag{3.48}$$

and for $j = N$

$$\frac{\partial g_M(u_{I,k}, \underline{d}_{I,k,M})}{\partial u_{I,k}} = \begin{cases} 0 & \text{if } |u_{I,k} - \underline{d}_{I,k,M}| \geq \phi_M \\ S\phi^{Max} & \text{if } |u_{I,k} - \underline{d}_{I,k,M}| < \phi_M \end{cases} . \tag{3.49}$$

We have computed the quantities necessary to integrate the Iwan model into the finite element forward solver. Recall the element level force is assembled into the global internal force vector through (3.38). There will be other quantities we need to compute specific to the Iwan model when we consider the inverse problem. We will compute those when they arise.

For the sake of convenience we will give the global internal force computation a functional representation. Specifically,

$$\{I\}_k = \{I_\sigma\}_k + \{I_f\}_k \tag{3.50}$$

$$= I(\{u\}_k, \underline{d}_k, \underline{p}), \tag{3.51}$$

where $I(\{u\}_k, \underline{d}_k, \underline{p})$ represents the internal force computation as a function of displacement at nodal variables, $\{u\}_k$, and internal state variables $\underline{d}_k$ at the corresponding time slice t_k. We have denoted by $\underline{d}_k \in \mathbb{R}^q$ the global vector of state variables. Moreover $\underline{d}$ without a subscript denotes the global space-time vector. Also, $I(\{u\}_k, \underline{d}_k, \underline{p})$ depends on the global material and interface parameter vector, $\underline{p}$. State variables are not nodal quantities, and moreover not all elements will have state variables. Note that $I(\{u\}_k, \underline{d}_k, \underline{p})$ assembles the contribution from the

material internal force, $\{I_\sigma\}_k$, and the interface interactions $\{I_f\}_k$. As we have introduced the state variables, we also introduce the corresponding state variable evolution equation,

$$\underline{d}_{k+1} = E(\{u\}_{k+1}, \underline{d}_k, \underline{p}). \tag{3.52}$$

Observe that the state variable is dependent upon the current displacement and the previous state variable, thus it is history-dependent. By not giving the state variable a more specific structure, we have left this formulation general to handle arbitrary history-dependent models. However, we observe for the case where $\{I\}$ is determined exclusively through linear elasticity, $I(\{u\}_k, \underline{d}_k, \underline{p})$ can be evaluated as,

$$I(\{u\}_k, \underline{d}_k, \underline{p}) = [K]\{u\}_k \tag{3.53}$$

where $[K]$ is the global stiffness matrix as in (3.37). Moreover, in this case, $\underline{d}$ does not exist and hence $E(\{u\}_{k+1}, \underline{d}_k, \underline{p})$ does not exist.

3.3 The Inverse Problem Formulation

In the previous section, we assumed that we knew material parameters, geometry, and loading completely. Conversely, for the material identification inverse problem, we assume knowledge of geometry, loading, and sparse (potentially noisy) measured displacement data, $\{u^M\}$. We assume there exists a true parameter set $\underline{p}^{\text{True}}$ and a corresponding $\boldsymbol{u}^{\text{True}}$ such that $\{u^M\}$ is a potentially noisy measurement of $\boldsymbol{u}^{\text{True}}$ at discrete points in $\overline{\Omega}$, at discrete time slices. In order to estimate the parameters, we would like to postulate an objective functional such that, when the forward fields (*e.g.* displacement) resulting from a proposed parameter set $\underline{p}^*$ match the measured quantities, the objective functional is minimized.

3.3.1 Least-Squares Approach

The classical approach towards this end is to minimize a least squares error functional,

$$\mathcal{J}_{LS}(\{u\}) = \sum_{k=1}^{N} \left|\left|\{u\}_k - \{u^M\}_k\right|\right|^2_{\Omega^M} . \tag{3.54}$$

We assume we have measurements at N time slices. Notice that we work with the discretized nodal displacements $\{u\}$. Moreover, $||\cdot||^2_{\Omega^M}$ denotes the norm squared of the argument over nodes where measurements exist. We could express this equivalently as

$$\mathcal{J}_{LS}(\{u\}) = \sum_{k=1}^{N} \left(\{u\}_k - \{u^M\}_k\right)^T [Q] \left(\{u\}_k - \{u^M\}_k\right) \tag{3.55}$$

where $[Q]$ denotes the boolean matrix indicating at which nodes measurements exist. Moreover, $\{u\}$ depends on $\underline{p}$ through the forward problem (3.33). In order to enforce this dependance, we can formulate a Lagrangian, imposing the forward model through constraint equations.

$$\begin{aligned}\mathcal{L}_{LS}(\{u\},\{v\},\{a\},\underline{d},\{\bar{u}\},\{\bar{v}\},\{\bar{a}\},\underline{\bar{d}},\underline{p}) = \\ \mathcal{J}_{LS}(\{u\}) + \mathcal{C}_{LS}(\{u\},\{v\},\{a\},\underline{d},\{\bar{u}\},\{\bar{v}\},\{\bar{a}\},\underline{\bar{d}},\underline{p})\end{aligned} \tag{3.56}$$

The functional $\mathcal{C}_{LS}(\cdot)$ enforces the constraints,

$$\begin{aligned}\mathcal{C}_{LS}(\{u\},\{v\},\{a\},\underline{d},\{\bar{u}\},\{\bar{v}\},\{\bar{a}\},\underline{\bar{d}},\underline{p}) = \\ + \{\bar{u}\}_0^T \left[[M]\{a\}_0 + [C]\{v\}_0 + I(\{u\}_0,\underline{d}_0,\underline{p}) - \{F\}_0\right] \\ + \sum_{k=0}^{N-1} \{\bar{u}\}_{k+1}^T \left[[M]\{a\}_{k+1} + [C]\{v\}_{k+1} + I(\{u\}_{k+1},\underline{d}_{k+1},\underline{p}) - \{F\}_{k+1}\right] \\ + \{\bar{v}\}_{k+1}^T [M] \left(\{v\}_{k+1} - \{v\}_k - \Delta t[(1-\gamma)\{a\}_k + \gamma\{a\}_{k+1}]\right)) \\ + \{\bar{a}\}_{k+1}^T [M] \left(\{u\}_{k+1} - \{u\}_k - \Delta t\{v\}_k - \frac{\Delta t^2}{2}[(1-2\beta)\{a\}_k + 2\beta\{a\}_{k+1}]\right) \\ + \underline{\bar{d}}_{k+1}^T \left(\underline{d}_{k+1} - E(\{u\}_{k+1},\underline{d}_k,\underline{p})\right) .\end{aligned} \tag{3.57}$$

Observe that $\{\bar{u}\}_k$ enforces (3.23), and $\{\bar{v}\}$ and $\{\bar{a}\}$ enforce the Newmark Beta time integration equations, (3.24)-(3.26). We have replaced the internal force vector $\{I\}_k$ with its functional form, $I(\{u\}_k, \underline{d}_k, \underline{p})$, from (3.51). Because we have substituted the internal force computation into the discretized governing equations for $\{I\}_k$, we need to enforce the evolution equation for the global internal state variable, $\underline{d}_k$, specifically (3.52). The state variable evolution equation is enforced by $\bar{\underline{d}}_k$, which is also in $\mathbb{R}^q$. We now can take the variations of $\mathcal{L}_{LS}(\cdot)$ with respect to the Lagrange multipliers, or adjoint variables, $\{\bar{u}\}$, $\{\bar{v}\}$, $\{\bar{a}\}$, and $\bar{\underline{d}}$. Notice the adjoint variables are adorned with an overbar. Subsequently setting these variations equal to zero for all directions, will recover the forward governing equations. For the sake of clarity, we will treat the variations at each time step separately. The way we can assemble time slices into a global space-time vector, we can similarly assemble variations at each time slice into a space time vector. We first consider the variation with respect to $\{\bar{u}\}$,

$$D\mathcal{L}_{LS} \cdot \{\delta\bar{u}\} = 0, \ \forall\{\delta\bar{u}\} \tag{3.58}$$

For the corresponding time slices, this yields,

$$[M]\{a\}_k + [C]\{v\}_k + I(\{u\}_k, \underline{d}_k, \underline{p}) = \{F\}_k \tag{3.59}$$

We now consider the Newmark Beta equations. Specifically we take the variations with respect to $\{\bar{v}\}$ and $\{\bar{a}\}$,

$$D\mathcal{L}_{LS} \cdot \{\delta\bar{v}\} = 0, \ \forall\{\delta\bar{u}\} \tag{3.60}$$

$$D\mathcal{L}_{LS} \cdot \{\delta\bar{a}\} = 0, \ \forall\{\delta\bar{u}\} \tag{3.61}$$

which will respectively yield for each time step,

$$\{v\}_{k+1} = \{v\}_k + \Delta t[(1-\gamma)\{a\}_k + \gamma\{a\}_{k+1}]) \tag{3.62}$$

$$\{u\}_{k+1} = \{u\}_k + \Delta t\{v\}_k + \frac{\Delta t^2}{2}[(1-2\beta)\{a\}_k + 2\beta\{a\}_{k+1}]) \tag{3.63}$$

$$\tag{3.64}$$

Finally, we consider the state variable equation, through the variation with respect to $\underline{d}$

$$D\mathcal{L}_{LS} \cdot \delta\bar{\underline{d}} \;\; = \;\; 0, \; \forall \delta\bar{\underline{d}} \tag{3.65}$$

which yields,

$$\underline{d}_{k+1} = E(\{u\}_{k+1}, \underline{d}_k, \underline{p}). \tag{3.66}$$

Combining (3.59) with (3.62), (3.63), and (3.66) will yield the exact same forward solution routine implied by (3.33).

We proceed now to take the variations with respect to the forward variables, $\{u\}$, $\{v\}$, $\{a\}$, and $\underline{d}$. We begin with $\{u\}$, which yields,

$$\begin{aligned} D\mathcal{L}_{LS} \cdot \{\delta u\}_k = & \left([M](\{\bar{a}\}_k - \{\bar{a}\}_{k+1}) + [K_T^k]^T\{\bar{u}\}_k \right. \\ & \left. + [Q](\{u\}_k - \{u^M\}_k) - \left[\frac{\partial E(\{u\}_k, \underline{d}_{k-1}, \underline{p})}{\partial \{u\}_k}\right]^T \bar{\underline{d}}_k \right)^T \{\delta u\}_k \end{aligned} \tag{3.67}$$

and for the final time step,

$$\begin{aligned} D\mathcal{L}_{LS} \cdot \{\delta u\}_N = & \left([M]\{\bar{a}\}_N + [K_T^N]^T\{\bar{u}\}_N \right. \\ & \left. + [Q](\{u\}_N - \{u^M\}_N) - \left[\frac{\partial E(\{u\}_N, \underline{d}_{N-1}, \underline{p})}{\partial \{u\}_N}\right]^T \bar{\underline{d}}_N \right)^T \{\delta u\}_N. \end{aligned} \tag{3.68}$$

We use $[K_T^k]$ to denote the tangent stiffness at time slice t_k, or specifically,

$$[K_T^k] = \frac{\partial I(\{u\}_k, \underline{d}_k, \underline{p})}{\partial \{u\}_k}. \tag{3.69}$$

We assume $[K_T^k]$ is a symmetric matrix. Next we consider the variation with respect to velocity, which implies for all but the final time step,

$$\begin{aligned} & D\mathcal{L}_{LS} \cdot \{\delta v\}_k = \\ & \qquad \left([C]\{\bar{u}\}_k - \Delta t[M]\{\bar{a}\}_{k+1} + [M]\{\bar{v}\}_k - [M]\{\bar{v}\}_{k+1}\right)^T \{\delta v\}_k \end{aligned} \tag{3.70}$$

and for the final time step,

$$D\mathcal{L}_{LS} \cdot \{\delta v\}_N = \left([C]\{\bar{u}\}_N + [M]\{\bar{v}\}_N\right)^T \{\delta v\}_N. \tag{3.71}$$

When we take the variation with respect to acceleration, we find three separate cases. For the initial time step, we find

$$D\mathcal{L}_{LS} \cdot \{a\}_0 = \left([M]\{\bar{u}\}_0 - \frac{\Delta t^2}{2}(1-2\beta)[M]\{\bar{a}\}_1 - \Delta t(1-\gamma)[M]\{\bar{v}\}_1\right)^T \{\delta a\}_0. \tag{3.72}$$

For the intermediate time step we have,

$$D\mathcal{L}_{LS} \cdot \{a\}_k = \Bigg([M]\{\bar{u}\}_k - \beta\Delta t^2[M]\{\bar{a}\}_k - \frac{\Delta t^2}{2}(1-2\beta)[M]\{\bar{a}\}_{k+1} - \Delta t(1-\gamma)[M]\{\bar{v}\}_{k+1} - \Delta t\gamma[M]\{\bar{v}\}_k\Bigg)^T \{\delta a\}_k. \tag{3.73}$$

For the final time step, we get,

$$D\mathcal{L}_{LS} \cdot \{a\}_N = \left([M]\{\bar{u}\}_N - \Delta t^2\beta[M]\{\bar{a}\}_N - \Delta t\gamma[M]\{\bar{v}\}_N\right)^T \{\delta a\}_N. \tag{3.74}$$

Finally, we consider the variation with respect to the state variable, for all but the final time step, we find

$$D\mathcal{L}_{LS} \cdot \delta\underline{d}_k = \left(\left[\frac{\partial I(\{u\}_k, \underline{d}_k, \underline{p})}{\partial \underline{d}_k}\right]^T \{\bar{u}\}_k + \bar{\underline{d}}_k - \left[\frac{\partial E(\{u\}_{k+1}, \underline{d}_k, \underline{p})}{\partial \underline{d}_k}\right] \bar{\underline{d}}_{k+1}\right)^T \delta\underline{d}_k \tag{3.75}$$

and for the final time step we get,

$$D\mathcal{L}_{LS} \cdot \delta\underline{d}_N = \left(\left[\frac{\partial I(\{u\}_N, \underline{d}_N, \underline{p})}{\partial \underline{d}_N}\right]^T \{\bar{u}\}_N + \bar{\underline{d}}_N\right)^T \delta\underline{d}_N. \tag{3.76}$$

Setting the variations with respect to the forward variables equal to zero for all directions will yield the adjoint governing equations. We observe that the variations with respect to each of the forward fields had a different solution in the final time step. These final time step variations yield final conditions. The solution method evolves backwards in time. We outline here the solution algorithm.

Final Conditions. We observe that the variations for the forward variables in the final time step yield equations are only in terms of final time step quantities. Thus, in setting these variations, (3.74), (3.71), (3.68) and (3.76), equal to zero, we can derive the final conditions.

$$[C]\{\bar{u}\}_N + [M]\{\bar{v}\}_N = 0 \tag{3.77}$$

$$\{\bar{u}\}_N = \Delta t^2 \beta \{\bar{a}\}_N + \Delta t \gamma \{\bar{v}\}_N \tag{3.78}$$

$$\bar{\underline{d}}_N = -\left[\frac{\partial I(\{u\}_N, \underline{d}_N, \underline{p})}{\partial \underline{d}_N}\right]^T \{\bar{u}\}_N \tag{3.79}$$

$$[M]\{\bar{a}\}_N + [K_T^N]^T\{\bar{u}\}_N - \left[\frac{\partial E(\{u\}_N, \underline{d}_{N-1}, \underline{p})}{\partial \{u\}_N}\right]^T \bar{\underline{d}}_N = [Q](\{u^M\}_N - \{u\}_N) \tag{3.80}$$

Transition Equations The variations for intermediate time steps, (3.73), (3.70), (3.67) and (3.75), yield the adjoint transition equations.

$$\{\bar{u}\}_k - \beta \Delta t^2 \{\bar{a}\}_k - \Delta t \gamma \{\bar{v}\}_k = \frac{\Delta t^2}{2}(1-2\beta)\{\bar{a}\}_{k+1} + \Delta t(1-\gamma)\{\bar{v}\}_{k+1} \tag{3.81}$$

$$[C]\{\bar{u}\}_k + [M](\{\bar{v}\}_k - \Delta t\{\bar{a}\}_{k+1} - \{\bar{v}\}_{k+1}) = 0 \tag{3.82}$$

$$\underline{d}_k = -\left[\frac{\partial I(\{u\}_k, \underline{d}_k, \underline{p})}{\partial \underline{d}_k}\right]^T \{\bar{u}\}_k + \left[\frac{\partial E(\{u\}_{k+1}, \underline{d}_k, \underline{p})}{\partial \underline{d}_k}\right]^T \bar{\underline{d}}_{k+1} \tag{3.83}$$

$$[M]\{\bar{a}\}_k + [K_T^k]^T\{\bar{u}\}_k - \left[\frac{\partial E(\{u\}_k, \underline{d}_{k-1}, \underline{p})}{\partial \{u\}_k}\right]^T \bar{\underline{d}}_k = [M]\{\bar{a}\}_{k+1} + [Q](\{u^M\}_k - \{u\}_k) \tag{3.84}$$

Final Transition Equation We use the variation with respect to the initial acceleration, (3.72), to derive the final transition equation.

$$\{\bar{u}\}_0 = \frac{\Delta t^2}{2}(1-2\beta)\{\bar{a}\}_1 + \Delta t(1-\gamma)\{\bar{v}\}_1 \tag{3.85}$$

Thus the adjoint equations depend on the forward variables in several ways. The derivatives of the internal force computation, $I(\{u\}_k, \underline{d}_k, \underline{p})$, depend on forward variables and appear in several equations. Specifically, the tangent stiffness appears in (3.80) and (3.84). The derivative of internal force with respect to the state variables appears in (3.79) and (3.83). Moreover, if the constitutive model requires an evolution equation, $E(\{u\}_{k+1}, \underline{d}_k, \underline{p})$, the derivatives of the evolution equation appear in several equations as well. The derivative of the evolution equation with respect to the displacement also appears in (3.80) and (3.84). The derivative of the evolution equation with respect to the state variables also appears in (3.84). Finally (3.84) also depends on the forward displacement directly through the error mismatch term, $[Q](\{u^M\}_k - \{u\}_k)$. From these final conditions and transition equations, we can derive the following algorithm. For the final time step, solve

$$\left(\frac{1}{\beta\Delta t^2}[M] + \frac{\gamma}{\beta\Delta t}[C] + [K_T^N]^T + \left[\frac{\partial E(\{u\}_N, \underline{d}_{N-1}, \underline{p})}{\partial \underline{u}_N}\right]^T \left[\frac{\partial I(\{u\}_N, \underline{d}_N, \underline{p})}{\partial \underline{d}_N}\right]^T\right)\{\bar{u}\}_N = [Q](\{u^M\}_N - \{u\}_N) \tag{3.86}$$

Update $\bar{\underline{d}}_N$, $\{\bar{a}\}_N$, and $\{\bar{v}\}_N$ through (3.77)-(3.79) using $\{\bar{u}\}_N$. For previous time steps, solve

$$\begin{aligned}\left(\frac{1}{\beta\Delta t^2}[M] + \frac{\gamma}{\beta\Delta t}[C] + [K_T^K]^T + \left[\frac{\partial E(\{u\}_k, \underline{d}_{k-1}, \underline{p})}{\partial \underline{u}_k}\right]^T \left[\frac{\partial I(\{u\}_k, \underline{d}_k, \underline{p})}{\partial \underline{d}_k}\right]^T\right)\{\bar{u}\}_k = \\ [M]\left(\frac{2\gamma+1}{2\beta}\{\bar{a}\}_{k+1} + \frac{1}{\beta\Delta t}\{\bar{v}\}_{k+1}\right) + [Q](\{u^M\}_k - \{u\}_k) \\ + \left[\frac{\partial E(\{u\}_k, \underline{d}_{k-1}, \underline{p})}{\partial \{u\}_k}\right]^T \left[\frac{\partial E(\{u\}_{k+1}, \underline{d}_k, \underline{p})}{\partial \underline{d}_k}\right]^T \bar{\underline{d}}_{k+1}\end{aligned} \tag{3.87}$$

and update $\underline{\bar{d}}_k$, $\{\bar{a}\}_k$, and $\{\bar{v}\}_k$ through (3.81)-(3.84) using $\{\bar{u}\}_k$. For the initial time step, solve

$$[M]\{\bar{u}\}_0 = \frac{\Delta t^2}{2}(1-2\beta)[M]\{\bar{a}\}_1 + \Delta t(1-\gamma)[M]\{\bar{v}\}_1 \tag{3.88}$$

Now we will derive the element level quantities corresponding to $\frac{\partial I}{\partial \boldsymbol{d}_k}$, $\frac{\partial E}{\partial \boldsymbol{d}_k}$, and $\frac{\partial E}{\partial \boldsymbol{u}_k}$ for the Iwan constitutive models. Observe that for linear elastic elements, these quantities are all zero, as there is no state variable and no state evolution equation. Moreover, the tangent stiffness in the linear elastic case is simply the stiffness. We have shown the tangent stiffness computation for the Iwan elements in Section 3.2.4. Recall for Iwan elements, we can define the element level internal force and state evolution by (3.43) and (3.46) respectively.

We begin by considering the derivative of the internal force with respect to the evolution parameter. At an element level, this quantity is a $M \times 1$ vector, where M is the dimension of $\underline{d}_{I,k}$, or the number of Jenkins elements in the discretized Iwan model. Recall this comes from discretizing the integral in the internal force computation over ϕ. The discretized internal force computation, (3.43), involves a sum over the discrete Jenkins elements, and the j^{th} term depends only on the j^{th} component of $\underline{d}_{I,k}$, *i.e.* $\underline{d}_{I,k,j}$. Specifically, we have,

$$\left[\frac{\partial f_I(u_{I,k}, \underline{d}_{I,k})}{\partial \underline{d}_{I,k}}\right]_j = \left(\frac{\partial f_j(u_{I,k}, \underline{d}_{I,k,j})}{\partial \underline{d}_{I,k,j}}\right) \tag{3.89}$$

where the subscript j on the left hand side of (3.89) denotes the j^{th} entry of the vector. The right hand side can be evaluated for $j = 1 \ldots N-1$ as

$$\frac{\partial g_j(u_{I,k}, \underline{d}_{I,k,j})}{\partial \underline{d}_{I,k,j}} = \begin{cases} 0 & \text{if } |u_{I,k} - \underline{d}_{I,k,j}| \geq \phi_j \\ -R\frac{\phi_{r,j}^{1+\chi} - \phi_{l,j}^{1+\chi}}{1+\chi} & \text{if } |u_{I,k} - \underline{d}_{I,k,j}| < \phi_j \end{cases} \tag{3.90}$$

and for $j = M$

$$\frac{\partial g_M(u_{I,k}, \underline{d}_{I,k,M})}{\partial \underline{d}_{I,k,M}} = \begin{cases} 0 & \text{if } |u_{I,k} - \underline{d}_{I,k,M}| \geq \phi_M \\ -S\phi^{Max} & \text{if } |u_{I,k} - \underline{d}_{I,k,M}| < \phi_M \end{cases}. \tag{3.91}$$

Next, we consider the derivative of the state evolution equation with respect to the displacement. At an element level, this quantity is an $M \times 1$ vector, and can be computed from 3.46,

$$\left[\frac{\partial E_I(u_{I,k+1}, \underline{d}_{I,k})}{\partial u_{I,k}}\right]_j = \begin{cases} 1 & \text{if } |u_{I,k+1} - \underline{d}_{I,k,j}| \geq \phi_j \\ 0 & |u_{I,k+1} - \underline{d}_{I,k,j}| < \phi_j \end{cases} . \tag{3.92}$$

Again the subscript j on the left hand side of (3.92) denotes the j^{th} entry of the vector. Finally, we compute the derivative of the state evolution equation with respect to the state variables. At an element level, this quantity is in fact an $M \times M$ matrix. It is, however, diagonal. Intuitively, we see that the j^{th} component of $\underline{d}_{I,k+1}$ only depends upon the j^{th} component of $\underline{d}_{I,k}$. We can express the components of this derivative as

$$\left[\frac{\partial E_I(u_{I,k+1}, \underline{d}_{I,k})}{\partial \underline{d}_{I,k}}\right]_{j,l} = \delta_{jl} \cdot \begin{cases} 0 & \text{if } |u_{I,k+1} - \underline{d}_{I,k,j}| \geq \phi_j \\ 1 & |u_{I,k+1} - \underline{d}_{I,k,j}| < \phi_j \end{cases} . \tag{3.93}$$

where the subscript j, l on the left hand side of (3.93) denotes the index in the matrix. We observe that in equations (3.86) and (3.87), we require the product

$$\left[\frac{\partial E_I(u_{I,k}, \underline{d}_{I,k-1})}{\partial u_{I,k}}\right]^T \left[\frac{\partial f_I(u_{I,k}, \underline{d}_{I,k})}{\partial \underline{d}_{I,k}}\right]^T . \tag{3.94}$$

We want to show that this product is always zero for the case of the Iwan model. This term also does not appear in the linear elastic case, as there is no state variables and no evolution equation in this case. We begin by observing that at a given Iwan element, these terms are a $1 \times M$ vector and an $M \times 1$ vector. Thus the product is a scalar,

$$\left[\frac{\partial E_I(u_{I,k}, \underline{d}_{I,k-1})}{\partial u_{I,k}}\right]^T \left[\frac{\partial f_I(u_{I,k}, \underline{d}_{I,k})}{\partial \underline{d}_{I,k}}\right]^T = \sum_{j=1}^{N} \left[\frac{\partial E_I(u_{I,k}, \underline{d}_{I,k-1})}{\partial u_{I,k}}\right]_j \left[\frac{\partial f_I(u_{I,k}, \underline{d}_{I,k})}{\partial \underline{d}_{I,k}}\right]_j \tag{3.95}$$

We want to show that each term in the sum is in fact zero. For each term in the sum, we consider the two possible cases.

Case 1: $\underline{d}_{I,k,j} = \underline{d}_{I,k-1,j}$. In this case the product is either

$$0 \cdot \left[\frac{\partial g_j(u_{I,k}, \underline{d}_{I,k,j})}{\partial \underline{d}_{I,k,j}}\right] \tag{3.96}$$

or

$$\left[\frac{\partial E_I(u_{I,k}, \underline{d}_{I,k-1})}{\partial u_{I,k}}\right]_j \cdot 0 \tag{3.97}$$

Case 2: $\underline{d}_{I,k,j} \neq \underline{d}_{I,k-1,j}$. In this case, $\underline{d}_{I,k,j} = u_{I,k} \pm \phi_j$ and $|u_{I,k} - \underline{d}_{I,k,j}| = \phi_j$. Therefore

$$\left[\frac{\partial g_j(u_{I,k}, \underline{d}_{I,k,j})}{\partial \underline{d}_{I,k,j}}\right] = 0 \tag{3.98}$$

and the product equals zero.

Both of these cases result in each term being zero. Thus the sum is zero, and the product

$$\left[\frac{\partial E_I(u_{I,k}, \underline{d}_{I,k-1})}{\partial u_{I,k}}\right]^T \left[\frac{\partial f_I(u_{I,k}, \underline{d}_{I,k})}{\partial \underline{d}_{I,k}}\right]^T = 0. \tag{3.99}$$

Thus for the case when there are only linear elastic or Iwan models present, we can simplify (3.86) and (3.87) in the adjoint algorithm to

$$\left(\frac{1}{\beta \Delta t^2}[M] + \frac{\gamma}{\beta \Delta t}[C] + [K_T^N]^T\right)\{\bar{u}\}_N = [Q](\{u^M\}_N - \{u\}_N) \tag{3.100}$$

and

$$\begin{aligned}\left(\frac{1}{\beta \Delta t^2}[M] + \frac{\gamma}{\beta \Delta t}[C] + [K_T^k]^T\right)\{\bar{u}\}_k = \\ [M]\left(\frac{2\gamma+1}{2\beta}\{\bar{a}\}_{k+1} + \frac{1}{\beta \Delta t}\{\bar{v}\}_{k+1}\right) + [Q](\{u^M\}_k - \{u\}_k) \\ + \left[\frac{\partial E(\{u\}_k, \underline{d}_{k-1}, \underline{p})}{\partial \{u\}_k}\right]^T \left[\frac{\partial E(\{u\}_{k+1}, \underline{d}_k, \underline{p})}{\partial \underline{d}_k}\right]^T \bar{\underline{d}}_{k+1}\end{aligned} \tag{3.101}$$

respectively. Observe however that, the right hand side of (3.101) still contains derivatives of the evolution equation in the term,

$$\left[\frac{\partial E(\{u\}_k, \underline{d}_{k-1}, \underline{p})}{\partial \{u\}_k}\right]^T \left[\frac{\partial E(\{u\}_{k+1}, \underline{d}_k, \underline{p})}{\partial \underline{d}_k}\right]^T \bar{\underline{d}}_{k+1}. \tag{3.102}$$

This term does not equal zero, and cannot be ignored. Again, at linear elastic elements, it is zero, as there is no state evolution equation or state variable. In Iwan elements,

$$\left[\frac{\partial E_I(u_{I,k}, \underline{d}_{I,k-1})}{\partial u_{I,k}}\right]^T \left[\frac{\partial E_I(u_{I,k+1}, \underline{d}_{I,k})}{\partial \underline{d}_{I,k}}\right]^T \tag{3.103}$$

is a $1 \times M$ vector times an $M \times M$ matrix. Appropriately, $\bar{\underline{d}}_{I,k+1}$ is an $M \times 1$ vector for each Iwan element. Notice here we have considered an adjoint state variable at an element level, hence the subscripted I. The product of (3.103) and $\bar{\underline{d}}_{I,k+1}$ is a scalar at the element level. In practice we assemble the element level contributions analogous to (3.38). If we look at the product of the first two terms, we can isolate when it is nonzero. Recall that

$$\left[\frac{\partial E_I(u_{I,k+1}, \underline{d}_{I,k})}{\partial \underline{d}_{I,k}}\right]^T \tag{3.104}$$

is a diagonal matrix, and thus

$$\left[\left[\frac{\partial E_I(u_{I,k}, \underline{d}_{I,k-1})}{\partial u_{I,k}}\right]^T \left[\frac{\partial E_I(u_{I,k+1}, \underline{d}_{I,k})}{\partial \underline{d}_{I,k}}\right]^T\right]_j = \begin{cases} 1 & |u_{I,k} - \underline{d}_{I,k-1}| \geq \phi_j \text{ and } |u_{I,k+1} - \underline{d}_{I,k}| < \phi_j \\ 0 & \text{else} \end{cases} \tag{3.105}$$

We can conceptualize the condition for which this evaluates to 1. Entries j corresponding to sliders that were slipping in the t_k^{th} time step, but are not slipping in the next, t_{k+1}^{th}, time step will have a 1. Other entries will be 0. This can happen exclusively when the velocity in the Iwan element changes direction. We observe that (3.79) and (3.84) do not imply that $\bar{\underline{d}}_{I,k+1}$ is zero. In fact, in real simulations,

this term can be substantial. Thus we need to consider this product in the adjoint equations when Iwan elements are present.

Similar to (3.33), we denote the discrete space-time adjoint equation as

$$\mathbb{N}_A\{\bar{u}\} = \mathbb{Q}\left(\{u^M\} - \{u\}\right) \tag{3.106}$$

where $\mathbb{Q}$ denotes a space-time block boolean matrix indicating where measurements exist. The process of solving for $\{\bar{u}\}$ is equivalent to solving a partial differential equation. Although the forward operator, $\mathbb{N}_F$, can be nonlinear, the adjoint operator, $\mathbb{N}_A$, is in fact always linear. Given the coupling of the adjoint equation to the forward equation, $\boldsymbol{u}$ and $\bar{\boldsymbol{u}}$ satisfy the triangular space-time coupled system,

$$\begin{bmatrix} \mathbb{N}_F & 0 \\ \mathbb{Q} & \mathbb{N}_A \end{bmatrix} \begin{Bmatrix} \{u\} \\ \{\bar{u}\} \end{Bmatrix} = \begin{Bmatrix} \mathbb{F} \\ \mathbb{Q}\{u^M\} \end{Bmatrix}. \tag{3.107}$$

This system can be solved sequentially for the solution $\{u\}^*$ and $\{\bar{u}\}^*$. At the solution point, we can compute $D\mathcal{L}_{LS} \cdot \delta\underline{p}$, and

$$\begin{aligned} D\mathcal{J}_{LS} \cdot \delta\underline{p} &= D\mathcal{L}_{LS} \cdot \delta\underline{p} && (3.108) \\ &= \sum_{k=0}^{N} \{\bar{u}\}_k^T \left[\frac{\partial I(\{u\}_k, \underline{d}_k, \underline{p}_k)}{\partial \underline{p}_k}\right] \delta\underline{p} \\ &\quad + \sum_{k=0}^{N-1} \underline{\bar{d}}_{k+1}^T \left[\frac{\partial E(\{u\}_{k+1}, \underline{d}_k, \underline{p}_k)}{\partial \underline{p}_k}\right] \delta\underline{p}. && (3.109) \end{aligned}$$

Once we are equipped with the gradient of the objective functional with respect to $\underline{p}$ we can apply one of many methods to find the solution to the optimization problem. Many of these methods are outlined in [70]. quasi-Newton methods are popular options as they are simpler to implement, especially in larger more complex codes. One can also proceed with a Newton or Gauss-Newton scheme, but this would require second derivatives, or approximations thereof. As the Hessian matrix is typically dense, it is common to implement the application of the Gauss-Newton

approximation to the inverse of the Hessian matrix. This again requires subsequent forward and adjoint solves. In contrast to this approach is an emerging technique based on an Error in Constitutive Equation objective functional. In the next section we will postulate a new objective functional and minimize it in an iterative pattern whereby we satisfy forward and adjoint operators, and subsequently update the material parameters.

3.3.2 Modified Error in Constitutive Equation

We postulate a different objective functional, seeking not only to minimize the error in the measured data, but also the error in the constitutive equation. In other applications of this technique, one postulates a mismatch of the material constitutive law and the stress tensor. Rather than work at a material point, we postulate the mismatch between the internal force vector, and the corresponding function that is used to evaluate internal force. Specifically, the error in internal force objective functional, which is analogous to the error in constitutive equation functional found elsewhere in the literature [37], [69], [8], is

$$\mathcal{U}(\{u\}, \underline{d}, \{I\}, \underline{p}) = \frac{1}{2} \sum_{k=1}^{N} \left(\{I\}_k - I(\{u\}_k, \underline{d}_k, \underline{p})\right)^T [A] \left(\{I\}_k - I(\{u\}_k, \underline{d}_k, \underline{p})\right). \quad (3.110)$$

Notice that $I(\{u\}_k, \underline{d}_k, \underline{p})$ is as defined in the previous section, *i.e.* it is the evaluation of the assembled internal force vector, including material and interface contributions, given nodal displacement, state variables and parameters at a given time slice, t_k. We select the matrix $[A]$ such that $\mathcal{U}$ is scaled appropriately. Choosing $[A] = [K_T^0]^{-1}$, the inverse of the initial global tangent stiffness matrix, provides reasonable scaling and generalizes the ECE functional used in the elastic case [8].

Specifically, this is the tangent stiffness evaluated at the initial conditions. This amounts to a weak enforcement of the internal force evaluation. In postulating this functional, we are allowing some error to persist in the relation between internal forces and the function by which it is evaluated. This is advantageous particularly when seeking to identify material parameters. If we are seeking material parameters, we may not know the constitutive equation exactly. Therefore we do not want to impose the constitutive equation strongly, as there is some uncertainty in it. We form the analog to the Modified Error in Constitutive Equation functional by adding the error in internal force objective functional, $\mathcal{U}$, and a scaled least squares functional,

$$\mathcal{M}(\{u\}) = \frac{1}{2}\sum_{k=1}^{N}\left(\{u\}_k - \{u^M\}_k\right)^T [Q]\left(\{u\}_k - \{u^M\}_k\right) \tag{3.111}$$

where again, $[Q]$ is again a boolean matrix indicating where measurement points exist. The MECE objective functional can now be written as

$$\mathcal{J}_{MECE}(\{u\}, \underline{d}, \{I\}, \underline{p}) = \mathcal{U}(\{u\}, \underline{d}, \{I\}, \underline{p}) + \kappa\mathcal{M}(\{u\}). \tag{3.112}$$

In an attempt to determine the parameters $\underline{p}$ that will yield a solution corresponding to the measurements, we seek to minimize J_{MECE}. The parameter κ is a penalty parameter proportional to how strongly the measurements are enforced. Specifically, it allows us to balance the error in the internal force computation and how closely we want the displacement field to match the measurements. As there may be error in the measurements, we do not want to enforce such measurements strongly. The parameter κ allows us to enforce the measurements in a way that is commensurate with the noise level. We will discuss how κ is selected further in section 3.3.3. We again enforce the forward problem through a constraint. The

Lagrangian becomes,

$$\mathcal{L}_{MECE}(\{I\},\{u\},\{v\},\{a\},\underline{d},\{\bar{u}\},\{\bar{v}\},\{\bar{a}\},\underline{\bar{d}},\underline{p}) =$$
$$\mathcal{J}_{MECE}(\{u\},\underline{d},\{I\},\underline{p}) + \mathcal{C}_{MECE}(\{I\},\{u\},\{v\},\{a\},\underline{d},\{\bar{u}\},\{\bar{v}\},\{\bar{a}\},\underline{\bar{d}},\underline{p}) \quad (3.113)$$

In the previous section when we considered only the least squares functional, we substituted the internal force evaluation for the internal force vector directly. In this case, we have enforced this relationship weakly through $\mathcal{U}$, and therefore the constraint equations are in terms of $\{I\}_k$ instead of $I(\{u\}_k, \underline{d}_k, \underline{p})$.

$$\begin{aligned}
\mathcal{C}_{MECE}(\{I\},\{u\},\{v\},\{a\},\underline{d},\{\bar{u}\},\{\bar{v}\},\{\bar{a}\},\underline{\bar{d}},\underline{p}) = \\
+ \{\bar{u}\}_0^T \left[[M]\{a\}_0 + [C]\{v\}_0 + \{I\}_0 - \{F\}_0\right] \\
+ \sum_{k=0}^{N-1} \{\bar{u}\}_{k+1}^T \left[[M]\{a\}_{k+1} + [C]\{v\}_{k+1} + \{I\}_{k+1} - \{F\}_{k+1}\right] \\
+ \{\bar{v}\}_{k+1}^T [M] \left(\{v\}_{k+1} - \{v\}_k - \Delta t[(1-\gamma)\{a\}_k + \gamma\{a\}_{k+1}]\right) \\
+ \{\bar{a}\}_{k+1}^T [M] \left(\{u\}_{k+1} - \{u\}_k - \Delta t\{v\}_k - \frac{\Delta t^2}{2}[(1-2\beta)\{a\}_k + 2\beta\{a\}_{k+1}]\right) \\
+ \underline{\bar{d}}_{k+1}^T \left(\underline{d}_{k+1} - E(\{u\}_{k+1}, \underline{d}_k, \underline{p})\right). \quad (3.114)
\end{aligned}$$

We do, however, enforce the state variable evolution equation strongly through a constraint equation similar to the least squares case. Uncertain quantities are postulated as part of the objective functional, *i.e.* through $\mathcal{U}$ and $\mathcal{M}$. Quantities that are not uncertain are enforced in the constraints. We are allowing errors to persist in the way we connect the internal force to the displacement and state variables. Since we have accounted for this potential error, allowing more error to persist in the evolution of the hidden state variables would be potentially redundant and cumbersome. We are not allowing errors to persist in how the state variables evolve.

In order to find the critical points of the Lagrangian, we need to satisfy the

optimality conditions. Specifically the variations of $\mathcal{L}_{MECE}$ need to equal zero for all directions. We proceed in an iterative alternating direction fashion. Specifically we fix the parameters, $\underline{p}$, and satisfy all of the other optimality conditions. We begin by taking the variation with respect to the internal force vector. This yields,

$$D\mathcal{L}_{MECE} \cdot \{\delta I\}_k = \left(\{I\}_k - I(\{u\}_k, \underline{d}_k, \underline{p})\right)^T [K_T^0]^{-1}\{\delta I\}_k + \{\bar{u}\}_k^T.\{\delta I\}_k \quad (3.115)$$

Satisfying the condition,

$$D\mathcal{L}_{MECE} \cdot \{\delta I\} = 0, \ \forall\{\delta I\}. \quad (3.116)$$

we get a modified internal force calculation,

$$\{I\}_k = I(\{u\}_k, \underline{d}_k, \underline{p}) - [K_T^0]\{\bar{u}\}_k, \quad (3.117)$$

Again, if $I(\{u\}_k, \underline{d}_k, \underline{p})$ arose exclusively as a result of linear elasticity, we could write this as

$$\{I\}_k = [K]\left(\{u\}_k - \{\bar{u}\}_k\right). \quad (3.118)$$

Rather than obtaining a modified constitutive relation, we get a modified internal force computation. This is a direct consequence of the fact that $\mathcal{U}$ is in terms of the internal force error as opposed to the constitutive relation error. We now proceed to take the variations of the Lagrangian with respect to the adjoint variables, and set them equal to zero. Taking the variation with respect to $\{\bar{u}\}$, and setting it equal to zero for all directions,

$$D\mathcal{L}_{MECE} \cdot \{\delta\bar{u}\} = 0, \ \forall\{\delta\bar{u}\}, \quad (3.119)$$

we get,

$$[M]\{a\}_k + [C]\{v\}_k + \{I\}_k = \{F\}_k. \quad (3.120)$$

We can enforce the modified internal force computation, and substitute (3.117) into (3.120), yielding

$$[M]\{a\}_k + [C]\{v\}_k + I(\{u\}_k, \underline{d}_k, \underline{p}) = \{F\}_k + [K_T^0]\{\bar{u}\}_k. \tag{3.121}$$

Observe that the modified internal force computation brings the adjoint variable, $\{\bar{u}\}_k$, into the governing equations for the forward displacement field. As in the least squares case, if we take the variations with respect to $\{\bar{v}\}$, $\{\bar{a}\}$, and $\underline{\bar{d}}$, we recover the Newmark Beta equations and the state variable evolution equations. Thus we have to modify our forward solution algorithm to add $[K_T^0]\{\bar{u}\}_k$ to the external force vector at each time step. Specifically (3.29) becomes

$$[M]\{a\}_0 \;=\; \{F\}_0 + [K_T^0]\{\bar{u}\}_0 \tag{3.122}$$

and (3.32) becomes,

$$\left(\frac{1}{\beta\Delta t^2}[M] + \frac{\gamma}{\beta\Delta t}[C]\right)\boldsymbol{u}_{k+1} + I(\{u\}_k, \underline{d}_k, \underline{p}) = \{F\}_{k+1} + [K_T^0]\{\bar{u}\}_k - [C]\{\eta\}_k + [M]\{\xi\}_k. \tag{3.123}$$

Moreover, we can express the modified forward problem as

$$\mathbb{N}_F\{u\} = \mathbb{F} + \mathbb{K}\{\bar{u}\} \tag{3.124}$$

where $\mathbb{K}$ is a space-time block matrix, with $[K_T^0]$ tiled along the diagonal. Equation (3.124) parallels equation (3.33) except the right hand side is coupled to the adjoint variable, $\{\bar{u}\}$, through the term $\mathbb{K}\{\bar{u}\}$. We now can focus on the variations with respect to the forward variables. First we take the variation with respect to displacement,

$$\begin{aligned} D\mathcal{L}_{MECE}\cdot\{\delta u\}_k = \big([M](\{\bar{a}\}_k - \{\bar{a}\}_{k+1}) \\ -[K_T^k][K_T^0]^{-1}\left(\{I\}_k - I(\{u\}_k, \underline{d}_k, \underline{p})\right) \\ + \kappa[Q](\{u\}_k - \{u^M\}_k) - \left[\frac{\partial E(\{u\}_k, \underline{d}_{k-1}, \underline{p})}{\partial\{u\}_k}\right]^T \underline{\bar{d}}_k\Bigg)^T \{\delta u\}_k. \end{aligned} \tag{3.125}$$

for all but the final time step, and

$$D\mathcal{L}_{MECE}\cdot\{\delta u\}_N = ([M]\{\bar{a}\}_N \\ -[K_T^N][K_T^0]^{-1}\left(\{I\}_N - I(\{u\}_N,\underline{d}_N,\underline{p})\right) \\ + \kappa[Q](\{u\}_N - \{u^M\}_N) - \left[\frac{\partial E(\{u\}_N,\underline{d}_{N-1},\underline{p})}{\partial\{u\}_N}\right]^T \underline{\bar{d}}_N\Bigg)^T \{\delta u\}_N. \quad (3.126)$$

for the final time step. Upon substitution of the modified internal force computation, (3.117), into (3.125) and (3.126), we almost recover (3.67) and (3.68) respectively. The only distinction is, in this case, $[Q]$ is scaled by κ. That is for all but the last time step,

$$D\mathcal{L}_{MECE}\cdot\{\delta u\}_k = \left([M](\{\bar{a}\}_k - \{\bar{a}\}_{k+1}) + [K_T^k]^T\{\bar{u}\}_k \right. \\ \left. + \kappa[Q](\{u\}_k - \{u^M\}_k) - \left[\frac{\partial E(\{u\}_k,\underline{d}_{k-1},\underline{p})}{\partial\{u\}_k}\right]^T \underline{\bar{d}}_k\right)^T \{\delta u\}_k \quad (3.127)$$

and for the final time step,

$$D\mathcal{L}_{MECE}\cdot\{\delta u\}_N = \left([M]\{\bar{a}\}_N + [K_T^N]^T\{\bar{u}\}_N \right. \\ \left. + \kappa[Q](\{u\}_N - \{u^M\}_N) - \left[\frac{\partial E(\{u\}_N,\underline{d}_{N-1},\underline{p})}{\partial\{u\}_N}\right]^T \underline{\bar{d}}_N\right)^T \{\delta u\}_N. \quad (3.128)$$

It is clear that when we consider the variations with respect to $\{v\}$, we recover (3.70) and (3.71),

$$D\mathcal{L}_{MECE}\cdot\{\delta v\}_k = D\mathcal{L}_{LS}\cdot\{\delta v\}_k \quad (3.129)$$

$$D\mathcal{L}_{MECE}\cdot\{\delta v\}_N = D\mathcal{L}_{LS}\cdot\{\delta v\}_N. \quad (3.130)$$

Moreover, considering the variation with respect to $\{a\}$, we recover (3.72)-(3.74) and can conclude,

$$D\mathcal{L}_{MECE}\cdot\{\delta a\}_0 = D\mathcal{L}_{LS}\cdot\{\delta a\}_0 \quad (3.131)$$

$$D\mathcal{L}_{MECE}\cdot\{\delta a\}_k = D\mathcal{L}_{LS}\cdot\{\delta a\}_k \quad (3.132)$$

$$D\mathcal{L}_{MECE}\cdot\{\delta a\}_N = D\mathcal{L}_{LS}\cdot\{\delta a\}_N. \quad (3.133)$$

Finally considering $\underline{d}$, we get

$$D\mathcal{L}_{MECE}\cdot\delta\underline{d}=\left(-\left[\frac{\partial I(\{u\}_k,\underline{d}_k,\underline{p})}{\partial\underline{d}_k}\right]^T[K_T^0]^{-1}\left(\{I\}_k-I(\{u\}_k,\underline{d}_k,\underline{p})\right)\right.$$
$$\left.+\bar{\underline{d}}_k-\left[\frac{\partial E(\{u\}_{k+1},\underline{d}_k,\underline{p})}{\partial\underline{d}_k}\right]\bar{\underline{d}}_{k+1}\right)^T\delta\underline{d}_k \quad (3.134)$$

for all but the final time step, and

$$D\mathcal{L}_{MECE}\cdot\delta\underline{d}=$$
$$\left(-\left[\frac{\partial I(\{u\}_k,\underline{d}_k,\underline{p})}{\partial\underline{d}_k}\right]^T[K_T^0]^{-1}\left(\{I\}_k-I(\{u\}_k,\underline{d}_k,\underline{p})\right)+\bar{\underline{d}}_k\right)^T\delta\underline{d}_k \quad (3.135)$$

for the final time step. Upon substituting (3.117) into (3.134) and (3.135), we can recover (3.75) and (3.76) respectively. Specifically,

$$D\mathcal{L}_{MECE}\cdot\underline{d}_k = D\mathcal{L}_{LS}\cdot\underline{d}_k \quad (3.136)$$

$$D\mathcal{L}_{MECE}\cdot\underline{d}_N = D\mathcal{L}_{LS}\cdot\underline{d}_N. \quad (3.137)$$

Thus the variations of $\mathcal{L}_{MECE}$ with respect to the forward variables yield the same equations as the variations of $\mathcal{L}_{LS}$ with respect to the forward variables, with the exception of scaling the boolean measurement matrix $[Q]$ by κ. Setting these variations to zero results in the same adjoint solution algorithm outlined in the previous section with one small modification, resulting from κ. Specifically equations (3.86) and (3.87) become,

$$\left(\frac{1}{\beta\Delta t^2}[M]+\frac{\gamma}{\beta\Delta t}[C]+[K_T^N]^T+\right.$$
$$\left.\left[\frac{\partial E(\{u\}_N,\underline{d}_{N-1},\underline{p})}{\partial\underline{u}_N}\right]^T\left[\frac{\partial I(\{u\}_N,\underline{d}_N,\underline{p})}{\partial\underline{d}_N}\right]^T\right)\{\bar{u}\}_N=\kappa[Q](\{u^M\}_N-\{u\}_N) \quad (3.138)$$

and,

$$\left(\frac{1}{\beta\Delta t^2}[M]+\frac{\gamma}{\beta\Delta t}[C]+[K_T^K]^T+\right.$$
$$\left.\left[\frac{\partial E(\{u\}_k,\underline{d}_{k-1},\underline{p})}{\partial \underline{u}_k}\right]^T\left[\frac{\partial I(\{u\}_k,\underline{d}_k,\underline{p})}{\partial \underline{d}_k}\right]^T\right)\{\bar{u}\}_k=$$
$$[M]\left(\frac{2\gamma+1}{2\beta}\{\bar{a}\}_{k+1}+\frac{1}{\beta\Delta t}\{\bar{v}\}_{k+1}\right)+\kappa[Q](\{u^M\}_k-\{u\}_k)$$
$$+\left[\frac{\partial E(\{u\}_k,\underline{d}_{k-1},\underline{p})}{\partial\{u\}_k}\right]^T\left[\frac{\partial E(\{u\}_{k+1},\underline{d}_k,\underline{p})}{\partial \underline{d}_k}\right]^T\bar{\underline{d}}_{k+1} \quad (3.139)$$

respectively. Moreover, we can write the adjoint problem as,

$$\mathbb{N}_A\{\bar{u}\}=\kappa\mathbb{Q}\left(\{u^M\}-\{u\}\right). \quad (3.140)$$

If we compare this to (3.106), we see that the left hand side operator is the same, and the right hand side has a been scaled by κ.

In contrast to the coupled system found in the least squares approach, (3.107), the coupled system resulting from the MECE approach is bi-directionally coupled through $\mathbb{K}$,

$$\begin{bmatrix}\mathbb{N}_F & -\mathbb{K}\\ \kappa\mathbb{Q} & \mathbb{N}_A\end{bmatrix}\begin{Bmatrix}\{u\}\\ \{\bar{u}\}\end{Bmatrix}=\begin{Bmatrix}\mathbb{F}\\ \kappa\mathbb{Q}\{u^M\}\end{Bmatrix}. \quad (3.141)$$

We can no longer solve the coupled system sequentially as in the least squares case. In order to solve the nonlinear space-time coupled system, we appeal to SOR-Newton, which is a common technique for solving nonlinear algebraic equations [91], [42]. We do not discuss the details of the Newton iteration here. Specifically, $\mathbb{N}_F$ can be nonlinear, but we assume we can invert this operator up to a sufficient tolerance using Newton or quasi-Newton iterations. The SOR-Newton iteration

scheme becomes

$$\begin{bmatrix} \mathbb{N}_F & 0 \\ \omega\kappa\mathbb{Q} & \mathbb{N}_A \end{bmatrix} \begin{Bmatrix} \{u\}^{i+1} \\ \{\bar{u}\}^{i+1} \end{Bmatrix} = \begin{bmatrix} (1-\omega)\mathbb{N}_F & \omega\mathbb{K} \\ 0 & (1-\omega)\mathbb{N}_A \end{bmatrix} \begin{Bmatrix} \{u\}^{i} \\ \{\bar{u}\}^{i} \end{Bmatrix} + \begin{Bmatrix} \omega\mathbb{F} \\ \omega\kappa\mathbb{Q}\{u^M\} \end{Bmatrix} \quad (3.142)$$

where variables with only superscripts denote the space-time representation of SOR iterates. Specifically, we sequentially solve,

$$\mathbb{N}_F\{u\}^{i+1} = (1-\omega)\mathbb{N}_F\{u\}^{i} + \omega\mathbb{K}\{\bar{u}\}^{i} + \omega\mathbb{F} \quad (3.143)$$

$$\mathbb{N}_A\{\bar{u}\}^{i+1} = (1-\omega)\mathbb{N}_A\{\bar{u}\}^{i} + \omega\kappa\mathbb{Q}\left(\{u^M\} - \{u\}^{i+1}\right). \quad (3.144)$$

As equation (3.143) has $\mathbb{N}_F$ on the left hand side, this equation may require Newton or quasi-Newton iterations to solve. This detail is suppressed, and we merely assume that we can obtain $\{u\}^{i+1}$. In the linear case, we can reformulate (3.143)-(3.144) in terms of $(\{u\}^{i+1} - \{u\}^{i})$ and $(\{\bar{u}\}^{i+1} - \{\bar{u}\}^{i})$ respectively. In other words, we can solve for the incremental change at each iterate, and eliminate the dependance of the right hand side of (3.143) on the previous iteration. In the nonlinear case, this is not possible. We require the previous solution in the term $(1-\omega)\mathbb{N}_F\{u\}^{i}$. Rather than merely store the previous iterate solution, $\{u\}^{i}$, and compute the forward operator times $\{u\}^{i}$, *i.e.* $\mathbb{N}_F\{u\}^{i}$, we store the entire right hand side for the previous iterate, which is exactly equal to this quantity. Specifically we have computed at the previous SOR iteration,

$$\mathbb{N}_F\{u\}^{i} = (1-\omega)\mathbb{N}_F\{u\}^{i-1} + \omega\mathbb{K}\{\bar{u}\}^{i-1} + \omega\mathbb{F}. \quad (3.145)$$

Rather than recompute the left hand side of (3.145) for the $(i+1)^{th}$ SOR iterate computation, we store the right hand side of (3.145), and substitute this stored quantity into (3.143). By doing this, we eliminate the need to compute $\mathbb{N}_F$ acting

on $\{u\}^i$. Similarly, we store

$$\mathbb{N}_A\{\bar{u}\}^i \;=\; (1-\omega)\mathbb{N}_A\{\bar{u}\}^{i-1} + \omega\kappa\mathbb{Q}\left(\{u^M\} - \{u\}^i\right) \tag{3.146}$$

for the right hand side of (3.144).

We measure the SOR-Newton convergence by,

$$e_{i+1} = \frac{||\{u\}^{i+1} - \{u\}^i||^2 + ||\{\bar{u}\}^{i+1} - \{\bar{u}\}^i||^2}{||\{u\}^i||^2 + ||\{\bar{u}\}^i||^2}. \tag{3.147}$$

We note that

$$\sqrt{||\{u\}||^2 + ||\{\bar{u}\}||^2} \tag{3.148}$$

is in fact a norm. The error measure in equation (3.147) is merely the norm squared relative difference in the solutions for subsequent iterates. Specifically, convergence in this norm indicates that we have found a fixed point, and presumably the solution, of (3.142). The adjoint solution is driven by the measurement error. Thus, as the error between the forward solution and the measurements decrease, the adjoint solution magnitude decreases and we ultimately recover the unmodified internal force evaluation. Specifically, as $\{\bar{u}\}$ decays, so does $[K_T^0]\{\bar{u}\}$, and as this shrinks to zero, we recover (3.51). In practice we find that we usually need to under-relax the coupled solve iterations, *i.e.* pick $\omega < 1$, for the scheme to converge. Recall that we had assumed the material parameters were fixed, and subsequently satisfied the remaining optimality conditions, specifically by solving the coupled system (3.141). After the coupled solver has converged to a specified tolerance, we can move on to the material parameter update step.

Parameter Update

For the parameter update step we fix all of the arguments in (3.114) except $\underline{p}$, and subsequently satisfy the optimality conditions treating only $\underline{p}$ as varying. In the linear elastic case, analogous to [8], we can find the updated parameters analytically by satisfying

$$D\mathcal{L}_{MECE} \cdot \delta\underline{p} = 0, \ \forall \delta\underline{p}. \tag{3.149}$$

In the nonlinear case, we cannot find $\underline{p}$ to satisfy (3.149) exactly. In this case, we postulate a smaller optimization problem for each element with unknown parameters to find $\underline{p}$ given fixed forward and adjoint fields, $\{u\}$ and $\{\bar{u}\}$. Specifically, we minimize

$$\mathcal{J}_p^e(\underline{p}) = \frac{C}{2} \sum_{k=1}^{N} \left|\left| \{I\}_k^e - I^e(\{u\}_k^e, \underline{d}_k^e, \underline{p}) \right|\right|^2 \tag{3.150}$$

where the superscript e denotes element level quantities and C is a normalizing constant, chosen to scale $\mathcal{J}_p^e$ appropriately. We choose,

$$C = \left(\sum_{k=1}^{N} ||\{I\}_k^e||^2 \right)^{-1}. \tag{3.151}$$

Notice that $\{I\}_k^e$ is given by the element level analog of (3.117),

$$\{I\}_k^e = I^e(\{u\}_k^e, \underline{d}^e, \underline{p}) - [K_T^0]^e \{u\}_k^e. \tag{3.152}$$

This minimization problem requires no PDE solves, and is computationally insignificant when compared to the coupled forward and adjoint solution. Specifically, for each parameter $p_i \in \underline{p}$, we can compute

$$\frac{\partial \mathcal{J}_p^e}{\partial p_i} = C \sum_{K=1}^{N} \left(\{I\}_k^e - I^e(\{u\}_k^e, \underline{d}_k^e, \underline{p}) \right)^T \left(\frac{\partial I^e(\{u\}_k^e, \underline{d}^e, \underline{p})}{\partial p_i} \right). \tag{3.153}$$

The gradient computation for the parameter update sub-problem can even be done with finite differences. Specifically we can approximate

$$\left(\frac{\partial I^e(\{u\}_k^e, \underline{d}^e, \underline{p})}{\partial p_i}\right) \tag{3.154}$$

with finite differences inexpensively with element level computations.

Once we compute the objective function and the gradient, we can use any standard gradient based iterative optimization technique. We used a trust region Limited Memory Broyden-Fletcher-Goldfarb-Shanno (L-BFGS) algorithm [26], [92]. At this point in the global scheme it is important to consider constraints on the material parameters. The BFGS implementation handles bound constraints, and we enforce our material bounds at this level. Since the parameter update is a local computation done at an element level, we can have various constitutive models in a single structural model, each with their own parameter update scheme. For example, we can update elastic elements with a closed form update, and perform small optimizations for nonlinear elements.

It is important to have some a priori knowledge of material parameter bounds. In the implementation of the parameter update, we use each parameter's largest bound as a normalizing factor. Specifically, if a particular parameter, $p_i \in \underline{p}$ has a largest potential value of p_i^L, we consider,

$$\widetilde{p_i} = \frac{p_i}{p_i^L}. \tag{3.155}$$

Observe that $|\widetilde{p_i}| < 1$. Now we can reformulate the objective function in terms of $\widetilde{p_i}$,

$$\widetilde{\mathcal{J}}(\widetilde{p_i}) = \mathcal{J}(\widetilde{p_i} p_i^L). \tag{3.156}$$

Moreover the objective function derivative with respect to $\widetilde{p_1}$ becomes,

$$\frac{\partial \widetilde{\mathcal{J}}}{\partial \widetilde{p_i}} = \frac{\partial \mathcal{J}}{\partial p_i} \cdot p_i^L. \tag{3.157}$$

This ensures that parameter space is scaled relatively uniformly over all the parameters to be identified.

While the optimization is insensitive to some bounds, others have shown to significantly impact the reconstruction. Specifically, a good bound for the yield point should be input if possible. For the Iwan model, this parameter is denoted F_S. If in the experiment to generate the measurements, no yielding is observed, we should attempt to set the minimum yield point of the material above the maximum force experienced by the material. While this is not always possible, we can diagnose a bad yield point bound by observing the algorithm's behavior. If, through the course of the optimization routine a parameter set is obtained at the parameter update step such that the material yield point is below the maximum force experienced, we will see the material yield in the subsequent forward solve. This in turn will make $\{u\} - \{u^M\}$ large and the adjoint field solution large. Finally, this will result in a large jump in both the ECE error and Least Squares error discussed in Section 3.3.4, equations (3.168) and (3.170) respectively.

3.3.3 Regularization and the penalty parameter

As part of the MECE optimization scheme, we not only identify the material parameters, but also the corresponding displacement field $\boldsymbol{u}$. In the MECE objective functional we have two separate terms. First is the error in constitutive equation functional, and second is the least squares measurement error functional. We can understand the least squares portion of the objective functional as a regularizer for the displacement field. Rather than impose measurements strongly, or directly as one would Dirichlet conditions, we enforce them in a weak sense through the least squares functional. As we increase the penalty parameter κ, we force the optimized

displacement field to better match the measurements. This weak enforcement prevents over fitting to the measurement data. As we let κ tend to infinity, we recover the strong, or Dirichlet, enforcement of measurement points. If the measurements do in fact contain noise, we would not want to force the displacement field match them exactly. Thus we need to consider the potential noise level in selecting κ. In [71] we see general guidelines for selecting the regularization parameter. Specifically, we seek a regularization parameter that yields a solution where the final error in the measurements is approximately equal to the noise level. Specifically, if we assume that $\boldsymbol{u}^M$ is a noisy measurement of the true, unpolluted, signal, *i.e.* $\boldsymbol{u}^{True}$, then Morozov's principle says we should choose our regularization parameter such that

$$\left|\left|\boldsymbol{u}^M - \boldsymbol{u}^*\right|\right| \approx \left|\left|\boldsymbol{u}^M - \boldsymbol{u}^{True}\right|\right| \tag{3.158}$$

where $\boldsymbol{u}^*$ is the final displacement field resulting from the MECE optimization algorithm. That is the error between the solution field and the measurements should be approximately the same order of the noise level. To the point of not over-emphasizing the measurement error, we seek to balance the two terms in the objective functional. We draw inspiration from the linear elastic case where the ECE functional reduces to,

$$\mathcal{U}_{Elastic} = \frac{1}{2}\sum_{k=1}^{N}\left(\{I\}_k - [K]\{u\}_k\right)^T [K]^{-1}\left(\{I\}_k - [K]\{u\}_k\right), \tag{3.159}$$

where $[K]$ is the stiffness matrix. We observe in this case $(\{I\}_k - [K]\{u\}_k)$ has the same units as the internal force vector and indeed can be interpreted as the internal force resulting from the error in the material parameters. We denote this error as,

$$\{I\}_k^\ell = \left(\{I\}_k - [K]\{u\}_k\right). \tag{3.160}$$

Moreover, we can quantify the equivalent displacement that would correspond to $\{I\}_k^\ell$ as,

$$\{u\}_k^\ell = [K]^{-1}\{I\}_k^\ell. \tag{3.161}$$

Now we can write

$$\mathcal{U}_{Elastic} \;=\; \frac{1}{2}\sum_{k=1}^{N}\left(\{u\}_k^\ell\right)^T[K]\left(\{u\}_k^\ell\right) \tag{3.162}$$

Elastic strain energy can be computed, after discretization, by,

$$\xi = \{u\}_k^T[K]\{u\}_k. \tag{3.163}$$

Thus in the elastic case, we can think of the ECE functional as the sum over time steps of the strain energy of the error. In an attempt to give similar weight to the components of the MECE functional, we give κ the following form,

$$\kappa = \beta_p \sum_{k=1}^{N} \frac{\{u^M\}_k^T[A]^{-1}\{u^M\}_k}{\{u^M\}_k^T\{u^M\}_k}. \tag{3.164}$$

In (3.164) we use $\{u^M\}$ as it likely provides at least the same order of magnitude as $\{u\}^\ell$. In the elastic case (where $[A]^{-1} = [K]$) we are scaling $\frac{\kappa}{2}\mathcal{M}(\{u\})$ to have a magnitude on the order of the sum of the strain energy over time steps, similar to the ECE portion of the functional. With this normalization, β_p takes values that are $O(1)$, *i.e.* independent of other numerical parameters. Actual selection of β_p is dependent on measurement noise and accuracy of initial conditions. In instances when $\{u^M\}$ consists of sparse measurements, entries not corresponding to measurement points are set to zero.

We now consider what this means in the nonlinear case. We focus on the nonlinear case where the tangent stiffness decreases as displacement increases. This is the case for the Iwan model. We again consider the quantity,

$$\left(\{I\}_k - I(\{u\}_k, \underline{d}_k, \underline{p})\right)[K_T^0]\left(\{I\}_k - I(\{u\}_k, \underline{d}_k, \underline{p})\right), \tag{3.165}$$

We denote the quantity,

$$\{I\}_k^n = \{I_k\} - I(\{u\}_k, \underline{d}_k, \underline{p}). \tag{3.166}$$

In the elastic case, we could relate $\{I\}_k^\ell$ to $\{u\}_k^\ell$ in a linear way through (3.161). This is not the case when $I(\{u\}_k, \underline{d}_k, \underline{p})$ is nonlinear. For example, in the nonlinear case, if we assume that $\{u\}_{k,1}$ and $\{u\}_{k,2}$ are in the same direction,

$$I(\{u\}_{k,1} + \{u\}_{k,2}, \cdot) - I(\{u\}_{k,1}, \cdot) < I(\{u\}_{k,2}, \cdot). \tag{3.167}$$

Note we have suppressed the state variable $\underline{d}_k$ for the sake of clarity and assume it can be inferred by displacement. If we were to try and connect $\{I\}_k^n$ to a corresponding displacement $\{u\}_k^n$ using equation (3.161) as in the elastic case, we would get a larger estimate $\{u\}_k^n$ than is in fact true. Given this observation, we can imagine that $\{u\}_k - \{u^M\}_k$ might be large, but in fact $\{I\}_k^n$ might be much smaller as the internal force response for $\{u\}_k$ and $\{u^M\}_k$ might be close. Physically this might be true near a material yielding point. Thus when we give κ the form (3.164) in the nonlinear case we would conjecture that β_p would take much smaller values. This is in fact what we find. Given this normalization, we find that β_p is still $O(1)$, but it needs to be smaller than what we would choose in the purely elastic case in order to balance the least squares measurement error and the ECE error.

While we have not directly analyzed the connection between the penalty parameter, κ, and regularization of the identified material parameters, we have observed numerically that κ, and more specifically β_p, can be used to bring stability to the numerical computation. The number of Iwan elements is generally small compared to the number of elements in the ambient structure. For this reason, the array of Iwan parameters to identify is generally low dimensional. Moreover, in the experiments we have performed, we have seen high observability of the material response

and hence the material parameter set. Should this formulation be extended to other specific nonlinear material models with higher dimensional parameter sets to identify, we would need to further examine the role of κ as a regularizer. Specifically, we would need to better understand how κ influences the regularity of high dimensional, spatially varying parameter sets. We know that as κ tends to infinity, we recover an Error in Constitutive Equation type of scheme. The weak enforcement of measurements allows the displacement field to be more regular, *i.e.* the forward displacement field does not need to exactly match the measurements. The increased regularity of the displacement field seems to impart increased regularity on the corresponding material parameters.

3.3.4 Stopping criteria

We initialize the algorithm, *i.e.* select β_p, such that the least squares measurement error and the ECE error are approximately equal on the first iteration. In practice we compare the normalized least squares measurement error

$$E_{LS} = \frac{\sum_{k=1}^{N} \left|\left|\{u\}_k - \{u^M\}_k\right|\right|^2}{\sum_{k=1}^{N} \left|\left|\{u^M\}_k\right|\right|^2} \tag{3.168}$$

and the normalized ECE error

$$E_{ECE} = \frac{\sum_{k=1}^{N} \left|\left|[K_T^0]\{\bar{u}\}_k\right|\right|^2}{\sum_{k=1}^{N} \left|\left|\{I\}_k\right|\right|^2} \tag{3.169}$$

$$= \frac{\sum_{k=1}^{N} \left|\left|[K_T^0]\{\bar{u}\}_k\right|\right|^2}{\sum_{k=1}^{N} \left(\left|\left|I(\{u\}_k, \underline{d}_k, \underline{p}) - [K_T^0]\{\bar{u}\}_k\right)\right|\right|^2}. \tag{3.170}$$

Observe that since the tangent stiffness matrix, $[K_T^0]$, is symmetric positive definite, the inverse of the tangent stiffness matrix $[K_T^0]$ is also symmetric positive definite.

Thus, we can bound the ECE error as,

$$\frac{1}{2}\sum_{k=1}^{N}\left(\{I\}_k - I(\{u\}_k, \underline{d}_k; \underline{p})\right)^T [K_T^0]^{-1}\left(\{I\}_k - I(\{u\}_k, \underline{d}_k; \underline{p})\right) \leq \\ \frac{\alpha}{2}\sum_{k=1}^{N}\left(\{I\}_k - I(\{u\}_k, \underline{d}_k; \underline{p})\right)^T [I]\left(\{I\}_k - I(\{u\}_k, \underline{d}_k; \underline{p})\right) \quad (3.171)$$

where α is a sufficiently large constant and $[I]$ is the identity matrix. Substituting in the modified constitutive equation, (3.117), into the right hand side of (3.171) we conclude,

$$\frac{1}{2}\sum_{k=1}^{N}\left(\{I\}_k - I(\{u\}_k, \underline{d}_k; \underline{p})\right)^T [K_T^0]^{-1}\left(\{I\}_k - I(\{u\}_k, \underline{d}_k; \underline{p})\right) \leq \\ \frac{\alpha}{2}\sum_{k=1}^{N}\left([K_T^0]\{\bar{u}\}_k\right)^T [I]\left([K_T^0]\{\bar{u}\}_k\right). \quad (3.172)$$

Notice that we can rewrite the right hand side of (3.172) in terms of the Euclidian norm,

$$\frac{1}{2}\sum_{k=1}^{N}\left(\{I\}_k - I(\{u\}_k, \underline{d}_k; \underline{p})\right)^T [K_T^0]^{-1}\left(\{I\}_k - I(\{u\}_k, \underline{d}_k; \underline{p})\right) \leq \\ \frac{\alpha}{2}\sum_{k=1}^{N}\left|\left|[K_T^0]\{\bar{u}\}_k\right|\right|^2. \quad (3.173)$$

We normalize (3.173) by the norm of the internal force vector summed over time steps in order to arrive at E_{ECE} as defined in (3.170). We can view E_{ECE} as the proportion of the internal force vector that results from the adjoint correction factor in the modified internal force calculation (3.117). As we drive E_{ECE} to zero, we are driving the ECE functional $\mathcal{U}(\cdot)$ to zero as well. Normalizing the ECE functional and the least squares measurement error functional makes the initial errors more problem independent. This allows us to more easily balance the initial errors as described in section 3.3.3.

In the case where some element blocks are in fact known, and thus we are not

changing parameters in these element blocks, we modify (3.170) to only evaluate the error over the unknown element blocks. We denote the set of unknown blocks as $\{B\}_U$ and calculate,

$$E^B_{ECE} = \frac{\sum_{B\in\{B\}_U}\sum_{k=1}^{N}\left|\left|[K^0_T]^B\{\bar{u}\}^B_k\right|\right|^2}{\sum_{B\in\{B\}_U}\sum_{k=1}^{N}\left|\left|\{I\}^B_k\right|\right|^2} \tag{3.174}$$

where the superscript B denotes the block level assembled quantity as opposed to the global quantity. We monitor this error instead of the global quantity as it allows us to focus on the error specifically in the unknown blocks, which is where our concern lies. Moreover, since $\{\bar{u}\}$ is determined by the linear adjoint problem, (3.140), which is forced by $(\{u^M\} - \{u\})$, we have

$$\sum_{k=1}^{N}\left|\left|[K^0_T]\{\bar{u}\}_k\right|\right|^2 \leq \tilde{\alpha}\sum_{k=1}^{N}\left|\left|\{u^M\}_k - \{u\}_k\right|\right|^2 \tag{3.175}$$

where $\tilde{\alpha}$ is a sufficiently large constant. By driving E_{LS} to zero, we can be confident that we are also driving E_{ECE} to zero. Therefore by monitoring the global least squares error, E_{LS}, and the local internal force error, E^B_{ECE}, we can evaluate not only the global convergence of the algorithm, but the localized performance where material parameters are unknown.

While we strive to begin the algorithm with balanced errors, the errors do not remain balanced as the iterations progress. Moreover, we find that the hysteretic response in a specific Iwan element may not correspond to a unique parameter set. As a result, we often find in numerical experiments that we can drive both E^B_{ECE} and E_{LS} down several orders of magnitude, but at a point the algorithm stagnates. This is not unexpected, as there are likely local minima in the objective functional. When and where the algorithm stagnates appears to be a function of several factors such as initial conditions and parameter update optimization tolerance. To the second factor, we point out that we use much looser tolerances for the parameter update step, than for the global MECE scheme. The reason for

this is twofold. First, there is little benefit to fitting parameters with high accuracy to the forward and adjoint field when there is necessarily error in the forward and adjoint field due to the fact that they assumed a different fixed parameter set when they were obtained. Second, by using a looser tolerance we prevent the parameter set from being extremely different from iteration to iteration. This is important as the next SOR iteration is seeded with the previous solution as the initial guess. If the parameter set is vastly different the next SOR iteration may not converge. Ultimately, the stagnation would seem to indicate that the objective function surface is not convex. We find that the best results are found when we set a global tolerance above the stagnation point.

3.3.5 MECE Algorithm summary

Now we will briefly summarize the steps required for each MECE iteration. Iterations proceed until a suitable stopping criteria is met.

(1) Solve the MECE coupled problem, (3.141), for fixed parameter set and obtain $\{u\}$ and $\{\bar{u}\}$. This is done using the SOR-Newton iteration, outlined in (3.143)-(3.144).

(2) Update material parameters at element level. This can be done analytically if possible, or through a small optimization routine. If a small optimization routine is required, the parameter update objective functional and gradient are given by (3.150) and (3.153) respectively.

3.3.6 Implementation notes

In order to check our formulations, we initially implemented the forward and adjoint solvers for a single degree of freedom in MATLAB. We verified the adjoint formulation by using it to compute a gradient of the least squares measurement error cost functional, (3.54), with respect to the parameters. We compared the results using the adjoint solution and finite differences and once we obtained agreement to high accuracy, we were confident in the numerical formulation. From here we implemented the algorithm in Sierra/SD (formerly Salinas), a massively parallel structural finite element code developed by Sandia National Laboratories [13]. In Sierra/SD we implemented the adjoint solver and the SOR driver and other components to compute the gradient of the objective functional used in the parameter update step, (3.150). The necessary linear solves are performed in parallel using the underlying Generalized Dryja, Smith, and Widlund (GDSW) linear solver [33]. We implemented capability to optimize over the two different parameter sets for the Iwan model. We also provided the option to use one of two different optimization packages for the parameter update step. We can choose the Trilinos Rapid Optimization Library (ROL), [45] or the trust region L-BFGS algorithm [26], released by Argonne National Laboratory. At the time of implementation ROL did not have robust bound constraints, and thus we had better success with the L-BFGS package. Moreover, we found that using the physical parameter set for the material optimization allowed us to impose more intuitive bound constraints, specifically on the material yield point. The implementation allows the user to select the Newmark Beta parameters, yet for the numerical simulations we used $\beta = 0.25$ and $\gamma = 0.5$. Since the implementation utilizes the Sierra/SD infrastructure, it is expected to exhibit the same parallelism. We have tested this MECE implementation with up to 64 cores, and expect it to parallelize to the extent that

the Sierra/SD linear solvers do.

3.4 Numerical Examples

3.4.1 Single Degree of Freedom

In order to understand some of the more fundamental features of this algorithm we begin by studying a single degree of freedom problem. We postulate a single, 1-dimensional Iwan element in the x direction with the left endpoint fixed. We postulate a concentrated mass on the left endpoint of 80 kg. We discretize the Iwan model with $N = 51$ Jenkins elements and space them with a geometric progression parameter $\alpha = 1.2$. We apply a sinusoidal loading to the right node. Specifically, our loading function has the form

$$f(x) = (5 \times 10^5) \sin\left(\frac{2\pi t}{0.05}\right). \tag{3.176}$$

We use a time step of 1×10^{-3} and 50 time steps. During this period, the forcing function has undergone one full cycle. We generate measurements using the true parameter set

$$\begin{Bmatrix} R \\ S \\ \chi \\ \phi^{Max} \end{Bmatrix} = \begin{Bmatrix} 1 \times 10^{10} \\ 2 \times 10^9 \\ -0.8 \\ 4 \times 10^{-4} \end{Bmatrix}. \tag{3.177}$$

After obtaining the forward solution, we pollute the data with 5% Gaussian noise of the form

$$u_{i,k}^M = (1 + \alpha\eta) u_{i,k}^{True} \tag{3.178}$$

where η is a standard normal random variable and α is the noise level, 0.05 in our case. We use an initial guess of

$$\begin{Bmatrix} R \\ S \\ \chi \\ \phi^{Max} \end{Bmatrix} = \begin{Bmatrix} 1 \times 10^{11} \\ 2 \times 10^{9} \\ -0.8 \\ 4 \times 10^{-4} \end{Bmatrix} \tag{3.179}$$

While we generate measurements and initialize our algorithm with the $\{R, S, \chi, \phi^{Max}\}$ parameter set, we optimize over the more physical parameter set, $\{K_T, F_S, \chi, \beta_I\}$. Recall that we can convert to the physical parameter set using (3.39)-(3.41). Moreover, while we have only perturbed R from the true parameter set to generate the initial guess, all of the physical parameters in the initial conditions will be distinct from the parameters in the true set. We impose bounds in the physical parameter set as

$$\begin{Bmatrix} 5 \times 10^{8} \\ 1 \times 10^{6} \\ -0.9 \\ 0.01 \end{Bmatrix} \leq \begin{Bmatrix} K_T \\ F_S \\ \chi \\ \beta_I \end{Bmatrix} \leq \begin{Bmatrix} 1 \times 10^{11} \\ 1 \times 10^{7} \\ -0.1 \\ 5 \end{Bmatrix}. \tag{3.180}$$

Note that χ is constrained by the Iwan model to lie between -1 and 0, and β_I must be greater than 0. Observe the the maximum amplitude of the forcing function, (3.176), is 5×10^5, and we set the lower bound for F_S at 1×10^6. F_S is the force at which all the Jenkins element sliders within an Iwan element slip. This bound enforces the fact that there is no yielding in the simulation.

Convergence of coupled solver

Before we progress to analyzing the global convergence, we consider the coupled forward and adjoint solver. In order to make progress in an MECE iteration, we need to obtain both $\boldsymbol{u}$ and $\bar{\boldsymbol{u}}$ with sufficient accuracy. For the following SOR study, we use the the numerical setup described above with one exception: we do not pollute the measurements with Gaussian noise for this study.

Recall that we use SOR as a relaxation technique to solve the coupled forward and adjoint problem postulated in equation (3.141). This allows us to focus on implementing the individual forward and adjoint solvers. SOR Newton is a relaxation technique that has been used extensively for coupling multi physics problems. Our case differs in that time evolves in different directions for different equations. In the nonlinear case, the nonlinearity only appears in the $(1,1)$ block of the right hand side of (3.141). The equation corresponding to this block (the forward problem) is solved with a Newton loop at each time step. When we look at the transition equation for the adjoint problem, (3.87), we see that the right hand side does evolve in time but is in fact still linear with respect to the adjoint field. Solving the coupled forward and adjoint equation accurately is an essential component to the global MECE iterations. When prescribing a tolerance for the SOR-Newton convergence criteria, we need to consider the tolerance for the global MECE scheme. We need to solve the coupled problem to a tolerance that is more stringent than the global scheme. Otherwise errors in the forward and adjoint solution fields will pollute the parameter update.

In (3.142) we see that both the SOR parameter, ω, and the penalty parameter, κ, influence the right hand side. Whereas the penalty parameter κ only affects the adjoint problem, ω affects both the forward and the adjoint problem. We would anticipate that these parameters each affect the convergence behavior of the SOR

Newton loop in different ways. For this study we use the same single element model with sinusoidal forcing function, along with the same measurement data (although with no noise) and initial conditions (3.179). Since we give κ the form (3.164), we want to understand how the scheme behaves for different choices of β_p and ω. We study the SOR-Newton convergence for a given initial guess while varying ω and β_p.

We show the number of iterations required for convergence for different choices of β_p and ω in Figure 3.3. We observe that as β_p grows, we need to increase the relaxation, *i.e.* shrink ω in order to ensure convergence. This is expected as β_p specifically influences the magnitude of the lower diagonal block in the coupled system (3.141), and hence we need to increase the relaxation in order to ensure that the magnitude of the $\kappa[Q]$ term does not adversely affect the convergence. We also note here that for larger β_p the algorithm might not reach the specified tolerance in 100 iterations, or at all. For large β_p the SOR loop may stagnate at a residual higher than the prescribed tolerance.

For the process of actually obtaining reconstructed parameters, we set the coupled SOR solver tolerance at 1×10^{-6}, using $\beta_p = 0.02$ and $\omega = 0.1$. We also set the maximum number of SOR iterations at 10. At the parameter update step we use the trust region L-BFGS optimization package to perform the parameter update. For the parameter update step we set the gradient tolerance and the objective function tolerance at 10^{-2}. Recall we use a looser tolerance for the parameter update step for reasons discussed in section refstopcon. We find that the early MECE iterations tend to reach the maximum number of SOR iterations before converging to the tolerance. In fact, Figure 3.3 would seem to indicate that the SOR loop might not converge to this tolerance for this β_p, ω, and initial guess. We find that full convergence is not necessary for the early iterations. Even if the early

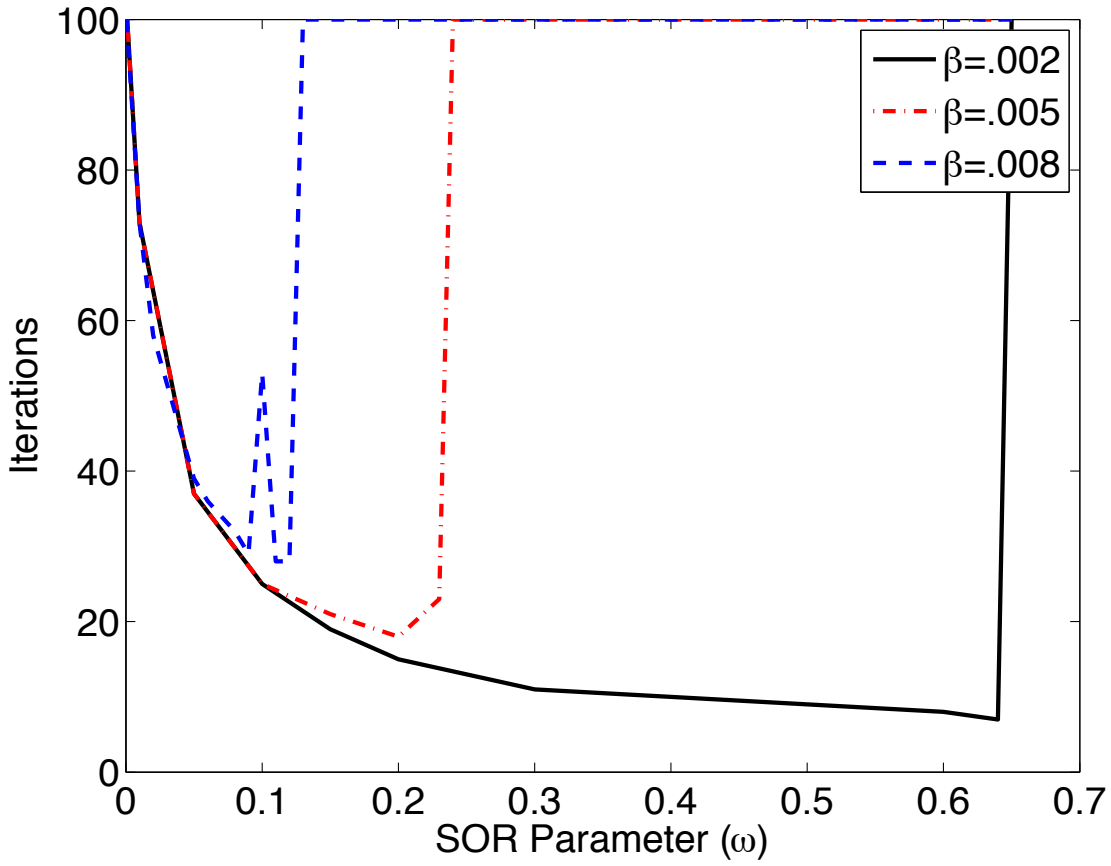

Figure 3.3: Number of SOR-Newton iterations required for different choices of β_p to reach a residual tolerance of $1e-4$. SOR parameter ω is plotted on the x axis, with number of iterations on the y axis. We allow a maximum number of 100 iterations.

MECE iterations have higher errors in the coupled solver, this is mitigated by the looser tolerance in the parameter update step. In other words, we do not need high accuracy in the forward and adjoint fields to get a sufficient initial parameter update. As long as there is sufficient accuracy to obtain a new parameter set that is "better" than the previous, we will attain higher accuracy and better parameters in subsequent iterations. We let the global iteration progress until E_{ECE} has stagnated. Towards this end, we solve to a global tolerance of 5×10^{-4} in 13 iterations. In Figure 3.4 we see the force-displacement response for the true solution, the ini-

tial guess, and the reconstructed parameter set. The reconstructed parameter set is

$$\begin{Bmatrix} R \\ S \\ \chi \\ \phi^{Max} \end{Bmatrix} = \begin{Bmatrix} 1.66 \times 10^{9} \\ 4.62 \times 10^{9} \\ -0.894 \\ 3.20 \times 10^{-4} \end{Bmatrix}. \tag{3.181}$$

While the reconstructed parameter set, (3.181), may seem vastly different from

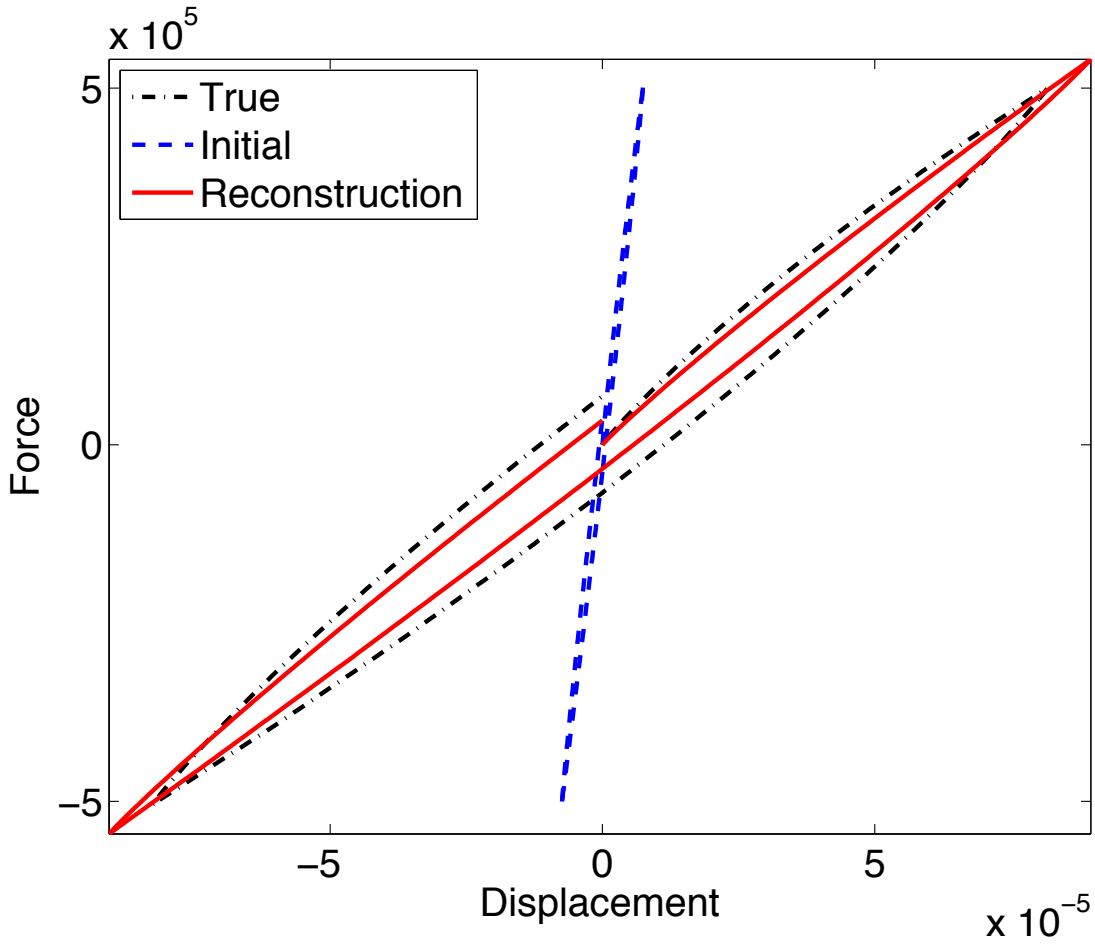

Figure 3.4: Single element force-displacement response reconstruction. Displacement is in meters; force is in newtons.

the true parameter set, (3.177), Figure 3.4 indicates that the force-displacement

response may not be uniquely determined by a parameter set. However, since we are interested in parameters that match the measured response, a more suitable measure of the true response of the system is the force-displacement response.

In order to study different initial conditions, we perform the same experiment for a different set of initial conditions. Specifically, we set the initial conditions to,

$$\begin{Bmatrix} R \\ S \\ \chi \\ \phi^{Max} \end{Bmatrix} = \begin{Bmatrix} 1 \times 10^9 \\ 2 \times 10^9 \\ -0.8 \\ 4 \times 10^{-4} \end{Bmatrix}. \tag{3.182}$$

Because the tangent stiffness is softer for the initial guess, we correspondingly increase β_p to 0.2. We also set the maximum number of SOR iterations to 20. Again, we stop the global algorithm when E_{ECE} stagnates. This is achieved with a tolerance of 5×10^{-5}. The reconstructed parameters are,

$$\begin{Bmatrix} R \\ S \\ \chi \\ \phi^{Max} \end{Bmatrix} = \begin{Bmatrix} 2.85 \times 10^9 \\ 4.86 \times 10^9 \\ -0.798 \\ 1.91 \times 10^{-4} \end{Bmatrix}. \tag{3.183}$$

We see the corresponding force-displacement response in Figure 3.5. In each reconstruction we observe that we do not recover the true parameter set. We do, however, recover a parameter set that better approximates the force-displacement response than the initial conditions. In each case we observe that the algorithm stagnates in a local minimum. In this local minimum we find that we better capture the maximal force-displacement as opposed to the width of the force-dissipation curve. The width of the curve corresponds to dissipation. $\mathcal{U}$ is postulated in terms of internal force discrepancy, and hence we expect to reconstruct the maximal force with higher accuracy than dissipation.

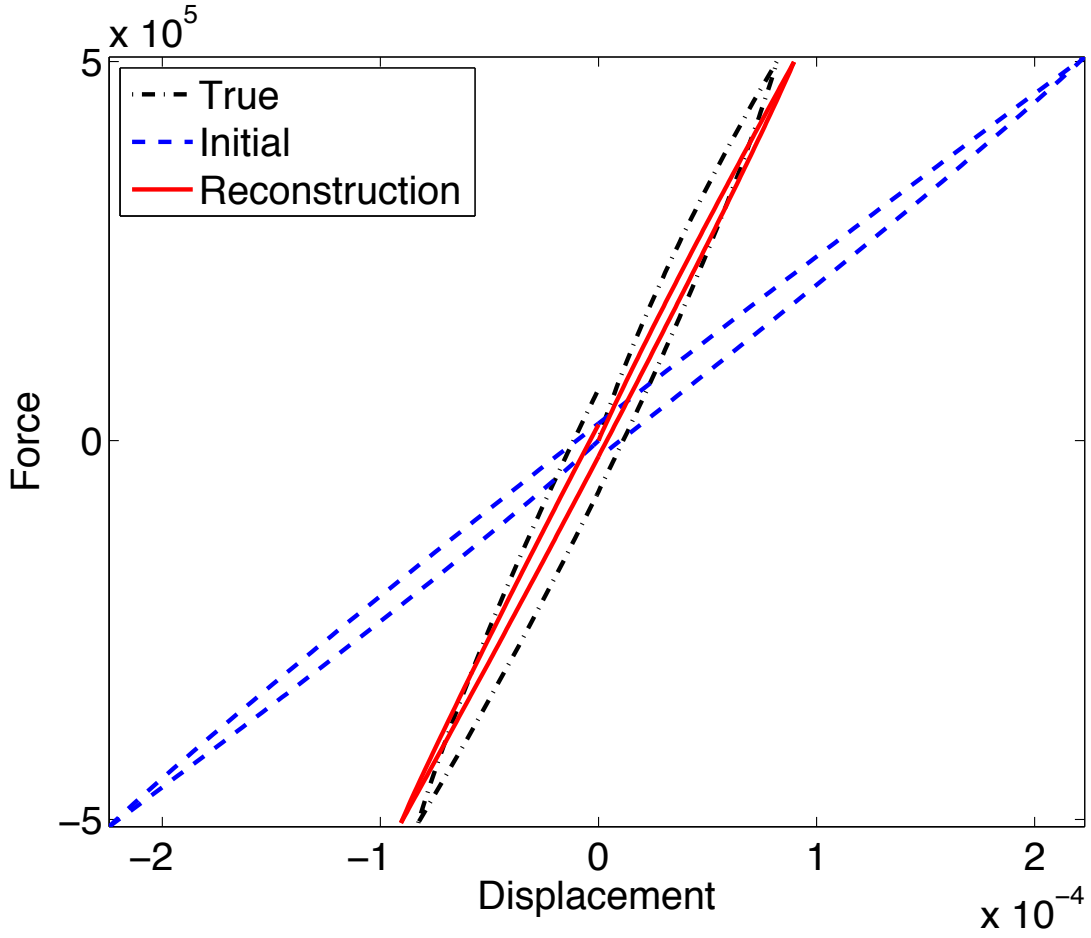

Figure 3.5: Single element force-displacement response reconstruction. Displacement is in meters; force is in newtons.

Performing these examples several times, with different samples of 5% Gaussian noise, we found that both initial conditions converge in 10-15 iterations. This indicated that the algorithm was robust to different samples of noise. User intervention is only necessary to identify the stagnation point. However, this can be achieved automatically by observing the relative difference between successive errors.

We performed an example using the initial conditions (3.182) where we set the maximum number of iterations at 15, and observed how many SOR iterations were required for the coupled solve at each iteration. We set $\beta_p = .2$ and $\omega = .1$. We

stop the algorithm for this test when E_{ECE} reaches 1×10^{-4}. We see the number of SOR iterations plotted for the coupled solve in each iteration plotted in Figure 3.6. We see rapid convergence in later iterations for two reasons. First, we reinitialize

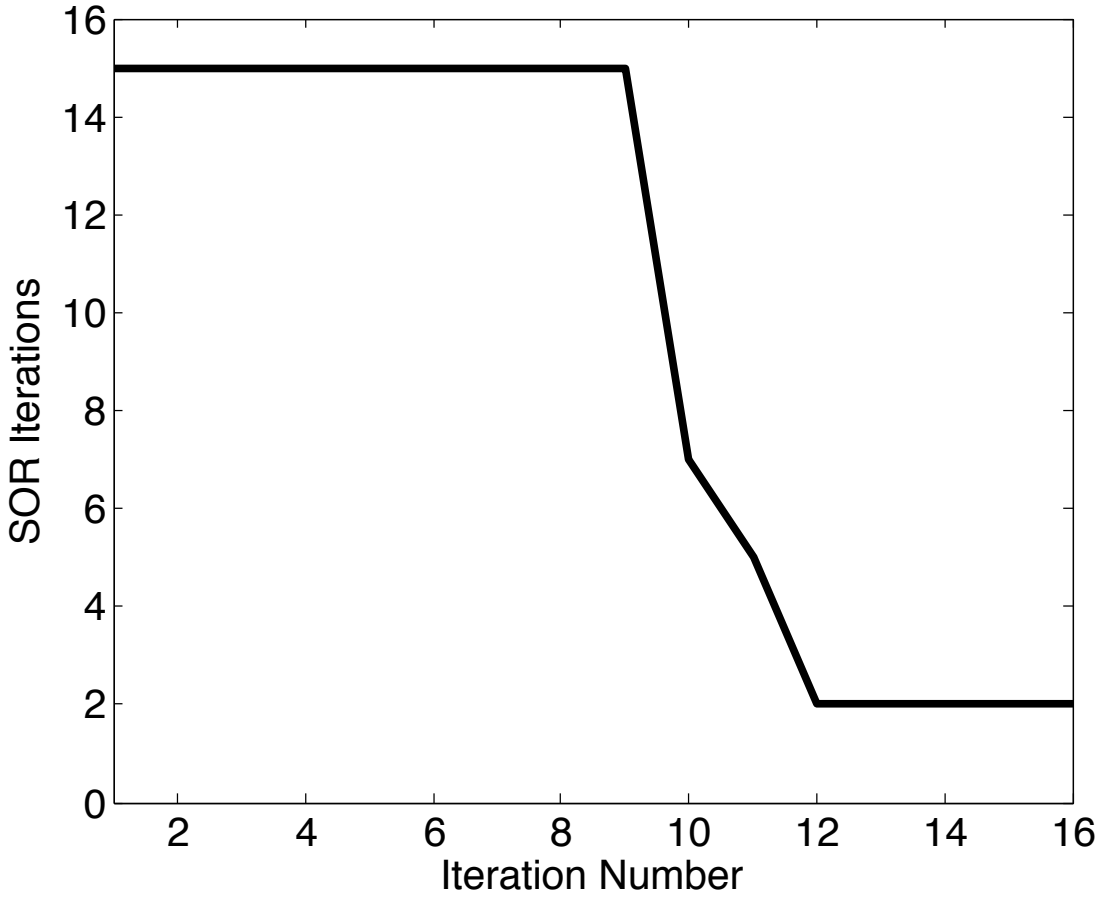

Figure 3.6: Number of SOR-Newton iterations required to solve the coupled problem at each iteration

the SOR iterations with the previous solution at the next iteration. Second, as we converge on the right parameter set, the magnitude of $\{u\} - \{u^M\}$ decreases, and therefore the magnitude of $\{\bar{u}\}$ decreases. We find that the later iterations not only converge to the tolerance, but converge in very few iterations.

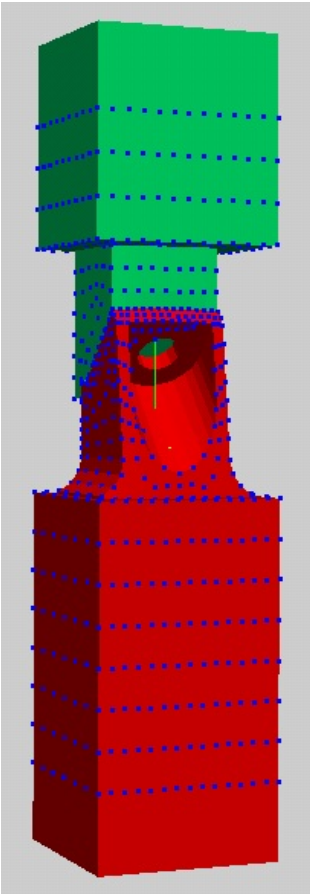

Figure 3.7: Lap joint with Iwan interface. Measurement points are highlighted.

3.4.2 Lap Joint with Iwan Interface

We now progress to a larger reconstruction problem, with sparse, indirect, noisy measurements. For this example, all computations are done with 8 processors. We used the same finite element model of a lap joint as used in [81]. We have visualized the joint along with the measurement points in Figure 3.7. There are 833 nodes on the surface where we measure displacement in all three directions. The three dimensional elements of the joint are presumed known. They are linear

isotropic elastic materials, with parameters,

$$\begin{Bmatrix} \rho \\ E \\ \nu \end{Bmatrix} = \begin{Bmatrix} 8300\ kg/m^3 \\ 210\ GPa \\ 0.3 \end{Bmatrix} \tag{3.184}$$

where ρ is density, E is Young's modulus, and ν is Poisson's ratio. Physically, these parameters are similar to those of steel steel. We also include mass proportional damping in these blocks. We use a proportionality constant of 1×10^{-4}. This was chosen so the response exhibits enough dissipation to tax the numerics, yet still exhibit a physically meaningful response. Specifically we can express the damping matrix that appears in (3.19) as

$$[C] = (1 \times 10^{-4})[M] \tag{3.185}$$

The interface, *i.e.* the surface where the top and bottom blocks meet in Figure 3.7, is treated with a multipoint constraint. Specifically the nodes on each surface are condensed to a single virtual node bound to the corresponding node on the other surface. The two nodes are connected with an independent Iwan model in each of the tangential (sheer) directions. The first direction lies on the interface plane and intersects the plane of symmetry through the entire structure. The second direction is tangent to the interface plane and is perpendicular to the first Iwan direction. The Iwan elements are discretized in the same way as in the single element model, using $N = 51$ individual Jenkins elements and $\alpha = 1.2$ is the geometric progression constant for the spacing. Moreover, the rotation about the normal axis is modeled with an elastic torsion spring. Our reconstruction will seek to identify each Iwan model and rotational spring constant. We apply a traction to the bottom surface with equal magnitudes in the x, y, and z directions. The magnitude of the force components is shown in Figure 3.8. We apply a homogeneous Dirichlet condition on the top surface. We generate the true solution using the following set of parameters

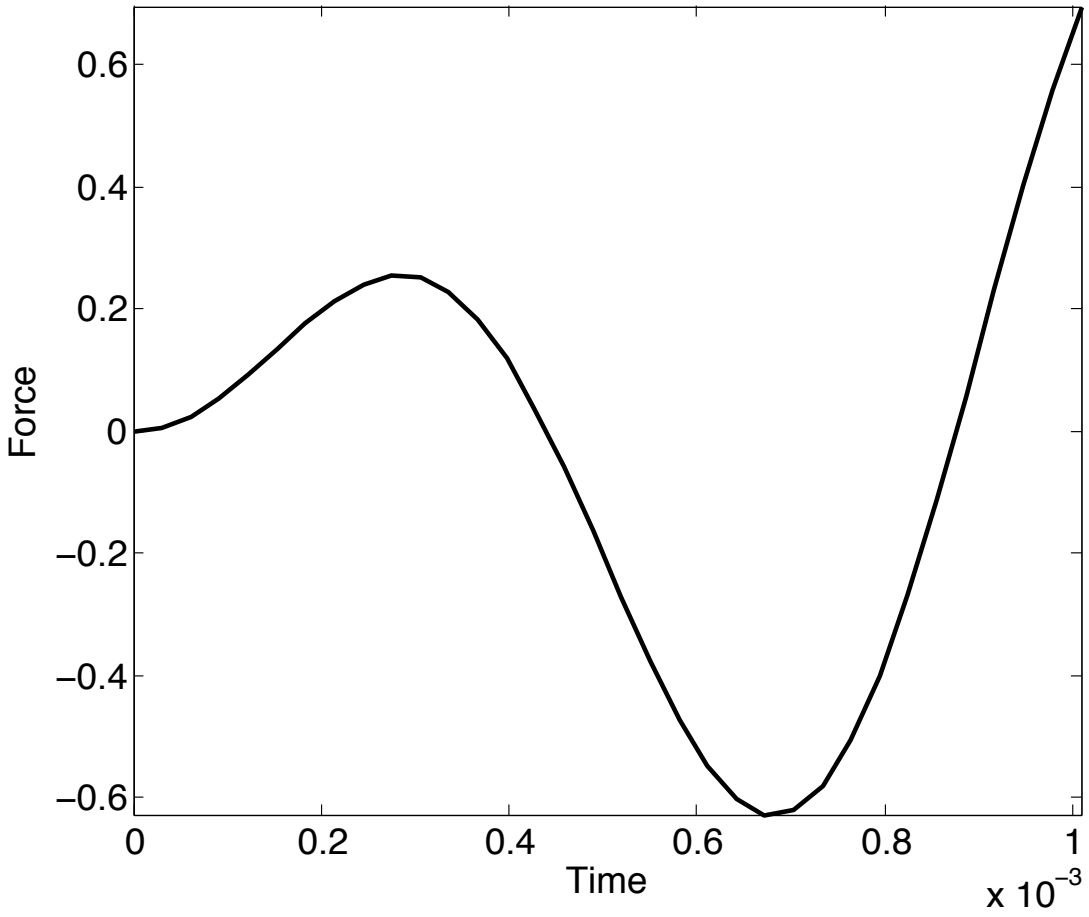

Figure 3.8: The magnitude (in Newtons) of each component of the traction applied to the lap joint model is plotted on the y axis. Time (in seconds) is plotted on the x axis.

for both Iwan models,

$$\begin{Bmatrix} R \\ S \\ \chi \\ \phi^{Max} \end{Bmatrix} = \begin{Bmatrix} 5.51 \times 10^5 \\ 2.11 \times 10^5 \\ -0.800 \\ 2.75 \times 10^{-5} \end{Bmatrix}. \tag{3.186}$$

We set the rotational spring constant equal to,

$$K_r = 1 \times 10^9 \ GPa. \tag{3.187}$$

and use a time step of $\Delta t = 1 \times 10^{-3}$ for 100 time steps. We subsequently pollute the measurements with 5% Gaussian noise using the same model, (3.178), as in the single element examples. Similar to the previous example, we optimize over the physical parameter set in the material updating part of the MECE algorithm using the trust region L-BFGS optimization package with parameter bounds

$$\begin{Bmatrix} 5 \times 10^4 \\ 0.1 \\ -0.9 \\ 1 \times 10^{-3} \end{Bmatrix} \leq \begin{Bmatrix} K_T \\ F_S \\ \chi \\ \beta_I \end{Bmatrix} \leq \begin{Bmatrix} 5 \times 10^9 \\ 1 \times 10^6 \\ -0.1 \\ 5 \times 10^3 \end{Bmatrix}. \tag{3.188}$$

We experiment with two different initial conditions, as in the single element examples. While both initial conditions are softer than the true solution, the second is much softer, as evident in the force-displacement plots we will show. We use these two examples to explore robustness to accurate initial conditions. The second example is much less accurate than the firs. While we ultimately identify a local minimum in each case, we reconstruct reasonable solutions that show marked improvement over the initial guess.

$$\begin{Bmatrix} R \\ S \\ \chi \\ \phi^{Max} \end{Bmatrix} = \begin{Bmatrix} 5.51 \times 10^6 \\ 2.11 \times 10^6 \\ -0.820 \\ 1.75 \times 10^{-6} \end{Bmatrix}. \tag{3.189}$$

We set the initial guess for the rotational spring constant as

$$K_r = 5 \times 10^9 GPa. \tag{3.190}$$

We set $\beta_p = 1 \times 10^{-4}$ and $\omega = 0.1$. We set the SOR tolerance at 1×10^{-5} and a maximum number of SOR iterations of 10. We solve to a global tolerance of

1×10^{-4}. The reconstructed parameters are,

$$\begin{Bmatrix} R \\ S \\ \chi \\ \phi^{Max} \end{Bmatrix} = \begin{Bmatrix} 7.54 \times 10^5 \\ 1.72 \times 10^6 \\ -0.800 \\ 2.07 \times 10^{-4} \end{Bmatrix}. \tag{3.191}$$

for the first tangential direction, and

$$\begin{Bmatrix} R \\ S \\ \chi \\ \phi^{Max} \end{Bmatrix} = \begin{Bmatrix} 9.64 \times 10^5 \\ 1.31 \times 10^6 \\ -0.800 \\ 4.28 \times 10^{-5} \end{Bmatrix}. \tag{3.192}$$

for the second tangential direction. The first tangential direction lies on the interface in the plane of symmetry for the total lap joint. The second tangential direction is on the interface surface, but orthogonal to the first direction. The reconstructed rotational spring constant is, $K_r = 1.103 \times 10^9\ GPa$. We can see the corresponding force-displacement response for each direction in Figures 3.9-3.10. While these parameters may appear different from the true set, we see that they generate the same force-displacement response. Similarly, they have decreased the E_{ECE} and E_{LS} error measurements. We observe that the reconstruction in the first direction is better than that of the second, as we have less sensitivity along the second direction. Because there are likely local minima in the objective function surface, we have recovered a parameter set that improves the fit of the force-displacement curve, but the algorithm stagnates in a local minimum. This parameter set has improved the maximum displacement of the Iwan elements, but has not as accurately recovered the dissipation, *i.e.* the width of the force-displacement curve.

We use the same β_p and ω for the soft initial conditions, but we set a global

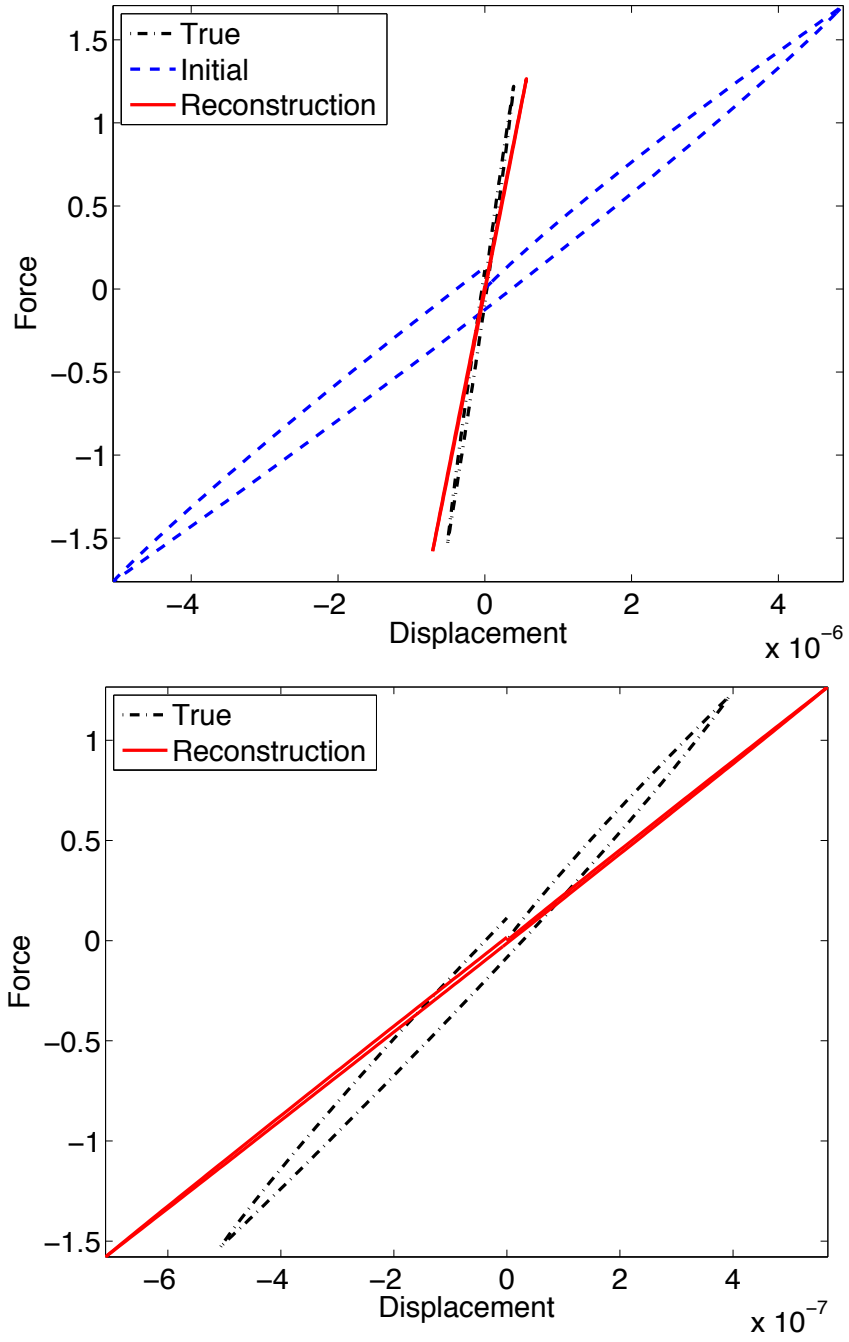

Figure 3.9: Here we see the reconstructed force-displacement response for direction 1 of the interface given a stiff initial condition. We show the plot with and without the initial conditions in order to accurately capture the scale. Displacement is in meters; force is in newtons.

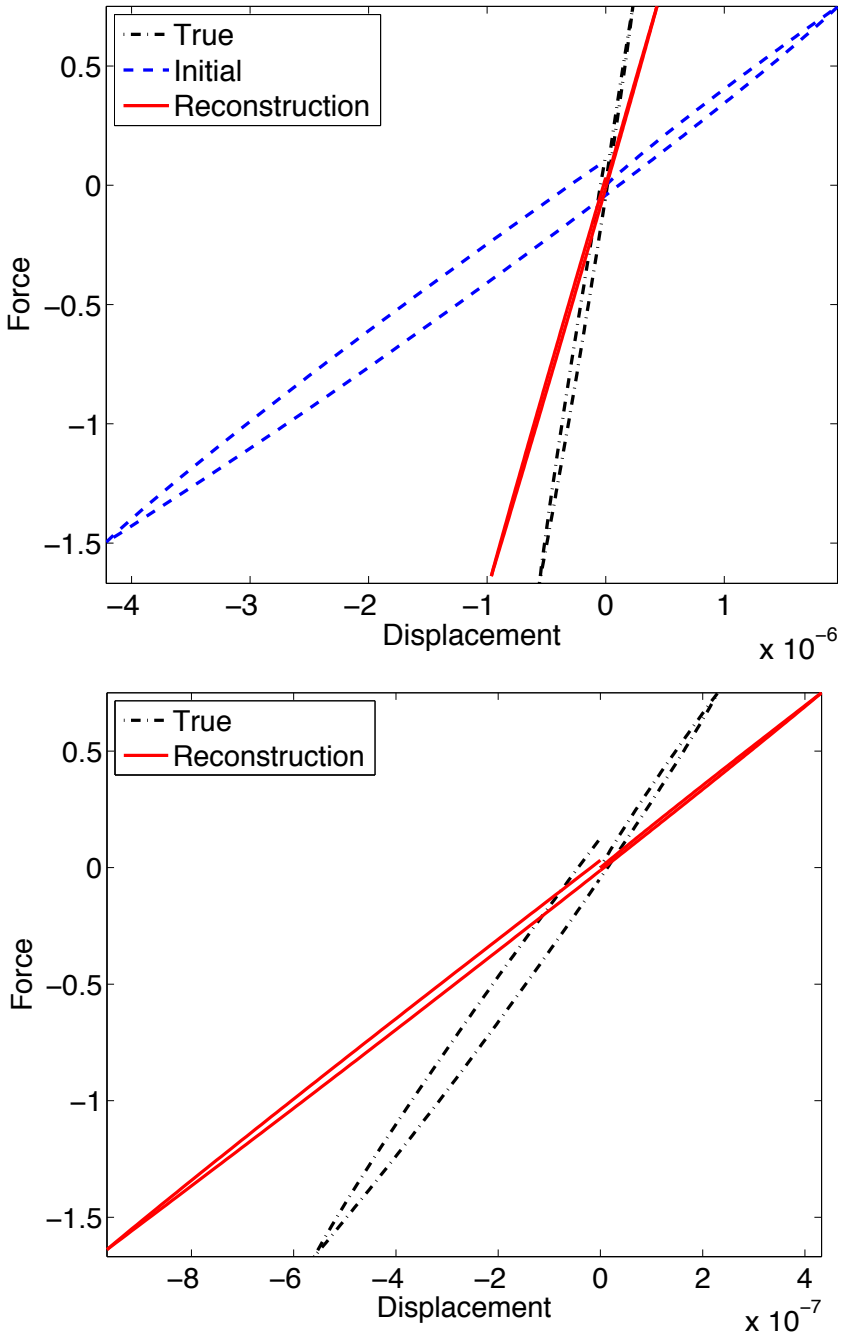

Figure 3.10: Here we see the reconstructed force-displacement response for direction 2 of the interface given a stiff initial condition. We show the plot with and without the initial conditions in order to accurately capture the scale. Displacement is in meters; force is in newtons.

tolerance of 1×10^{-3} to avoid stagnation. We set the SOR tolerance to 1×10^{-4}, as it needs to be tighter than the global tolerance, yet we do not want to waste computational time achieving tolerances that are unnecessarily tight. We maintain the maximum number of SOR iterations of 10. The initial parameter set for both Iwan models in this case is,

$$\begin{Bmatrix} R \\ S \\ \chi \\ \phi^{Max} \end{Bmatrix} = \begin{Bmatrix} 5.51 \times 10^4 \\ 2.11 \times 10^4 \\ -0.800 \\ 1.75 \times 10^{-4} \end{Bmatrix}. \tag{3.193}$$

We initialize the rotational spring as

$$K_r = 1 \times 10^9. \tag{3.194}$$

While some of these parameters are the same as the true parameters, the response that the ensemble produces is very much different than the true response. The reconstructed parameters are,

$$\begin{Bmatrix} R \\ S \\ \chi \\ \phi^{Max} \end{Bmatrix} = \begin{Bmatrix} 6.83 \times 10^5 \\ 1.83 \times 10^6 \\ -0.800 \\ 2.48 \times 10^{-4} \end{Bmatrix}. \tag{3.195}$$

for the first direction, and

$$\begin{Bmatrix} R \\ S \\ \chi \\ \phi^{Max} \end{Bmatrix} = \begin{Bmatrix} 6.87 \times 10^5 \\ 1.12 \times 10^6 \\ -0.800 \\ 1.06 \times 10^{-4} \end{Bmatrix}. \tag{3.196}$$

for the second direction. The reconstructed rotational spring constant is $K_r = 1.01 \times 10^8\ GPa$. We can see the reconstructed force-displacement response in

Figures 3.11-3.12. Again we see better sensitivity in the first direction. This is consistent with the previous example. Moreover, we see again that we have better reconstructed the maximal displacements in the force-displacement curves than the dissipation (width). We have converged on a parameter set that while different from the true set, provides a better reconstruction of the measured response than the initial guess. We can attribute this again to the local minimum we have converged upon. We observe that the reconstructions are more sensitive to maximal displacement and maximal force in the force-displacement curves, than the dissipation. We can attribute this to the objective function; we can see how large discrepancies in the maximal values attained by the internal force vector will correspond to larger errors. Hence these scheme is more sensitive to these mismatches.

We also show the convergence of the ECE error and the Least Squares (LS) measurement error for this final numerical experiment in Figure 3.13. We choose β_p such that each error measure has the same order of magnitude in the initial iteration. By the time we terminate the algorithm, the E_{LS} error has stagnated, but the ECE error is still showing some progression. We stop when the least squares error has stagnated as E_{ECE} is measured only on the unknown elements, while E_{LS} is an indicator of global fit, as discussed in section 3.3.4.

3.5 Conclusions

We have developed and implemented a robust method for nonlinear material characterization. We have derived a general framework within which we can work with various nonlinear, hysteretic, material models. We have implemented the Iwan model specifically, and have shown that we can recover material parameters that will reproduce the force-displacement response in the measured solution. This for-

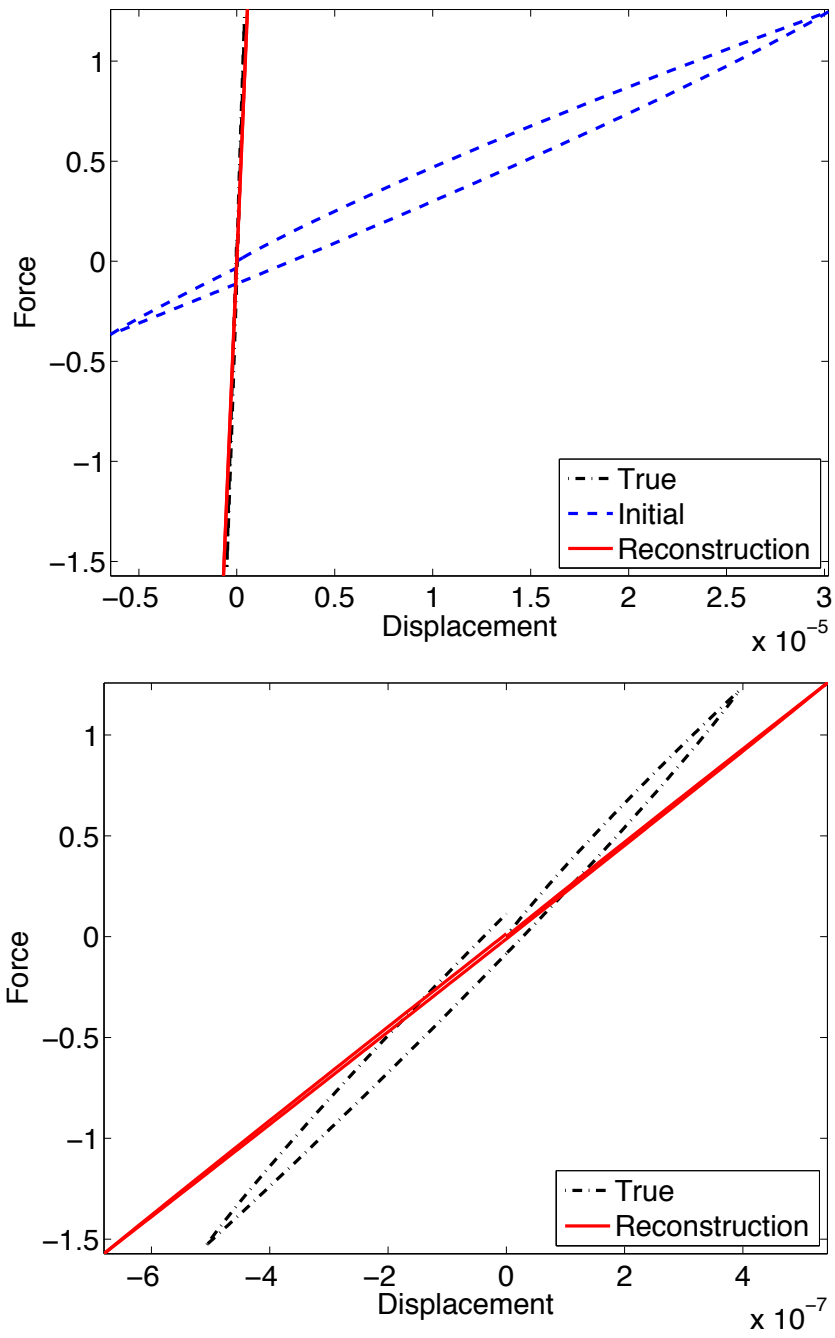

Figure 3.11: Here we see the reconstructed force-displacement response for direction 1 of the interface given a soft initial condition. We show the plot with and without the initial conditions in order to accurately capture the scale. Displacement is in meters; force is in newtons.

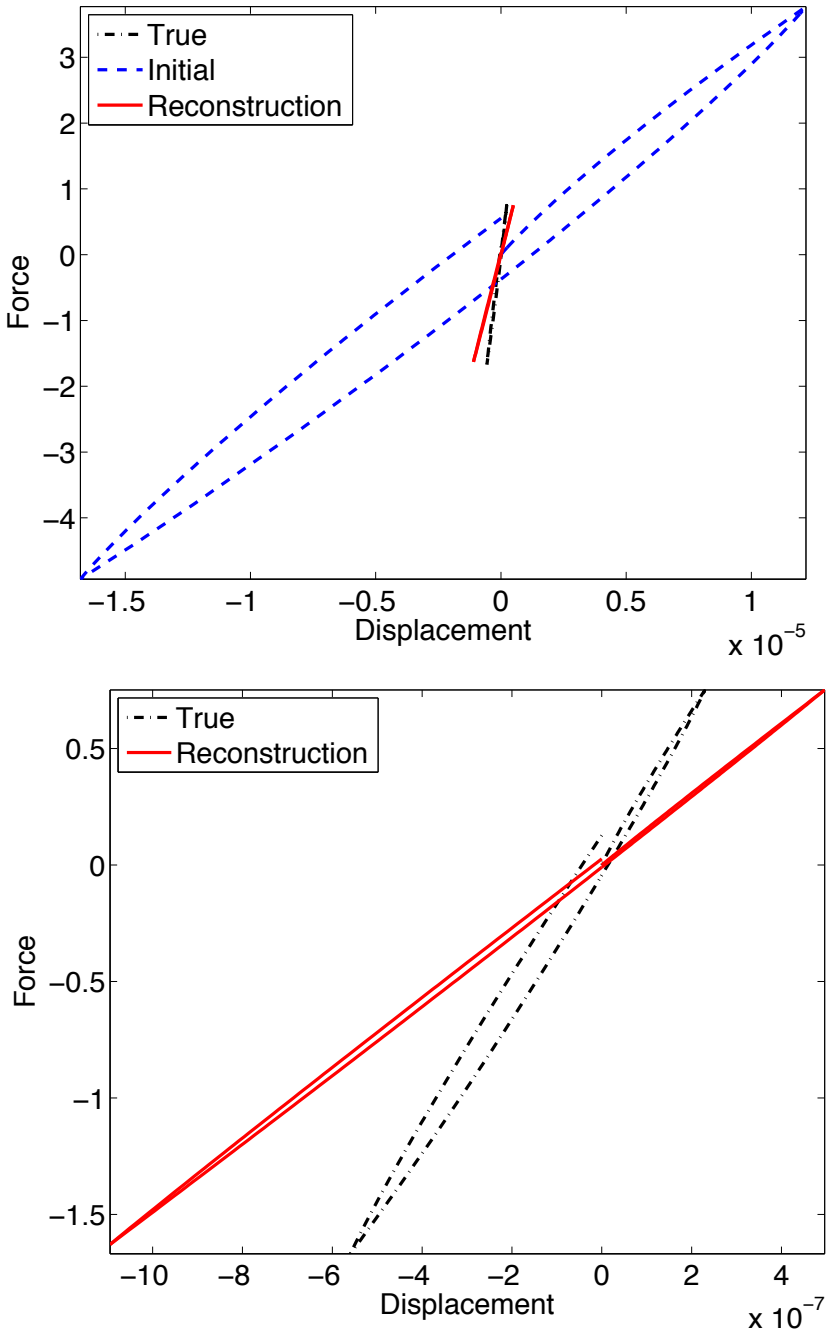

Figure 3.12: Here we see the reconstructed force-displacement response for direction 2 of the interface given a soft initial condition. We show the plot with and without the initial conditions in order to accurately capture the scale. Displacement is in meters; force is in newtons.

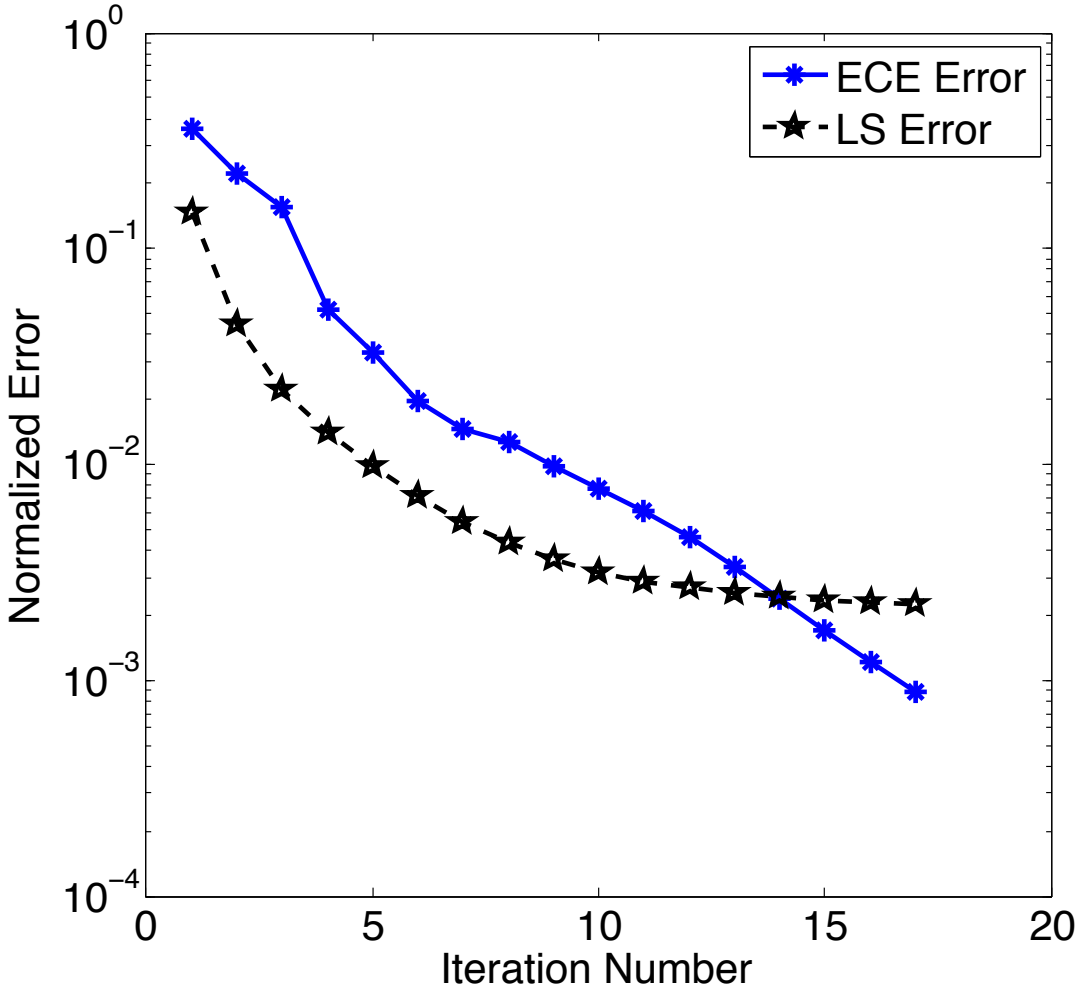

Figure 3.13: Here we see convergence of each error measure for successive iterations.

mulation is robust to noise and initial conditions. Moreover, this method is highly adaptable. We have broken the overall scheme into district subproblems: the coupled forward and adjoint solve, and the parameter update step. Each of these steps can be customized or extended. The coupled solve could be done with a variety of techniques, including Newton-SOR, and nonlinear conjugate gradients. While we have used specific optimization packages to perform the material update, other material models may admit analytic parameter updates. In the instance where

we need to perform the parameter update numerically, other algorithms and optimization packages can be used without interfering with the rest of the scheme. The MECE material identification technique is a robust alternative to classical methods for material identification. Future work analyzing the properties of the objective functional may reveal insights as to stopping criteria and penalty parameter selection/tuning. This implementation provides users the capability to tune finite element models to real, observed measurements.

CHAPTER 4

CONCLUSION

Throughout this work I have focused on the inverse problems, and specifically on computational aspects. All of the algorithms and derivations outlined were subsequently implemented in various codes. However, most of the implementation took place in Sierra/SD, which is highly scalable, and originally conceived for mostly linear finite element analysis. Some of the challenges this posed were maintaining scalability, reusing underlying code, and integrating optimization libraries.

There are natural extensions of the work presented here. Future extensions of the source localization work would naturally include time domain problems. Moreover, we could further study how sensitivity at measurement points affect the algorithms performance. Future extensions of the MECE work could include a more robust coupled forward and adjoint solver. Most of the computational expense is in the coupled solver, and improving upon the SOR scheme outlined could significantly improve the total computational time required by the algorithm. In addition, we could further study the regularizing behavior of the penalty parameter, and better understand how it influences the reconstructed material parameters.

There are two contributions outlined in this thesis. First is the broadly applicable source localization technique, which is relatively easy to implement within an existing finite element code base. Second is the technical details required to implement the MECE technique for nonlinear materials identification in a production level code base, and the actual implementation of this within the Sierra/SD framework. Throughout the implementation, I tried to make components, such as the adjoint solver, reusable so as to allow for easier future implementation of other inverse problem capabilities.

BIBLIOGRAPHY

[1] V. Akçelik, B. Biros, O. Ghattas, K. Long, and B. van Bloemen Waanders. A variational finite element method for source inversion for convective-diffusive transport. *Finite Elements in Analysis and Design*, 2003.

[2] O. E. Andreikiv, V. R. Skal's'kyi, and O. M. Serhienko. Acoustic-emission criteria for rapid analysis of internal defects in composite materials. *Materials Science*, 2001.

[3] J. Antoni. A bayesian approach to sound source reconstruction: Optimal basis, regularization, and focusing. *Journal of the Acoustical Society of America*, 2012.

[4] I. Argatov and E. Butcher. On the iwan models for lap-type bolted joints. *International Journal of Non-Linear Mechanics*, 46(2):347 – 356, 2011.

[5] S. R. Arridge. Optical tomography in medical imaging. *Inverse problems*, 15(2):R41, 1999.

[6] S. Avril, M. Bonnet, A. S. Bretelle, M. Grediac, F. Hild, P. Ienny, F. Latourte, D. Lemosse, S. Pagano, E. Pagnacco, et al. Overview of identification methods of mechanical parameters based on full-field measurements. *Experimental Mechanics*, 48(4):381–402, 2008.

[7] G. Bal, D. Finch, J. Schotland, P. Kuchment, and P. Stefanov. *Tomography and inverse transport theory*, volume 559. Amer Mathematical Society, 2012.

[8] B. Banerjee, T. F. Walsh, W. Aquino, and M. Bonnet. Large scale parameter estimation problems in frequency-domain elastodynamics using an error in constitutive equation functional. *Computer Methods in Applied Mechanics and Engineering*, 2012.

[9] B. Baran and C. Basdogan. Force-based calibration of a particle system for realistic simulation of nonlinear and viscoelastic soft tissue behavior. In Astrid Kappers, Jan van Erp, Wouter Bergmann Tiest, and Frans van der Helm, editors, *Haptics: Generating and Perceiving Tangible Sensations*, volume 6191 of *Lecture Notes in Computer Science*, pages 23–28. Springer Berlin / Heidelberg, 2010.

[10] C. Bellis and M. Bonnet. A fem-based topological sensitivity approach for fast qualitative identification of buried cavities from elastodynamic overde-

termined boundary data. *International Journal of Solids and Structures*, 47(9):1221 – 1242, 2010.

[11] T. Belytschko, W. K. Liu, and B. Moran. *Nonlinear Finite Elements for Continua and Structures*. John Wiley & Sons Ltd., 2006.

[12] J. Benoit, C. Chauviére, and P. Bonnet. Source identification in time domain electromagnetics. *Journal of Computational Physics*, 231(8):3446 – 3456, 2012.

[13] M. Bhardwaj, K. Pierson, G. Reese, T. Walsh, D. Day, K. Alvin, J. Peery, C. Farhat, and M. Lesoinne. Salinas: a scalable software for high-performance structural and solid mechanics simulations. In *Supercomputing, ACM/IEEE 2002 Conference*, pages 35–35. IEEE, 2002.

[14] L. T. Biegler. *Large-scale PDE-constrained optimization*, volume 30. Springer Verlag, 2003.

[15] G. Biros and O. Ghattas. Parallel lagrange–newton–krylov–schur methods for pde-constrained optimization. part ii: The lagrange–newton solver and its application to optimal control of steady viscous flows. *SIAM Journal on Scientific Computing*, 27(2):714–739, 2005.

[16] G. Biros and O. Ghattas. Parallel lagrange newton krylov schur methods for pde-constrained optimization. part ii: The lagrange-newton solver and its application to optimal control of steady viscus flows. *SIAM J. Sci. Comput.*, 2005.

[17] P. Blomgren, G. Papanicolaou, and H. Zhao. Super resolution in time-reversal acoustics. *Journal of the Acoustical Society of America*, 2002.

[18] G. Bolzon, G. Maier, and M. Panico. Material model calibration by indentation, imprint mapping and inverse analysis. *International Journal of Solids and Structures*, 41:2957 – 2975, 2004.

[19] M. Bonnet. Fast identification of cracks using higher-order topological sensitivity for 2-d potential problems. *Engineering Analysis with Boundary Elements*, 2011.

[20] M. Bonnet and A. Constantinescu. Inverse problems in elasticity. *Inverse problems*, 21(2):R1, 2005.

[21] M. Bonnet and B. Guzina. Sounding of finite bodies by way of topological derivative. *Int. J. Numer. Meth. Engng.*, 2004.

[22] M. Bonnet and B. B. Guzina. Elastic-wave identification of penetrable obstacles using shape-material sensitivity framework. *J. Comput. Phys.*, 228(2):294–311, February 2009.

[23] I. Bouchouev and V. Isakov. Uniqueness, stability and numerical methods for the inverse problem that arises in financial markets. *Inverse problems*, 15(3):95–116, 1999.

[24] A. F. Bower. *Applied Mechanics of Solids*. CRC Press, 2010.

[25] S. Boyd and L. Vandenberghe. *Convex optimization*. Cambridge university press, 2004.

[26] R. Byrd, P. Lu, J. Nocedal, and C. Zhu. A limited memory algorithm for bound constrained optimization. *SIAM Journal on Scientific Computing*, 1995.

[27] A. Carpinteri, G. Lacidogna, and N. Pugno. Structural damage diagnosis and life-time assessment by acoustic emission monitoring. *Engineering Fracture Mechanics*, 2007.

[28] G. Cervone, P. Franzese, and A. Grajdeanu. Characterization of atmospheric contaminant sources using adaptive evolutionary algorithms. *Atmospheric Environment*, 2010.

[29] H. Chalal, F. Meraghni, F. Pierron, and M. Grédiac. Direct identification of the damage behaviour of composite materials using the virtual fields method. *Composites Part A: Applied Science and Manufacturing*, 35:841 – 848, 2004.

[30] T. F. Chan, G.H. Golub, and P. Mulet. A nonlinear primal-dual method for total variation-based image restoration. *SIAM Journal on Scientific Computing*, 20(6):1964–1977, 1999.

[31] A. J. Devaney. Time reversal imaging of obscured targets from multistatic data. *IEEE Transactions on Antennas and Propagation*, 2005.

[32] S. W. Doebling, C. R. Farrar, and M. B. Prime. A summary review of vibration-based damage identification methods. *Shock and Vibration Digest*, 30(2):91–105, 1998.

[33] C. R. Dohrmann, A. Klawonn, and O. B. Widlund. A family of energy minimizing coarse spaces for overlapping schwarz preconditioners. *Domain decomposition methods in science and engineering XVII*, pages 247–254, 2008.

[34] M. M. Doyley. Model-based elastography: a survey of approaches to the inverse elasticity problem. *Physics in Medicine and Biology*, 57(3):R35, 2012.

[35] L. C. Evans. *Partial Differential Equations*. Graduate Studies in Mathematics. American Mathematical Society, 1998.

[36] G. Feijoo. A new method in inverse scattering based on the topological derivative. *Inverse Problems*, 2004.

[37] P. Feissel and O. Allix. Modified constitutive relation error identification strategy for transient dynamics with corrupted data: The elastic case. *Computer methods in applied mechanics and engineering*, 196(13):1968–1983, 2007.

[38] M. Fink, D. Cassereau, A. Derode, C. Prada, P. Roux, M. Tanter, J. L. Thomas, and F. Wu. Time-reversed acoustics. *Rep. Prog. Phys.*, 2000.

[39] G. Geymonat and S. Pagano. Identification of mechanical properties by displacement field measurement: a variational approach. *Meccanica*, 38(5):535–545, 2003.

[40] M. S. Gockenbach and A. A. Khan. An abstract framework for elliptic inverse problems: Part 1. an output least-squares approach. *Mathematics and mechanics of solids*, 12(3):259–276, 2007.

[41] G. Gurney, R. Law, A. Denning, P. Rayner, D. Baker, P. Bousquet, L. Bruhwiler, Y. H. Chen, P. Ciais, S. Fan, I. Fung, M. Gloor, M. Heimann, K. Higuchi, J. John, T. Maki, S. Maksyutov, K. Masaire, P. Peylin, M. Prather, B. Pak, J. Randerson, J. Sarmiento, S. Taguchi, T. Takahashi, and C. W. Yuen. Towards robust regional estimates of CO_2 sources and sinks using atmospheric transport models. *Nature*, 2002.

[42] L. A. Hageman and T. A. Porsching. Aspects of nonlinear block successive overrelaxation. *SIAM Journal on Numerical Analysis*, 12(3):316–335, 1975.

[43] A. Hayes and A. Martinoli. Distributed odor source localization. *IEEE Sensors Journal*, 2002.

[44] A. Hayes, A. Martinoli, and R. Goodman. Swarm robotic odor localization: Off-line oprimization and validation with real robots. *Robotica*, 2003.

[45] M. Heroux, R. Bartlett, V. Howle, R. Hoekstra, Hu J., T. Kolda, R. Lehoucq, K. Long, R. Pawlowski, E. Phipps, A. Salinger, H. Thornquist, R. Tuminaro, J. Willenbring, A. Williams, and K. Stanley. An overview of the trilinos project. *ACM Trans. Math. Softw.*, 31(3):397–423, 2005.

[46] Y. Z. Ider and S. Onart. Algebraic reconstruction for 3d magnetic resonance–electrical impedance tomography (mreit) using one component of magnetic flux density. *Physiological measurement*, 25(1):281, 2004.

[47] V. Isakov. *Inverse problems for partial differential equations*, volume 127. Springer Verlag, 1998.

[48] D. Jackson and D. Dowling. Phase conjugation in underwater acoustics. *J. Acoust. Soc. Am.*, 2007.

[49] W. Jatmiko. A pso-based mobile robot for odor source localization in dynamic advection-diffusion with obstacles environment: Theory, simulation, and measurement. *Computational Intelligence Magazine, IEEE*, 2007.

[50] H. Johansson and K. Runesson. Calibration of a class of non-linear viscoelasticity models with sensitivity assessment based on duality. *International journal for numerical methods in engineering*, 69(12):2513–2537, 2007.

[51] Y. M. Kadah and X. Hu. Algebraic reconstruction for magnetic resonance imaging under b/sub 0/inhomogeneity. *Medical Imaging, IEEE Transactions on*, 17(3):362–370, 1998.

[52] J. Kaipio and E. Somersalo. *Statistical and computational inverse problems*, volume 160. Springer, 2004.

[53] J. Kaipio and E. Somersalo. Statistical inverse problems: discretization, model reduction and inverse crimes. *Journal of Computational and Applied Mathematics*, 198(2):493–504, 2007.

[54] H. Kawakatsu and J. Montagner. Time reversal seismic source imaging and moment tensor inversion. *Geophys. J. Int.*, 2008.

[55] A. Kirsch. *An introduction to the mathematical theory of inverse problems*, volume 120. Springer, 2011.

[56] I. Knowles. Parameter identification for elliptic problems. *Journal of computational and applied mathematics*, 131(1):175–194, 2001.

[57] R. V. Kohn and A. McKenney. Numerical implementation of a variational method for electrical impedance tomography. *Inverse Problems*, 6(3):389, 1999.

[58] G. Kowadlo and R. Russel. Using naive physics for odor localization in a cluttered indoor environment. *Auton Robot*, 2006.

[59] P. Ladevèze and A. Chouaki. Application of a posteriori error estimation for structural model updating. *Inverse Problems*, 15(1):49, 1999.

[60] P. Ladeveze and D. Leguillon. Error estimate procedure in the finite element method and applications. *SIAM Journal on Numerical Analysis*, 20(3):485–509, 1983.

[61] C. Larmat, J. Tromp, Q. Liu, and J. P. Montagner. Time reversal location of glacial earthquakes. *Journal of Geophysical Research*, 2002.

[62] F. Latourte, A. Chrysochoos, S. Pagano, and B. Wattrisse. Elastoplastic behavior identification for heterogeneous loadings and materials. *Experimental Mechanics*, 48(4):435–449, 2008.

[63] B. Lecampion, A. Constantinescu, and D. Nguyen Minh. Parameter identification for lined tunnels in a viscoplastic medium. *International journal for numerical and analytical methods in geomechanics*, 26(12):1191–1211, 2002.

[64] R. Mahnken and E. Stein. Parameter identification for viscoplastic models based on analytical derivatives of a least-squares functional and stability investigations. *International Journal of Plasticity*, 12(4):451–479, 1996.

[65] E. Marengo, F. Gruber, and F. Simonetti. Time-reversal MUSIC imaging of extended targets. *Image Processing, IEEE Transactions on*, 2007.

[66] Y. K. Mariappan, K. J. Glaser, and R. L. Ehman. Magnetic resonance elastography: a review. *Clinical Anatomy*, 23(5):497–511, 2010.

[67] Y. M. Marzouk and H. N. Najm. Dimensionality reduction and polynomial chaos acceleration of bayesian inference in inverse problems. *Journal of Computational Physics*, 228(6):1862–1902, 2009.

[68] M. Meo, U. Polimeno, and G. Zumpano. Detecting damage in composite material using nonlinear elastic wave spectroscopy methods. *Applied Composite Materials*, 15:115–126, 2008. 10.1007/s10443-008-9061-7.

[69] H. M. Nguyen, O. Allix, and P. Feissel. A robust identification strategy for rate-dependent models in dynamics. *Inverse Problems*, 24(6):065006, 2008.

[70] J. Nocedal and S. Wright. *Numerical Optimization*. Springer, 2006.

[71] A. Oberai, N. Gokhale, and M. Doyley. Evaluation of the adjoint equation based algorithm for elasticity imaging. *Physics in Medicine and Biology*, 2004.

[72] T. Oden and L. Demkowicz. *Applied Functional Analysis*. CRC Press, 2010.

[73] D. S. Oliver and Y. Chen. Recent progress on reservoir history matching: a review. *Computational Geosciences*, 15(1):185–221, 2011.

[74] S. Pang and J. Farrell. Chemical plume source localization. *IEEE Transactions on Systems, Man, and Cybernetics, Part B: Cybernetics*, 2006.

[75] H. W. Park, S. Shin, and H. S. Lee. Determination of an optimal regularization factor in system identification with tikhonov regularization for linear elastic continua. *International Journal for Numerical Methods in Engineering*, 51(10):1211–1230, 2001.

[76] R. E. Plessix. A review of the adjoint-state method for computing the gradient of a functional with geophysical applications. *Geophysical Journal International*, 167(2):495–503, 2006.

[77] E. E. Prudencio, R. Byrd, and X. C. Cai. Parallel full space sqp lagrange–newton–krylov–schwarz algorithms for pde-constrained optimization problems. *SIAM Journal on Scientific Computing*, 27(4):1305–1328, 2006.

[78] K. Ren. Recent developments in numerical techniques for transport-based medical imaging methods. *Commun. Comput. Phys*, 8(1):1–50, 2010.

[79] M. Sambridge and K. Mosegaard. Monte carlo methods in geophysical inverse problems. *Reviews of Geophysics*, 40(3):1009, 2002.

[80] A. Schiela and M. Weiser. Superlinear convergence of the control reduced interior point method for pde constrained optimization. *Computational Optimization and Applications*, 39(3):369–393, 2008.

[81] D. Segalman. A four-parameter iwan model for lap-type joints. *Transactions of the ASME*, 2005.

[82] D. Segalman and M. Starr. Inversion of masing models via continuous iwan systems. *International Journal of Non-Linear Mechanics*, 43(1):74 – 80, 2008.

[83] T. I. Seidman and C. R. Vogel. Well posedness and convergence of some regularisation methods for non-linear ill posed problems. *Inverse problems*, 5(2):227, 1999.

[84] H. S. Shin and G. N. Pande. On self-learning finite element codes based on monitored response of structures. *Computers and Geotechnics*, 27(3):161–178, 2000.

[85] J. Sokolowski and A. Zochowski. On the topological derivative in shape optimization. *SIAM J. Control Optim.*, 1999.

[86] L. Tenorio. Statistical regularization of inverse problems. *SIAM review*, 43(2):347–366, 2001.

[87] R. Unnthorsson, T. Runarsson, and M. Jonsson. Acoustic emission based fatigue failure criterion for cfrp. *International Journal of Fatigue*, 2008.

[88] S. Vakili and M. S. Gadala. Effectiveness and efficiency of particle swarm optimization technique in inverse heat conduction analysis. *Numerical Heat Transfer, Part B: Fundamentals*, 56(2):119–141, 2009.

[89] M. W. Urban, A. Alizad, W. Aquino, J. F. Greenleaf, and M. Fatemi. A review of vibro-acoustography and its applications in medicine. *Current Medical Imaging Reviews*, 7(4):350–359, 2011.

[90] J. Wang and N. Zabaras. A bayesian inference approach to the inverse heat conduction problem. *International Journal of Heat and Mass Transfer*, 47(17):3927–3941, 2004.

[91] R. E. White. Parallel algorithms for nonlinear problems. *SIAM Journal on Algebraic Discrete Methods*, 7(1):137–149, 1986.

[92] C. Zhu, R. H. Byrd, P. Lu, and J. Nocedal. Algorithm 778: L-bfgs-b: Fortran subroutines for large-scale bound-constrained optimization. *ACM Transactions on Mathematical Software (TOMS)*, 23(4):550–560, 1997.

[93] V. A. Zverev. The principle of acoustic time reversal and holography. *Acoustical Physics*, 2003.